



AALBORG UNIVERSITET
STUDENTERRAPPORT

Thermo-Economic Analysis of a Solar Pit Seasonal Heat Storage for Greenhouse Heating

Tarouca Fael João Pedro
Energy Technology, PECT10-2, 2020-05

Master Thesis

ACKNOWLEDGMENTS

I would like to thank my dearest family that helped and supported me in this adventure and even at distance, kept on giving me all the strengths to fulfil my desires. This thesis is dedicated to them, my mother, father, brother and sister.

I would also like show my most appreciation and thanks to my dear professor and supervisor, Ahmad Arabkoohsar, for the support, help and encouragement during my studies in Aalborg University and during this thesis.

Lastly, to all my friend that made this voyage much more appreciated and for their companionship.

Title: Thermo-Economic Analysis of a Solar Pit Seasonal Heat Storage for Greenhouse Heating

Author: Tarouca Fael João Pedro

ABSTRACT

Greenhouse farming is rising due to the high demand of fresh diverse produce and given the fossil-fuel paradigm, it is urging the implementation of renewable and sustainable technologies in this industry.

This thesis is based on the heat demand of a tomato greenhouse implemented on the region of Aarhus, Denmark, with internal temperature variations from 18 to 22 °C, using as main energy source a 2000 m³ pit seasonal thermal energy storage unit, aided by a 3000 m² U-pipe shaped evacuated tube collector field as energy source, having water as medium and with maximum operating temperature of 85 °C.

In order to understand the feasibility of using a pit storage unit to cope the greenhouse's temperature requirements, a thermo-economic analysis was done, conducting an energetic examination based on the heat balance of all units and economically, by a net present value (NPV) approach. Knowing the greenhouse hourly heat demand pattern on a year-basis, a multi-node approach was taken to predict stratification in the, dependent on in-and-out fluxes from the collector field and greenhouse.

The modelling showed that it is possible to cover a 73 % of a 2000 m² tomato growth greenhouse's heat demand for an optimal temperature control, with a solar collector field and pit storage efficiencies of 33.5 % and 80.5 %, respectively. The setup showed a positive NPV of 200,000 € on a 20 years lifetime basis and a payback period of 10 years.

Keywords: Pit seasonal heat storage, U-pipe evacuated tube collectors, solar, greenhouse, stratification, multi-node, thermos-economic.

NOMENCLATURE

Symbol	Unit	Description	Greek Letters	Unit	Description	Subscript	Description
T	K	Temperature	α	–	Absorptivity	<i>amb</i>	Ambient
\dot{m}	kg/s	Mass flow rate	τ	–	Transmissivity	<i>c</i>	Collector
v	m/s	Velocity					
F'	–	ETC efficiency factor	β	$^\circ$	Tilt angle	<i>f</i>	Fluid
cp	J/kgK	Specific Heat	γ	$^\circ$	Declination Angle	<i>i</i>	Inlet
D	m	Diameter	ε	–	Emissivity	<i>o</i>	Outlet
r	m	radius	σ	W/m^2K^4	Stefan-Boltzmann Constant	<i>g</i>	Glass
U	W/m^2K	Global heat transfer coefficient	ρ	kg/m^3	Volumetric mass	<i>p</i>	Plate
h	W/m^2K	Convection heat transfer coefficient	η	%	Efficiency	<i>u</i>	Useful
k	W/mK	Conduction heat transfer coefficient	μ	$Pa \cdot s$	Dynamic viscosity	<i>t</i>	tube
\dot{Q}	Wh	Heat power	ν	m^2/s	Kinematic viscosity	<i>cst</i>	constant
I	W/m^2	Solar Radiation	δ	m	Thickness	<i>med</i>	medium
L	m	Length				<i>GH</i>	Greenhouse
A	m^2	Area				<i>STES</i>	Seasonal thermal energy storage
V	m^3	Volume					
Re	–	Reynolds number				<i>ETC</i>	Evacuated solar collector
Pr	–	Prandtl number					
Nu	–	Nusselt number					
Gr	–	Grashof number					
Ra	–	Raleigh					
g	m/s^2	Acceleration of gravity					

CONTENT

1	OVERVIEW	12
1.1	Solar Irradiation.....	12
1.2	Greenhouse	14
1.3	Seasonal Heat Storage	17
1.4	Solar Collectors	22
2	ENERGY ANALYSIS	26
2.1.	GreenHouse Energy Modelling	33
2.1.1	Greenhouse Energy Balance	34
2.1.2	Solar Irradiation	35
2.1.3	Greenhouse Losses.....	40
2.1.4	Greenhouse Ventilation	46
2.1.5	Internal Energy	47
2.2	U-pipe Evacuated Solar Collector Modelling	48
2.2.1	UpETC Energy Balance	50
2.2.2	Effective Irradiation.....	52
2.2.3	Heat Losses	53
2.2.4	Useful Energy	56
2.2.5	Number of UpETC in series and parallel.....	58
2.2.6	ETC Efficiency	59
2.3	Pit Seasonal Thermal Energy Storage	60
2.3.1	Pit thermal energy storage heat balance	62
2.3.2	Sub-volumes, areas and nodes.....	63
2.3.3	Storage heat losses to surroundings	65
2.3.4	Charge into the pit	69
2.3.5	Discharge of the pit.....	71



2.3.6	Mixing flows	72
2.3.7	Temperature variation on the <i>ith</i> node	74
2.3.8	Pit-storage Efficiency	76
2.4	Validation of energy model.....	77
3	ECONOMIC ANALYSIS	80
4	RESULTS AND DISCUSSION.....	82
4.1	Greenhouse	82
4.2	Solar Collectors	86
4.3	Pit Storage	89
5	CONCLUSIONS	96
6	FUTURE WORKS.....	99
7	REFERENCES.....	100
8	ANNEXES.....	107



INTRODUCTION

The greenhouse effect and creation of microclimate to increase farming efficiency is known for about two millenniums (van Henten, 1994) and its use is increasing continuously, due to the higher demand of fresh produce consumption and lower cost of production (Von Zabeltitz, 2011). Other positive characteristics are the lower water consumption per unit area and higher CO_2 concentrations that increase productivity, making this a high market valuable technology (Czyzyk, Bement, Dawson, & Mehta, 2014).

Choosing the location for a greenhouse implementation is crucial given the different climate conditions that will majorly set the heat demand of the unit (Kittas, Katsoulas, Bartzanas, & Bakker, 2013) and so Mariani, Cola, Bulgari, Ferrante, & Martinetti, 2016 have demonstrated that the heat requirements in Northern European countries are much higher than Mediterranean.

Heating systems for climate control are considered the highest CO_2 producers in greenhouses, where there has been accounted 30 to 90% of the total emissions in greenhouses (Almeida et al., 2014; Baytorun, Önder, & Gügerç, 2016; Boulard et al., 2011; Canakci & Akinci, 2006; Hatirli, Ozkan, & Fert, 2006; Pluimers, Kroeze, Bakker, Challa, & Hordijk, 2000). This and the energy consumption will often dictate the selling cost of produce, is craving the industry to find optimum and greener energy sources, where Sturm, Maier, Royapoor, & Joyce, 2014 have shown that shifting from natural gas heaters to waste combined heat and power (CHP) plants can decrease energy consumption up to 93%.

To contradict the fossil fuel paradigm, several different heating systems have been developed, where Semple, Carriveau, & Ting, 2017 demonstrated that it is profitable to use a seasonal heat storage borehole coupled with a heat pump, or Jain & Tiwari, 2003 which concluded that using heat ground air collectors allowed inside temperatures 6–7°C higher than ambient. Others like Arfaoui, Bouadila, & Guizani, 2017; Benli & Durmuş, 2009; D'Arpa et al., 2016; Mehrpooya, Hemmatabady, & Ahmadi, 2015; Ozgener & Hepbasli, 2005; Xu, Li, Wang, & Liu, 2014; Zhang et al., 2015 have combined heat pumps with solar collector units, latent seasonal heat storage and seasonal soil heat storage units to increase unit's efficiency and decrease running cost of production. All this studies have made greenhouses more efficient and environmentally sustainable (Mariani et al., 2016).

Power sources are not the only way to achieve better cost-benefit, in fact, passive systems are being developed continuously, which generally conduct into lower energy necessities. Çaylı & Akyüz, 2019; Zaimoglu, 2017 shown that using thermal curtains, especially during non-irradiative hours, helps maintaining a more stable interior temperature, where Santamouris, Argiriou, & Vallindras, 1994; Singh & Tiwari, 2010 state that using north walls with lower thermal conductivity than general greenhouse covering materials, like glass or polymers, can help the system by increasing temperature variations from interior and ambient up to 7°C. Dannehl, Schuch, & Schmidt, 2013; Kozai, Shida, & Watanabe, 1986 have shown

that even though thermal curtains may decrease 11% of light transmission, the system can still profit up to 32% in energy yield.

The modelling process of a greenhouse can be of various cases like energetic, exergetic, environmental and economical (Başçetinçelik, Öztürk, Paksoy, & Demirel, 1999; Hepbasli, 2011; Öztürk, 2005; Pasgianos, Ar, & Polycarpou, 2003). For energy analysis, researchers like Benli & Durmuş, 2009; Lafont & Balmat, 2002 have used the fuzzy logic control model, which allowed optimal temperature and relative humidity and good comprise with experimental results. Some other approaches to promote higher control of the microclimate have been studied like linear programming setups or the heating set-point trajectory approach (Chalabi & Zhou, 1996; Jadidi, Sabuni, Homayounifar, & Mohammadi, 2012).

Solar energy is economically viable and environmentally friendly and it has been shown to be a good direct energy source for greenhouses, especially for warmer climates, but given its intermittency, it often requires energy storage units to harvest and store it as form of heat. (Dincer & Ezan, 2018) Using solar energy to produce heat is often integrated with heat storage units, given their low cost-benefit and it has been used widely in greenhouses as main energy power source (Mahmood Farzaneh-Gord, Arabkoohsar, Bayaz, & Khoshnevis, 2013; Mehrpooya et al., 2015; Xu et al., 2014).

There are three main types of solar collectors: Flat plate collectors (FPC), evacuated tube collectors (ETC) and concentrating parabolic collectors (CPC), where it has been shown that using evacuated solar collectors for colder climates provides higher efficiencies with lower heat losses than FPC (Maraj, Londo, Firat, & Gebremedhin, 2019), although it should be taken into account that with high working fluid temperatures ($> 80^{\circ}\text{C}$), vacuum deterioration may happen, thus decreasing highly its performance (Saikia, Nath, & Bhanja, 2019). It has been proved that orientation, disposition and high specific heat of working medium are some of the major specs of solar collectors which will also affect the storage unit's performance, stratification levels and the levelized cost of energy (LCOE) (Z. Tian, Perers, Furbo, & Fan, 2018; Zelzouli, Guizani, Sebai, & Kerkeni, 2012). Another important control aspect is the medium's mass flow rate, where Badescu, 2007; Naik, Varshney, Muthukumar, & Somayaji, 2016; Shafieian, Khiadani, & Nosrati, 2019 have stated that obtaining a proper range will yield higher outlet temperatures and better efficiencies, in the other hand the lower the flow rate the inferior the collector's efficiency (Badar, Buchholz, & Ziegler, 2012).

Shifting from short term to long term heat storage can increase solar coverage from 15 – 30% to 40 – 100% (Böszörményi & Šiváková, 2012) and shifting from conventional decentralised natural gas heat units to centralised solar heating plants, provides environmental and economic cost decrease of about 85 and 16%, respectively (Schach & Wollstein-Lehmkuhl, 2018; Tulus, Boer, Cabeza, Jiménez, & Guillén-gosálbez, 2016). Seasonal heat storage units, being a long term storage, pretend to harvest heat from the warmer periods of the year to ensure portions or totality of heat demand during colder ones (John A. Duffie, 2013). This technology has several possible applications, apart from the convectional use for district heating, can be used for drying, space heating, desalination and power generation (Lehr, 2016). It has been shown by Fan, Huang, Andersen, & Furbo, 2017; Lehr, 2016 that

combining a seasonal heat storage unit with heat pumps in combined heat and power plants (CHP) can increase the pump's coefficient of performance (COP) and combining cooling and heating storage facilities can induce heat profits from one another as Balaras, Dascalaki, & Aidonis, 2010 have done.

Among seasonal thermal energy storage (STES), different configurations have been studied, from boreholes, aquifers, tanks and pits (Dincer & Ezan, 2018; John A. Duffie, 2013). Pit thermal energy storage (PTES) units are widely used in the world (IEA, 2011, 2015), where the main implementation aspects are: appropriate volume, heat losses, stratification mechanisms and heat demand (Kumana, 2017; Lavan & Thompson, 1977; Shafieian et al., 2019). Heat losses can be decreased with insulation materials, where Pfeil & Koch, 2000 have shown a good environmental and economical comprise using recycled granulated glass and Thomas Schmidt et al., 2018 demonstrated that usage of insulation in the bottom and walls of a pit is not economically feasible.

In order to provide a good heat quality to the user, stratification strategies can be taken, in which Andersen, Furbo, & Fan, 2007; Campos Celador, Odriozola, & Sala, 2011; Furbo, Vejen, & Shah, 2005 have studied different stratification mechanisms, from inlet stratification pipes, to entry and exit streams' location. This last approach, it is generally set with hot streams on the top of the units and return cold loads on the bottom. Even though these strategies take place, Abdoly & Rapp, 1982; Neupauer & Kupiec, 2017 state that de-stratification tends to happen as time passes mainly due to diffusion and heat losses and mostly during the charging period.

The mediums that can be used in STES units are generally grouped as: sensible, where there is no phase change (Böszörményi & Šiváková, 2012); latent, inversely to sensible ones where the system profits from lower volume need due to energy absorption during the phase change period (Gordon, 2013); thermochemical, generally done with the use of salts, harvesting energy from chemical changes (Druske, Fopah-lele, Korhammer, & Urs, 2014). Thermochemical mediums are still a new and evolving technology (IEA, 2011, 2015). Nowadays the main focus is upon sensible mediums, with water commonly as medium, due to high specific heat, low cost and easy access (John A. Duffie, 2013).

This study aimed to understand the energetic and economic feasibility of a coupled pit seasonal heat storage unit with U-pipe shaped evacuated solar collectors, to ensure the heat demand of a tomato growth greenhouse facility on the region of Aarhus, Denmark, by creating a numerical model relying on the system's heat balance in the software MATLAB R2019a. The modelling of the PTES was done with a multi-node approach, connected to a group of evacuated solar collectors with variable flow rate in the range of $[0.001:0.020] \text{ kg/s}$ in order to ensure the heat demand of a single-span double-wall polycarbonate (PC) greenhouse, oriented East-West and with a ground area of 2000 m^2 , under the optimal temperatures range of $[18:22] \text{ }^\circ\text{C}$. All calculations were done based on the weather data conditions of the city of Aarhus, hourly, on an yearly-basis, in order to obtain a dynamic approach of the greenhouse's necessities and available solar irradiation intermittency. From Figure 1-1, it can be seen the configuration of the components of the overall system, where an ETC

collector field and a greenhouse (GH) have been connected to a PTES unit, with the greenhouse profiting from the stored heat, mainly during winter periods and night time.

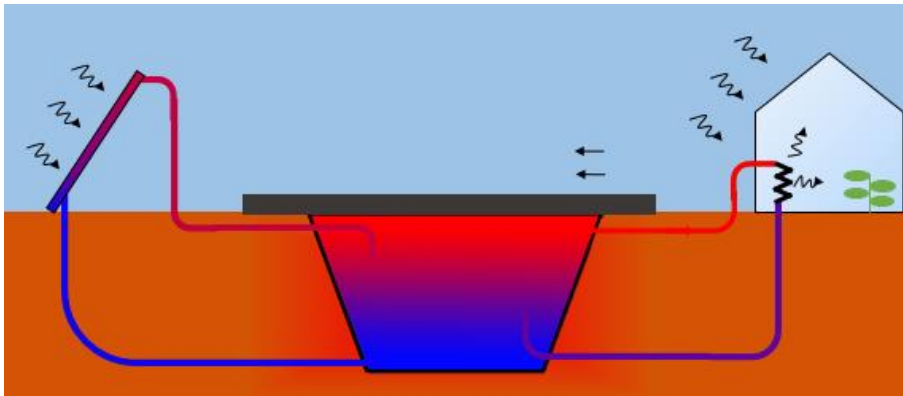


Figure 1-1 Demonstration of solar pit storage unit connected to ETC field and greenhouse

1 OVERVIEW

In this chapter it will be given a general knowledge of the main subjects approached in this thesis, i.e. solar irradiation taking a role on the charging of both solar collectors and greenhouse and the notion of seasonal heat storage, solar collectors and greenhouses.

1.1 SOLAR IRRADIATION

Thermal radiation is a small portion of the radiation spectrum, concentrated between 0.1 – 100 μm , which includes most part of infrared radiation, a small region of ultra-violet (UV) and all the visible band, as can be seen in Figure 1-1. This region, concentrates the beams that induce temperature variations when hitting particles (Vliet, 2000). The main beam length of solar irradiation is between 0.1 – 0.3 μm and it is why solar irradiation is such an important thermal energy source (Bergman, Lavine, Incropera, & Dewitt, 2011).

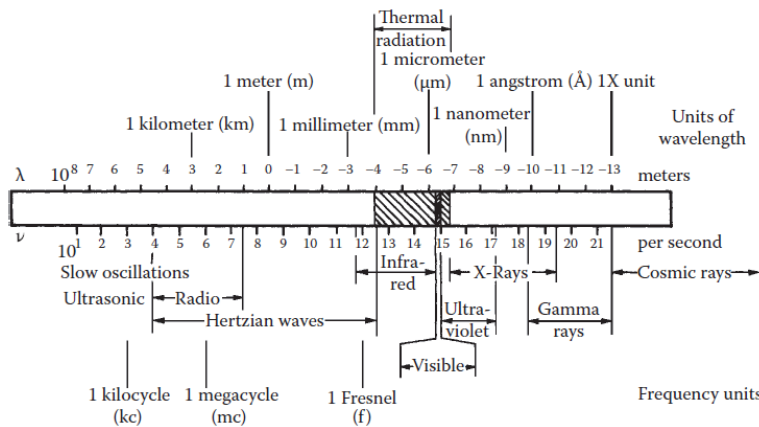


Figure 1-1 Electromagnetic radiation spectrum (Vliet, 2000)

An important aspect to this study is to understand the solar capacity for thermal technologies such as greenhouses and seasonal heat storage systems as their source. Solar irradiation is highly variable on a year-round and dependent on the location where a given unit is to be input (ASHRAE, 2017; Gordon, 2013).

Knowing the solar availability is the start-up aspect to initiate the simulations, for this, weather conditions need to be known, i.e. ambient temperature, wind speed, global and diffuse irradiation, latitude and longitude, which can be obtained through weather data or the ASHRAE Clear Sky Model (Vliet, 2000). In this project the year-round weather data for the city of Aarhus was used and dependent on the orientation of each surface and its inclination, the hourly available energy can be found, by means of solar angles shown in Figure 1-2, where α , β , i , a_s , a_w , are solar altitude angle, surface tilt angle, incident angle, solar azimuth angle and surface azimuth angle, respectively and further explained in chapter 2.1.2.

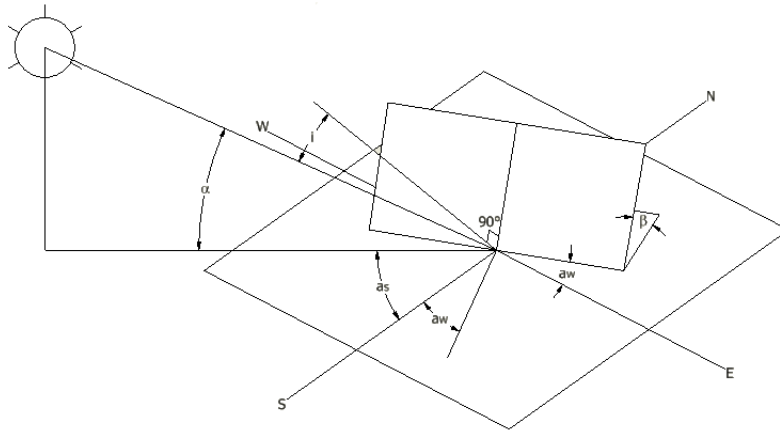


Figure 1-2 Solar angles on a tilted surface

The incoming thermal radiation can be obtained as seen in Figure 1-3 where the global irradiation, composed by direct, diffuse and reflected beams, reach a surface and are spread dependent on the material's irradiative properties, being divided into portions of reflected, absorbed and transmitted radiation (Gordon, 2013).

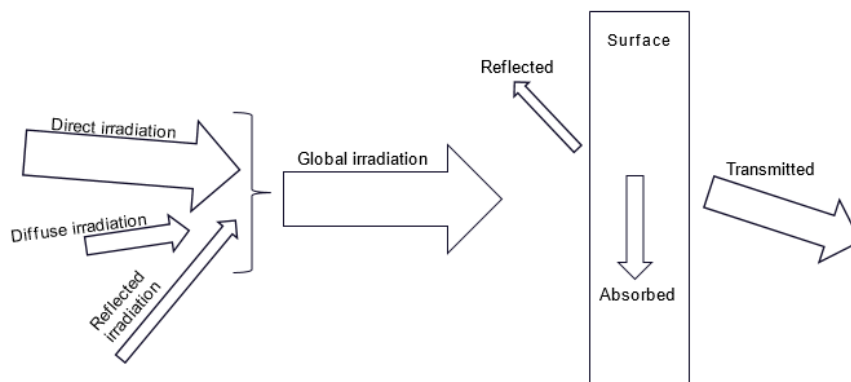


Figure 1-3 Global irradiation composition and its impact on a surface

If the case is to have high transmitted solar irradiation either on a greenhouse or a solar collector, the better the irradiative transmission of a passing surface like glass or non-opaque polymers (Akelah, 2013). If high absorption of solar irradiation is the purpose, then a material with high absorptivity and low transmissivity is required like coated metal fins in solar collectors. So dependent on the purpose, the proper material should be chosen to take advantage on this energy source (Vliet, 2000).

In the end, using solar irradiation as form of heat, requires knowledge on local weather conditions, solar and surface angles of the housing covers, yearly irradiative pattern and a good selection of materials for each thermal means, to make solar thermal technologies feasible.

1.2 GREENHOUSE

For more than 20 years now, the farming industry realized that by controlling the stress factors on crop production, it was possible to endure crop production with lesser impact from environmental uncertainties and year-wise growth even for seasonal plants, simply by controlling the climate of the housing, thus creating a greenhouse effect (Kittas et al., 2013).

Greenhouses' most important component is its coating, which allow lower bands, around $0.3 - 3 \mu m$, of thermal radiation to pass through and retains bigger wavelengths, around $0.3 - 80 \mu m$, thus increasing its internal energy and consequently its temperature. Figure 1-4 shows a basic schematic of this facilities, where the incoming solar radiation is filtered by the wall's surfaces and bands of bigger wavelengths are trapped in the housing, creating the greenhouse effect, being possible to achieve higher temperatures than the surrounding areas (Griepentrog, Blackmore, & Vougioukas, 2006).

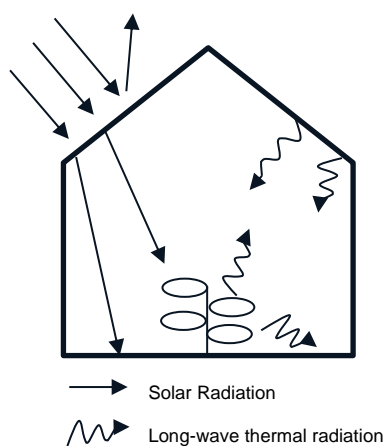


Figure 1-4 Demonstration of greenhouse effect

The greenhouse structural configuration dictates the likelihood of a broader life cycle expectancy and of profitability (Von Zabeltitz, 2011). Given that, the specific inner and outer climate conditions will dictate which will be the optimal design. Roofing type, volume, ground area, mechanical structure and cover materials are some of the more important aspects when modelling a greenhouse (Akelah, 2013).

Two main types of roof are widely used (Von Zabeltitz, 2011):

- Round arched, which has high wind resistance and simple construction, but at the cost of accumulation of condensates in the highest most horizontal point causing water dripping and higher solar diffusion;
- Point arched, that reduce dripping and necessity of mechanical structures, but at the cost of more wind resistance.

In terms of area and volume, the higher the volume the nicer the interior climatic conditions are kept for the same ground area, although it will require higher heat supply (Singh & Tiwari, 2010). For this, solutions have been accessed, like the shift from single to multi-span greenhouses, yielding higher crop density and the possibility of mechanical ventilators usage

for interior quality control, causing on other hand an increase in building costs significantly (Von Zabeltitz, 2011).

In this study, the housing layout from Arabkoohsar, Farzaneh-Gord, Ghezelbash, & Koury, 2017; Farzaneh-Gord, Arabkoohsar, Bayaz, & Khoshnevis, 2013 was used, given its wide volume per ground area, single-span to decrease construction costs and point-arched roof providing better dripping than round-arched and structural advantages, shown in Figure 1-5.

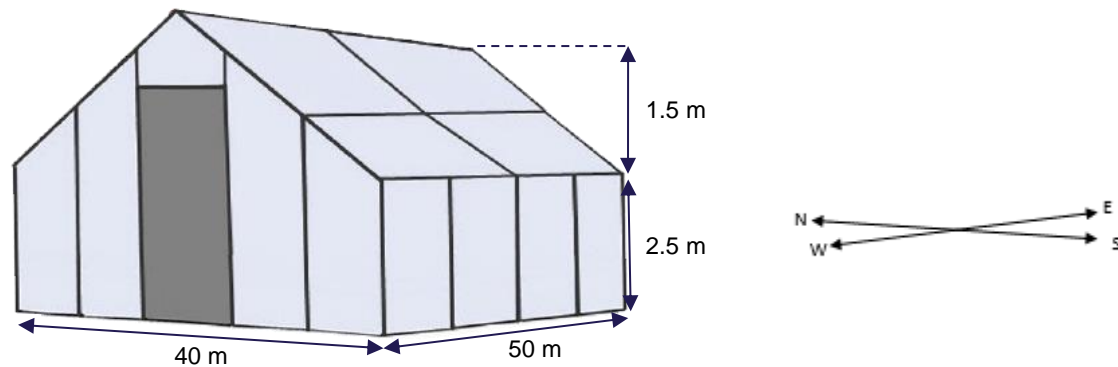


Figure 1-5 Greenhouse configuration and dimensions

There are a variety of covering materials commonly used in the industry, with some listed in Table 1-1, which the appropriate choice has many conundrums: depending on location, yearly weather conditions, price and product's thermal and mechanical characteristics. Glasshouses contribute to high construction costs, so to make them feasible, large volumes are considered to decrease costs by unit area and heat losses through the walls, as Kittas et al., 2013; Saltuk & Artun, 2019 have stated that the average glasshouse's area in the Netherlands in 2003 were of 1.5 hectares.

An alternative to glass usage is a polymer, providing a possibility of using single or multilayer (double or triple) separated by gaseous bulks, generally filled with air, where Verhaegh, 1996 has stated that 30 – 40% of heating savings can be achieved by shifting from single to double inflating polyethylene (PE). Along with the plastics' cheap factor, when compared to glass, it also has the ease of manipulation to provide specific wave-length blockages/passes, by altering opacity or colour, depending on the expected solar irradiance and interior desired climatic conditions (Von Zabeltitz, 2011).

Table 1-1 Transmittance values for different cover materials (adapted from Von Zabeltitz, 2011) and overall heat transfer coefficient (adapted from ASAE, 1998)

Material	Thickness, δ (mm)	Solar Transmittance		Transmittance (%) (IR wavelengths 3 – 20 μm)	U-value ($\text{W}/\text{m}^2\text{K}$)
		Direct light (%)	Diffuse light (%)		
Glass	4	89 – 91	82	0	5.4
PE single	0.1 – 0.2	89 – 91	81	25 – 60	6.2
PC double-wall	12	80	76	0	3.2 – 3.6

Polymers like polyethylene (PE) and polycarbonate (PC) are of common employment in greenhouses, where the first one represents a very cheap solution with good thermal properties, but at the cost of low life span, with 3-4 years life, depending on the weather conditions, being more desired for mild climates like the Mediterranean (Akelah, 2013; Dilara & Briassoulis, 1998). In northern European countries, the mechanical resistance becomes of more importance and therefore rigid plastics like PC are more appropriate and even though the building costs are larger, in double-layered PC films it is possible to achieve high transmittance of low wave-length thermal radiation and sustain heavy wind and rain loads (Griepentrog et al., 2006; Kittas et al., 2013; Von Zabeltitz, 2011). As also stated by Çaylı & Akyüz, 2019; Krug et al., 2020; Nelson, 2004, double-layers can reduce energy consumption by 40% from single-layer greenhouses.

The material considered for the study at hand was a double-layered PC due to rigid characteristics given the winter harsh conditions of Denmark, with good transmittance of low band solar irradiation and high capture of big thermal radiation bands within the house, with specifications shown in Table 1-2 where δ , τ , ρ and k are thickness, transmissivity, reflection coefficient and conduction heat transfer coefficient, respectively and the subscript *PC*, polycarbonate.

Table 1-2 Cover material's characteristics used in simulations.

Material	Unit	Double-wall PC
δ	mm	8
τ_{PC}	-	0.84
ρ_{PC}	-	0.1
k_{PC}	W/m^2K	0.21

1.3 SEASONAL HEAT STORAGE

Energy usage and availability occur sometimes in different time frames, for example at night time, dams still run while the energy requirements are very low, which brings the necessity of storing energy, so water back-pumping has been implemented (Rehman, Al-Hadhrami, & Alam, 2015). The intermittency between necessity and attainability led to a variety of technologies of energy storage such as electrical, potential and heat (Abdi, Mohammadi-ivatloo, Javadi, Khodaei, & Dehnavi, 2017).

Heat storage facilities are divided into two main purposes: short or long term storage and both function through charging-storing-discharging cycles as demonstrated in Figure 1-6. Long-term thermal energy storage (TES) start with a charging period where an energy source such as solar, works as energy input during the warm season, followed by storing period when the requirements are kept, like maximum temperature or pressure, and in the winter/cold season the unit discharges in order to attain the output necessities. This process is done when the demand and availability of heat do not meet, therefore called seasonal thermal energy storage (Vliet, 2000).

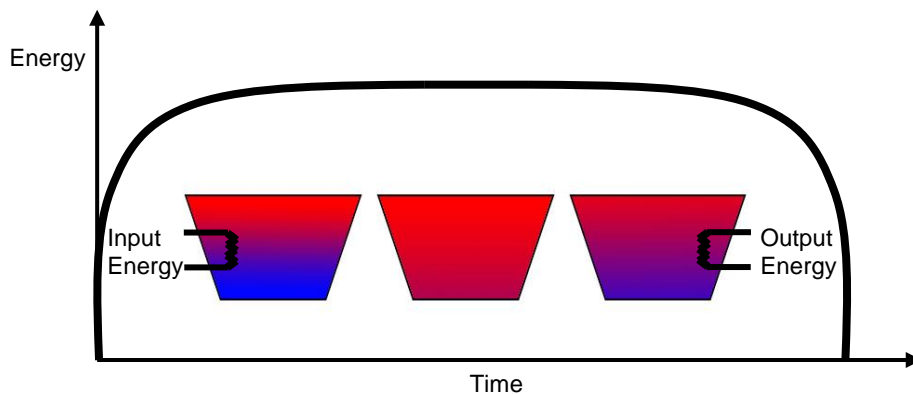


Figure 1-6 Seasonal heat storage unit cycle

One of the main energy sources in STES facilities is solar energy that is harvested and converted into heat by means of a storing medium. For this, different deposit configurations can be used, in Figure 1-7 some of the most used ones are demonstrated (IEA, 2015; Krasimirov Pavlov, 2014; Pavlov & Olesen, 2012; T. Schmidt, Mangold, & Müller-Steinhagen, 2004):

- Water Tank Storage is the more versatile unit, given it is a built tank, partially or totally underground, with insulated walls and cover, allowing a variety of internal thermal considerations with low impact from its surrounding conditions, thus acquiring high storage performances, although, it comes with high construction costs;
- Aquifer Thermal Energy Storage presents a good purpose when there is demand for both heating a cooling, where wells filled with minerals such as gravel, sand and limestone, make into the ground-water layer, and extract the cold medium from one well and charge it and store it in the hot one. When the cooling medium is required, the cycle is reversed.
- Pit thermal energy storage (PTES) presents as a ground hole surrounded by soil with low thermal diffusivity, such as clay, separating the medium with a waterproof material like polypropylene and insulated at least on the top cover. These facilities are widely used due to low implementation costs and low temperature variations of the ground surroundings having as example the *MARSTAL Sunstore* facilities already in use in Denmark.

The configuration chosen in this project was a PTES unit, taking into account the successful cases shown by Fan et al., 2017; PlanEnergi, 2013, 2015.

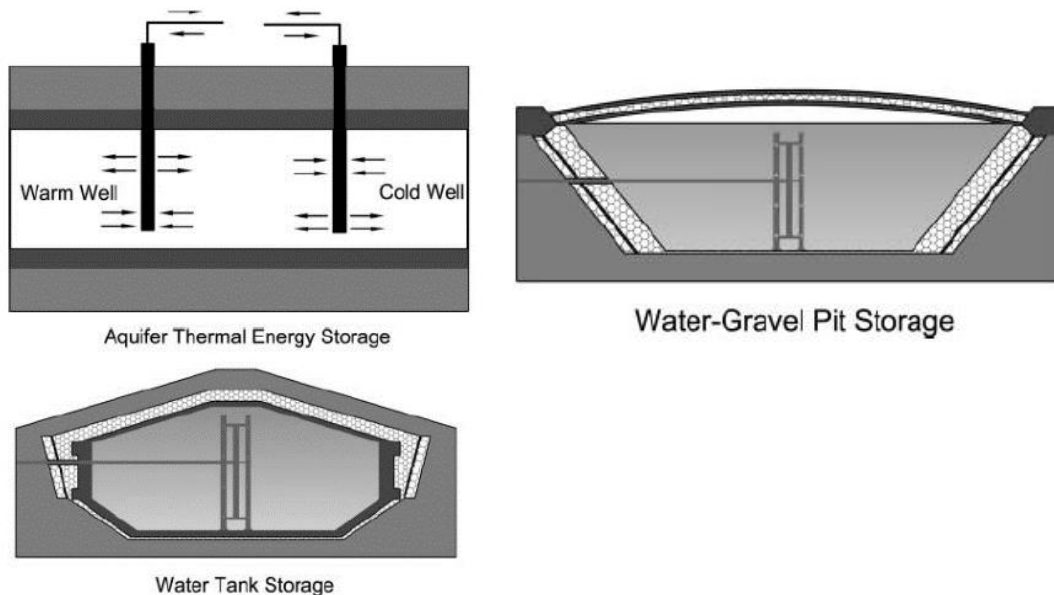


Figure 1-7 Different types of underground thermal energy storage (Pavlov & Olesen, 2012)

In order to store energy on a medium, one must know its thermal properties given it will also dictate the volume necessity for a specific demand (Dincer & Ezan, 2018). There are 3 main families of mediums: sensible storage, where the medium harvest energy with no phase change; latent storage, where energy is stored with lower density changes using phase-change materials (PCM); usage of for example salts, which will harvest the energy by changing chemically, so called thermochemical storage. (Dincer & Ezan, 2018; Jamshidian, Gorjian, & Far, 2018) The dimensions are crucial to be minimized given the construction costs, and from Figure 1-8, it is clear that thermochemical are the more prominent, with higher energy capacity by unit volume, followed by latent and lastly sensible ones.

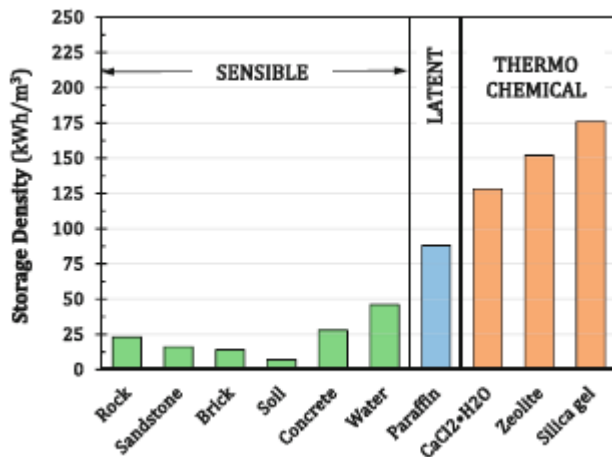


Figure 1-8 Volumetric net power rate for different usual mediums used in Seasonal heat storage (Dincer & Ezan, 2018)

The costs of construction and maintenance are not only dependent on volume, and as shown in Figure 1-9 and Table 1-3, can be concluded that thermochemical storage is a technology still in development, in which IEA, 2011 reported that so far it is not clear the advantages of using it in large scale units for conventional climate control. In the other hand, STES systems are widely known, with capital advantages and stability.

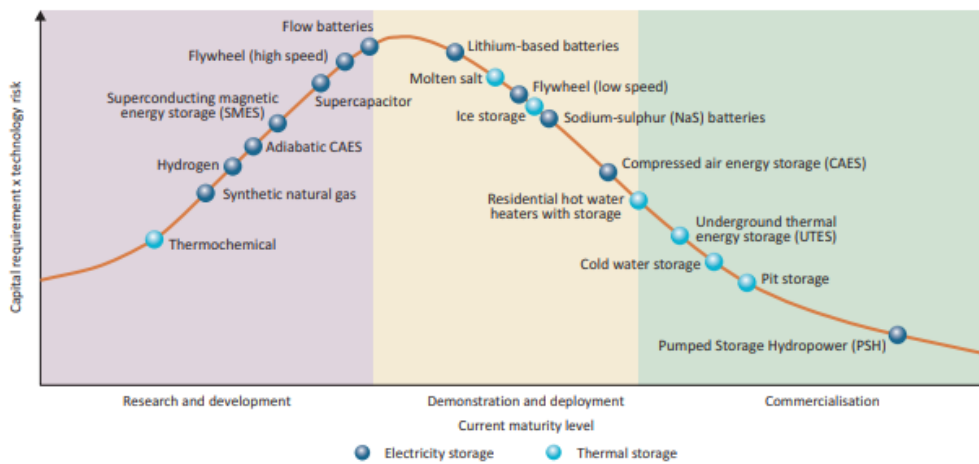


Figure 1-9 Ratio of capital requirement and risk over the maturity level of different energy storage systems (IEA, 2011)

Analysing Table 1-3, latent storage has advantages in energy rate by volume unit and efficiency, when compared with sensible ones, but in the other hand, its capital cost can reach up 3 times higher than sensible and with shorter storage periods, turning it less desirable for high energy capacity units (Dincer & Ezan, 2018; John A. Duffie, 2013).

Table 1-3 Characteristics of different heat storage technologies

Thermal	Power Rate (MW)	Storage Period	Efficiency (%)	Capital Costs (\$/kW)
Sensible STES	0.001-10	Day-month	50-90	3400-4500
Latent STES	0.001-1	Hour-day	75-90	6000-15000
Thermochemical	0.01-1	Hour-month	75-100	1000-3000

For a wide variety of cases PTES systems use water as medium, given its high specific heat among liquids, easy access and low cost, but it can induce corrosive effects on the mechanical materials of the setup. When not purified, it has a high degrading rate, where PlanEnergi, 2015 reported that the low grade purification of the water led to a degradation of the running pipes on the first year of implementation, and in cold climates may even freeze, thus decreasing the capacity of the unit (Dincer & Ezan, 2018). As stated by Thomas Schmidt et al., 2018, the water requires a previous purification, where salts are removed and the PH is elevated to 9.8, in order to be useful as a heat storage medium.

The medium used in this thesis was water, considering that it was purified to the standards reported by Thomas Schmidt et al., 2018.

Heat storages can have different thermal distributions by means of temperature gradient along the vertical axis, called stratification. This phenomenon is very important to increase the quality of provided energy when discharging a tank and can either be naturally done or induced by mechanical stratifiers, for example when using different levels of charged flow inlet pipes like some storage tanks used in the industry as demonstrated in Figure 1-10 (John A. Duffie, 2013).

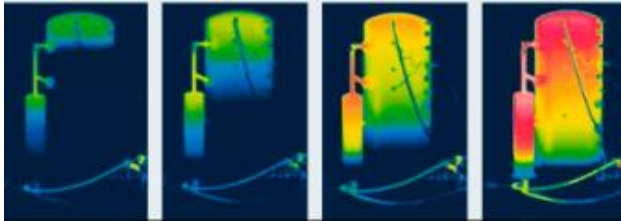


Figure 1-10 Stratification mechanism used in the industry (Tisun, 2020)

When natural stratification is carried, a free convection approach takes place, where a charged medium entering a tank will follow its path dependent on density, creating a temperature gradient (Jiji, 2006), allowing usage of the colder medium from the tank's bottom to the charging unit, thus increasing the energy provider's performance. (Abdoly & Rapp, 1982) The general configuration of naturally stratified tanks, shown in Figure 1-11, is optimal given that the incoming charged water always enters from the top and leaves at the bottom/colder region, thus depriving high levels of mixture between hot and cold zones (John A. Duffie, 2013).

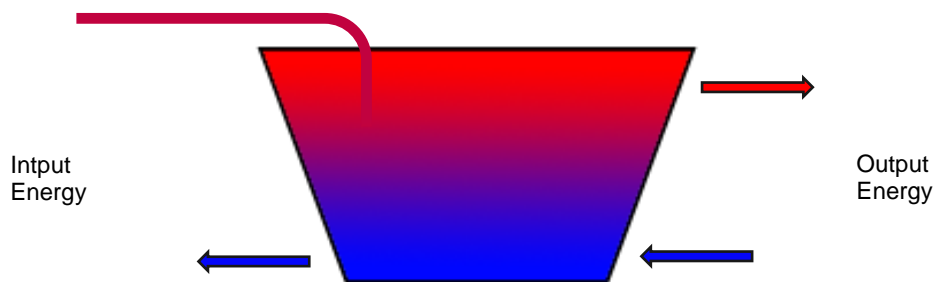


Figure 1-11 Input and output flows to provide stratification mechanism

Creating the higher barrier between cold and warm regions will yield bigger efficiency of permutation to the user (John A. Duffie, 2013). The barrier, also called thermocline region, demonstrated in Figure 1-12 (a) and (b), determines the stratification quality, i.e. the shorter the thermocline region, the better and bigger heat quality availability.

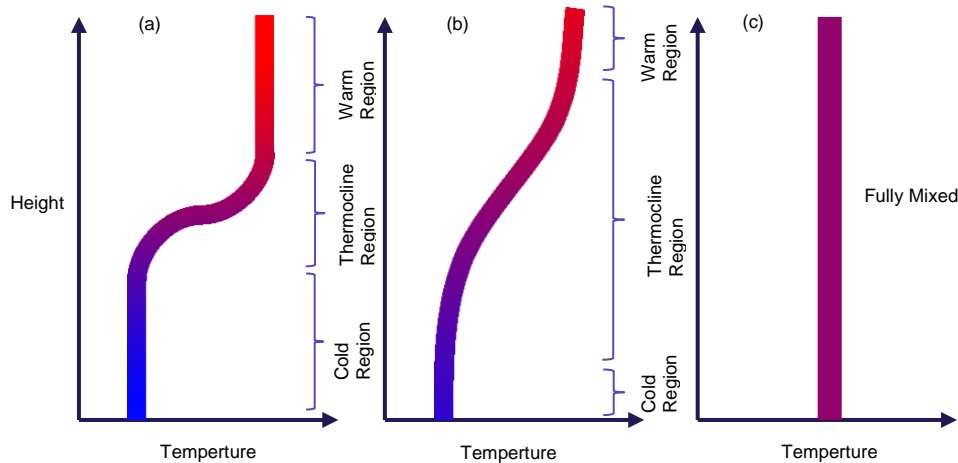


Figure 1-12 Thermocline region width depending on the stratification level

In an optimal situation, like in Figure 1-10 where a stratification mechanism is used, demonstrated in Figure 1-12 (a), the thermocline region tends to be short, but the more common and likely circumstance is seen in Figure 1-12 b, where the thermocline region agglomerates most of the tank's height. As stated by John A. Duffie, 2013; Lavan & Thompson, 1977, throughout time tanks tend to de-stratify due to diffusion and become fully-mixed as is demonstrated in Figure 1-12 (c).

Modelling stratification levels properly and accurately can be a challenge and for this some models are in use nowadays like multi-node and plug-flow approaches. For this study, the multi-node approach was taken, where the volume is divided into N number of sub-volumes of equal height. Discretising the pit allows to run the model's equations in each discretised region and reach a more accurate and realistic thermal behaviour (Cadau, Lorenzi, Gambarotta, & Morini, 2019; John A. Duffie, 2013).

1.4 SOLAR COLLECTORS

Housing and water heating, electricity production, greenhouse crop growth and industrial processes are some of the many cases that solar energy can provide and have been around for years (Böszörményi & Šiváková, 2012; Z. Tian et al., 2018; Tulus et al., 2016). The main technology in use due to its efficiency and profitability, its low cost and short payback periods, is the solar collector. From evacuated pipes to flat plates, this product is in rampage in the aid of long-term heat storage units (Chung, Park, & Yoon, 1998; Krasimirov Pavlov, 2014; Schach & Wollstein-Lehmkuhl, 2018; Xu et al., 2014).

Solar collectors, as seen in Figure 1-13, constitute of a layered unit, starting with a glass/plastic material with high thermal radiation transmissivity, a metal fin layer to harvest the transmitted irradiation, with high absorption coefficient and low emissivity, like coated-copper. These two materials are separated by a bulk area, with a gas like air or argon or in a vacuum, in order to create an inner thermal barrier with the outside conditions, and finally

a piping array attached to the cover to absorb the energy collected and provide it to the running fluid within. (Vliet, 2000)

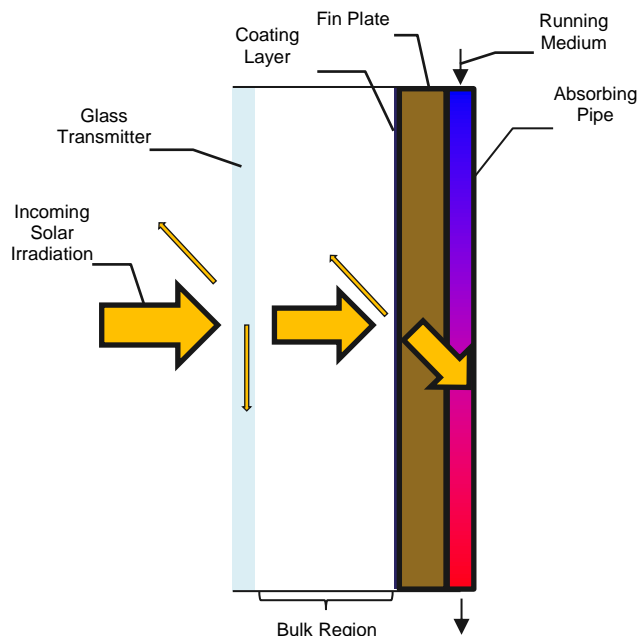


Figure 1-13 Solar collector configuration

Solar collector's array types are divided in three different families (Gordon, 2013; Vliet, 2000): Flat plate collector (FPC), with a flat configuration with the characteristics of Figure 1-13, having generally air in the bulk region and insulated in the bottom. These collectors work very well for low temperature purposes ($80^{\circ}\text{C} <$) and in mild climates given its losses by conduction and convection from the bulk to surroundings; Evacuated tube collectors (ETC), where the solar transmitter layer and absorber plate are separated by an evacuated bulk region, which highly prevents the heat losses, thus yielding better performances than FPC (Jamshidian et al., 2018). This technology has the advantages of working well in cold climates and can reach high temperatures to the point of changing phase, although costs are greater than FPC. Compound parabolic concentrator (CPC) is a configuration where a parabolic reflector, with low transmittance and absorptivity, surrounds the absorbing cover, reflecting most of the incident solar irradiation onto the cover. This technology can be done in various ways, by aggregating an ETC with CPC (Kumar & Rosen, 2011).

Given the Danish low temperature climate and with prospect of achieving the highest yield possible from solar irradiation, the evacuated tube collectors were chosen for the study, as Maraj et al., 2019; Yan, Zhang, & Shao, 2013 suggest that in cold climates ETC tends to have higher efficiency than FPC, given its lower losses and lower aperture area necessity for the same output energy.

The ETC have two usual kinds of arrays: Metal-fin-vacuum tubes and Dewar tubes, the first one can be displayed as shown in Figure 1-14 where a glass envelope allows solar waves to pass through, keeping the bigger beams or far-infra-red region (FIR) in. A cover plate will conduct the absorbed heat onto a pipe with a medium flowing and a vacuum region between

glass and metal fin (Vliet, 2000). Even though it has very little thermal resistances in-between the outside and medium, it is expensive and difficult to evacuate the glass and the fin due to connections (Gordon, 2013).

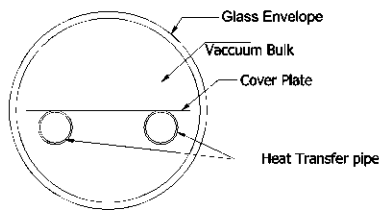


Figure 1-14 Basic configuration of a metal-fin-vacuum tube with flat fin plate

The Dewar tubes, are more complex, composed by concentric borosilicate glass, separated between vacuum and generally connected to an inner fin-plate absorber and pipe with flowing fluid as demonstrated in Figure 1-15. The fins are coated in order to decrease radiation emission to the surroundings (Badar, Buchholz, & Ziegler, 2011; Kumar & Rosen, 2011) and made of materials with high absorption coefficients and conductivity, as is copper or aluminium (Vliet, 2000). This kind of collector setup is a cheaper layout due to the easier way to induce the vacuum from glass to glass and so it was the layout chosen for the modelling process (Gordon, 2013).

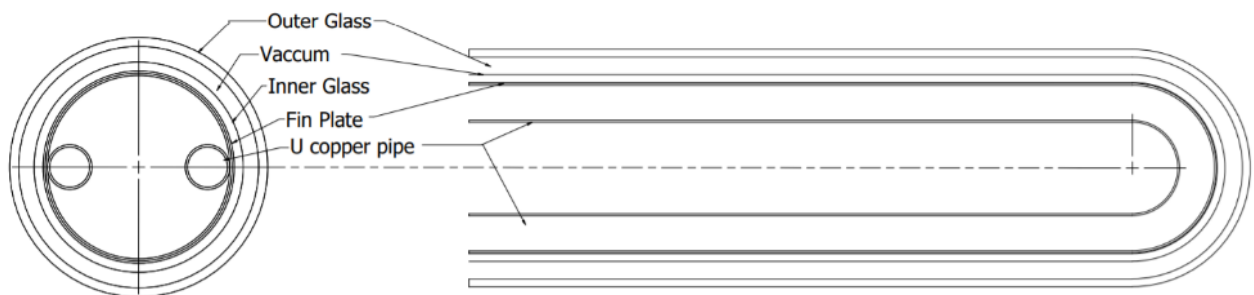


Figure 1-15 Cross-sectional schematic and side-view of the solar collector configuration used in simulations

The ETC was chosen from the work done by Y. Gao et al., 2014, as a Dewar tube with U-pipe shaped (UpETC) with characteristics shown in Table 1-4, where the subscripts col , g , p and t stand for collector, glass, plate and tube, respectively.

Table 1-4 UpETC dimensions and thermal properties

L_{col}	1.8 m
d_g	0.058 m
d_p	0.047 m
d_t	0.010 m
α_p	0.9
τ_g	0.95
F'	0.986
medium	H_2O (distilled at PH 9.8)

2 ENERGY ANALYSIS

Modelling a system as complex as coupling solar irradiation with greenhouse facilities, solar collectors and seasonal heat storage units require a base strategy given the interdependency of ones system with the others, so an energetic analysis is generally conducted by means of energy balance, as has been done by Chalabi & Zhou, 1996; Li, Chen, Luo, Zhang, & Xue, 2010; Lund & Peltola, 1992; Taki, Rohani, & Rahmati-joneidabad, 2018.

The subjected methodology was taken by modelling each subsystem by itself and finally combining them together in order to create a dynamic interaction, year-wise, profiting or affecting from one another. The subsystems were modelled for every j^{th} hour of an entire year, considered as:

- Greenhouse
- U-pipe shaped evacuated tube solar collector field
- Pit seasonal heat storage unit

All the subsystems are dependent on the climate conditions of the site to be set up. For this Figure 2-1 to Figure 2-4 show the year-round ambient temperature, wind velocity and direct and diffuse radiation. This study's modelling was set to start on the beginning of the charging period or warm season and finish at the end of the cold period, so all time-dependent graphs are provided from the 1st of April – 31st of March.

Table 2-2, Table 2-3 and Table 2-4 have variables with a bar, that account for an averaging value, where subscripts *annual*, *warm*, *cold*, *max* and *min*, stand for annual time interval, warm period of the year, cold period, maximum recorded value and minimum recorded value, respectively, with time intervals shown in Table 2-1.

Table 2-1 Time interval for each subscript in hours and days of the year

	Subscript		
	<i>warm</i>	<i>cold</i>	<i>annual</i>
Time interval (<i>hours</i>)	[1:4392]	[4393:8760]	[1:8760]
Time interval (<i>days</i>)	1 st April - 31 st September	1 st October – 31 st March	1 st April – 31 st March

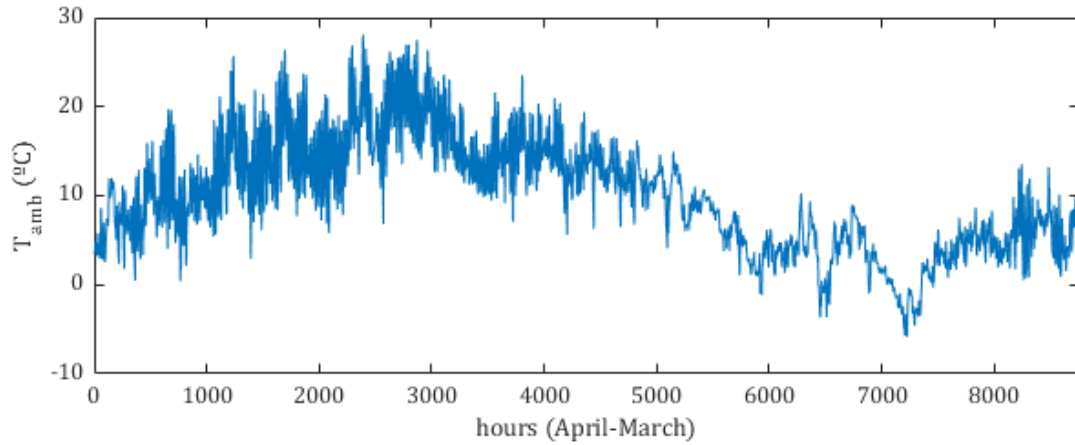


Figure 2-1 Graphical representation of the project ambient temperature

Table 2-2 Ambient temperature averaged, maximum and minimum values

\bar{T}_{annual}	\bar{T}_{warm}	\bar{T}_{cold}	T_{max}	T_{min}
°C				
9.9	14.0	5.7	28.1	-5.9

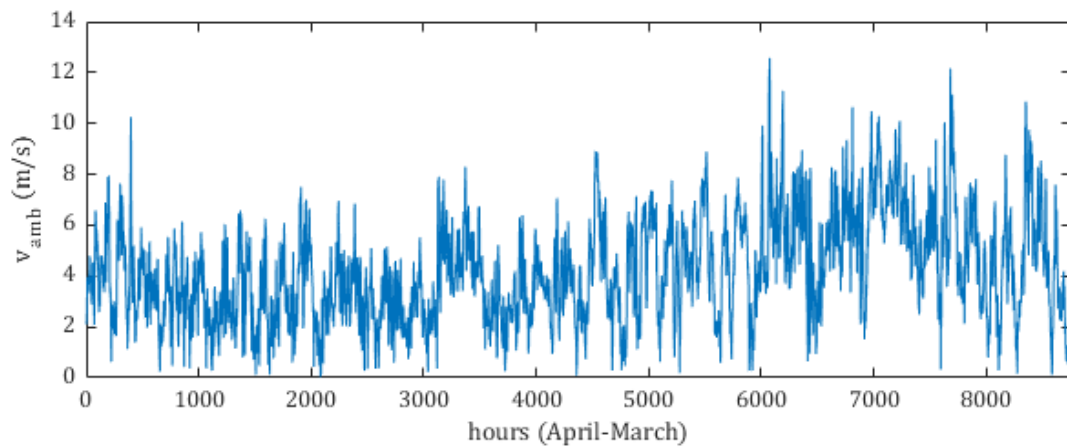


Figure 2-2 Graphical representation of the project wind velocity

Table 2-3 Wind velocity averaging, maximum and minimum values

\bar{v}_{annual}	\bar{v}_{warm}	\bar{v}_{cold}	v_{max}	v_{min}
<i>m/s</i>				
4.2	3.4	5.0	12.6	0.04

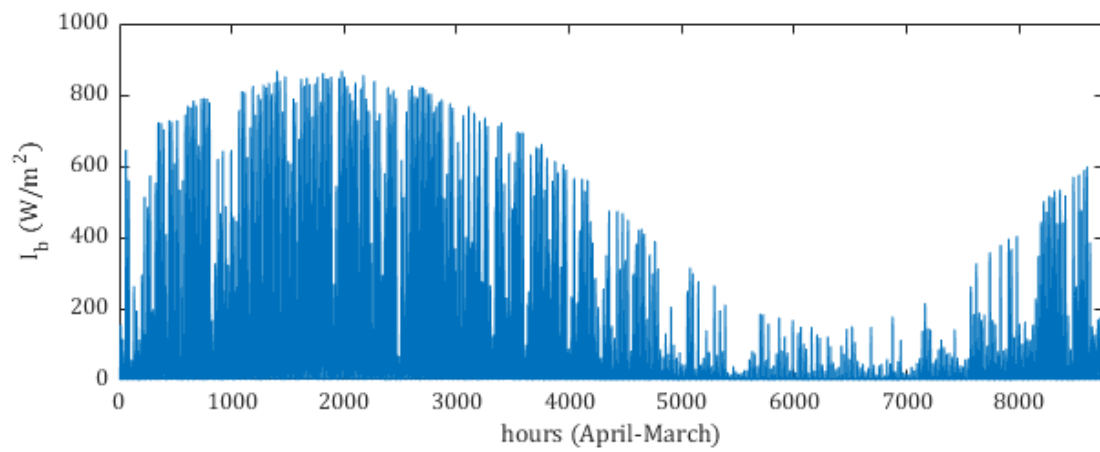


Figure 2-3 Graphical representation of the direct solar irradiation

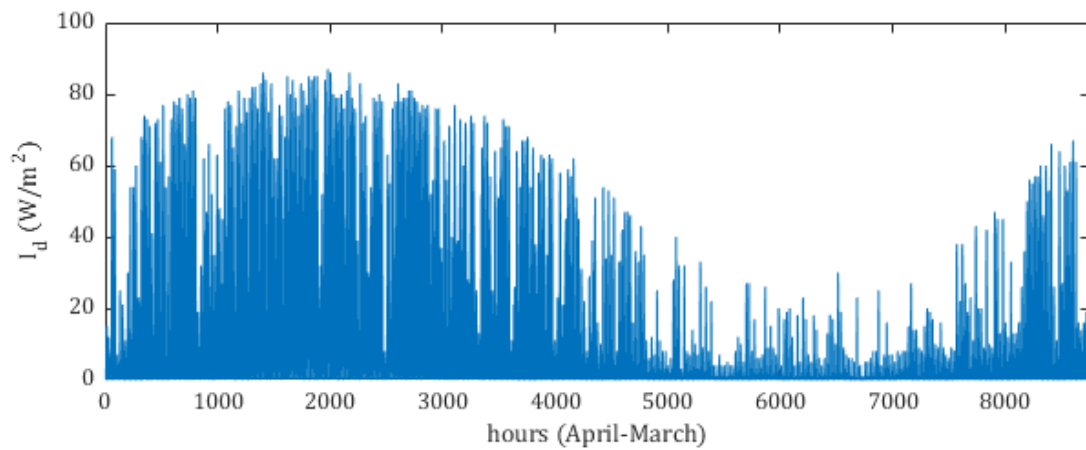


Figure 2-4 Graphical representation of the diffuse solar irradiation

Table 2-4 Direct and diffuse irradiation averaged, maximum and minimum values

	$\bar{I}_{b_{annual}}$	$\bar{I}_{b_{warm}}$	$\bar{I}_{b_{cold}}$	$I_{b_{max}}$	$I_{b_{min}}$
W/m^2	213.4	285.5	164.9	868	0
	$\bar{I}_{d_{annual}}$	$\bar{I}_{d_{warm}}$	$\bar{I}_{d_{cold}}$	$I_{d_{max}}$	$I_{d_{min}}$
	12.6	21.0	15.7	87	0

The soil temperature is known to vary dependently on the nearby surface's climatic conditions and as suggested by Cui et al., 2011, it will vary less with depth increase. For this, taking the work of Baggs, 1983, for northern hemisphere areas, equation 0.1 was obtained, which provides the daily temperature of the soil, T_{soil} , at a given depth. The variables T_m , ΔT_m , k_v , A_s , x , α_{soil} , t and t_0 stand for average annual air temperature, ground temperature differential, assumed as 0.85 °C, vegetation coefficient of shade over the ground, assumed 0.9, amplitude of the annual average air temperature, ground depth, soil average thermal diffusivity assumed as 0.96 mm²/s from Pagola, Jensen, Madsen, & Poulsen, 2017, time in days of the year and phase of air temperature wave, assumed as 21 days, respectively.

$$T_{soil}(x, t) = (T_m + \Delta T_m) - 1.07K_v A_s \exp(-0.00031552x\alpha_{soil}^{-0.5}) \cos\left[\frac{2\pi}{365}(t - t_0 - 0.018335x\alpha_{soil}^{-0.5})\right] \quad (0.1)$$

where $A_s(t') = (\bar{T}_{max_{t'}} + \bar{T}_{min_{t'}})/2$ with $t' = month$

The soil temperature was computed for every day of the year with the depth interval [0:0.5:-16] m and its average monthly temperature can be seen in Figure 2-5, where, as suggested, differs more significantly with time when the depth is small and tending to a constant value as it goes deeper, being less ambient temperature dependent as depth increases.

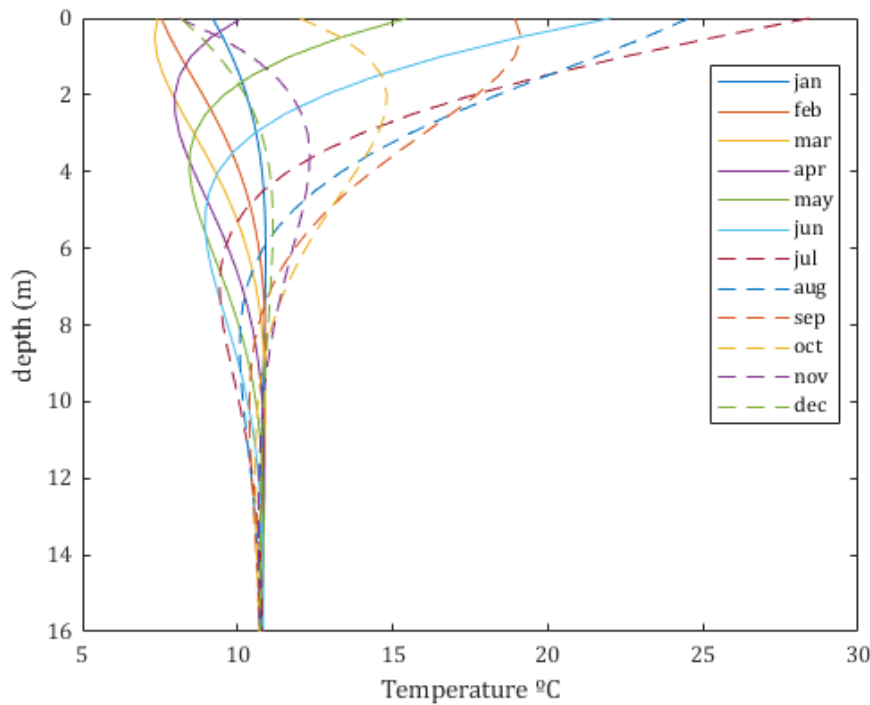


Figure 2-5 Average monthly soil temperature dependent on depth

When modelling a coupled system STES-ETC the Volume-Area ratio is determinant to achieve the best performance, lower necessity of aid from external power sources and best budget (Schach & Wollstein-Lehmkuhl, 2018). In this project the complexity was no different, given the amount of parameters that make a system work at its best and at great computation expenses when conducting an optimization procedure on a multi-objective situation as complex as comparing optimal generated heat, along with lowest need of auxiliary energy and highest profitability with variant values like fluid flow rate, number of series, volume of pit, area of solar collection and interdependency from the pit's temperature gradient and dynamic in-and-out heat fluxes.

As stated by (O. Paksoy, 2005), seasonal water heat storage units are an expensive technology and due to that, the number of possible charging-discharging cycles constitutes of one of the major factors to reduce production costs, given that if a unit can produce two cycles per year-period, then its necessity of STES volume will decrease. For this, the required heat to produce a complete cycle was determined, and from that an iterative process was conducted in order to determine the possibilities of diminishing its volume and area of collection.

The greenhouse needs of heat during the cold period were determined and set as demand of the seasonal heat storage. For this, it was possible to determine the volume necessity, using the internal energy heat balance equation with the volume in evidence as shown in equation 0.2, where $\dot{Q}_{GH,cold}$, dt , ρ , cp and dT are the greenhouse heat demand from the cold period, calculated as the sum of heat demand during the cold period shown in Table 2-1, time interval of 3600 seconds, water's density, specific heat and temperature difference

between maximum storage temperature, here set as 85 °C and initial storage temperature, assumed 20 °C, thus a dT of 65 °C.

The total heat demand during the cold period was of 375 *MWh*, thus reaching the conclusion of a need of 4900 m^3 to complete a cycle of heat demand of the greenhouse.

$$V_{STES} = \frac{\dot{Q}_{GH,cold} dt}{\rho c p dT} \quad (0.2)$$

From the work done by Schach & Wollstein-Lehmkuhl, 2018 a number of Volume-Area ratios along with series of collectors ranging 10:40 were used to run the modelling. From the results, a net present value (NPV) economic analysis was done with respective costs shown in chapter 3 and an interest rate of 5% was considered. Denoting that a further explanation of the net present value is given in chapter 3, being the net cash flow between cash outflows and inflows over a lifetime period. Thus the higher positive net cash flow, the better the profitability of the system and the sooner the payback period (Mahmood Farzaneh-Gord et al., 2013).

In Figure 2-6, can be seen four plots with different number of N series, and in each a group of points dependent on the volume of the pit and area of collectors, having as output the net present value. Comparing the series, it seems that having from 20 to 30 collectors yields the higher amount of profitable outputs, whereas for 10 and 40, the system did not present very promising revenues. Another aspect is the fact that for the volumes of 2000 and 2500 m^3 , the higher profits were obtained with V/A ratios bellow 1 and the volumes of 1500 and 3000 m^3 did not yield any promising net cash flows.

The remaining non showed bounds simply did not fulfil the greenhouse's requirements or did not provide any positive outcome, regardless of the series or V/A ratios. In the end, the series that provided the best NPV with lower needs of auxiliary heat was the case of volume equal to 2000 m^3 , with 3000 m^2 and 20 collectors in series, thus concluding it as the optimal case, under the studied values.

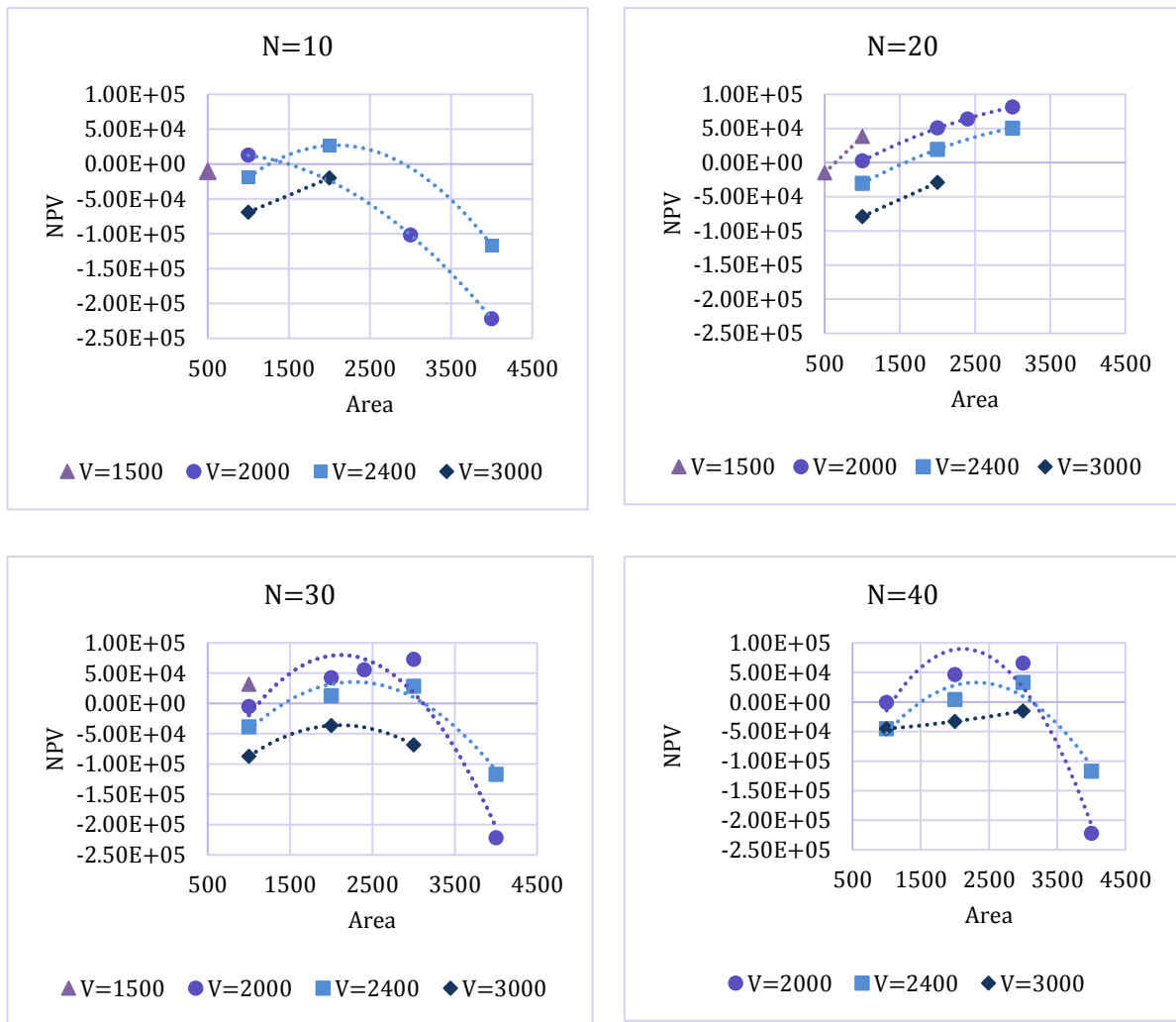


Figure 2-6 Net present value variation dependent on number of N series, area of solar collectors and volume of pit

In order to understand the thermal behaviour of a charging discharging storage unit, the model was run for an initial year-period and re-run for a second one with initial inputs from the outputs of the last hour of the first period, in order to understand if there would be thermal stability in the tank, thus concluding it as a quasi-stable any-year-round case (Gordon, 2013; Sharma, Tiwari, & Sorayan, 1999).

Finally, this study was conducted with temperature dependent physical characteristics like thermal conductivity, density, dynamic viscosity, specific heat and Prandtl number for the intervenient fluids, i.e. water and air, which were obtained from data tables from ASHRAE, 2017, plotted and with the aid of Microsoft Excel 2013, respective regressions were determined to obtain a valid equation for any temperature case in-between the project's working bounds, as shown in the annex section, chapter 8 .

2.1. GREENHOUSE ENERGY MODELLING

Greenhouse effect is a phenomenon from which life would not exist, where the atmosphere creates a thermal barrier for a certain wavelength of solar rays, retaining them and so creating an acclimatized region. Greenhouse farming works with the same purpose, but in this case, the microclimate created is dependent on the requirements of the growing produce, housing materials and on the site that it is placed (Von Zabeltitz, 2011) .

In Figure 2-7, the main products grown in greenhouses in Denmark are shown, where the three main ones account for potted plants, cucumber and tomatoes.

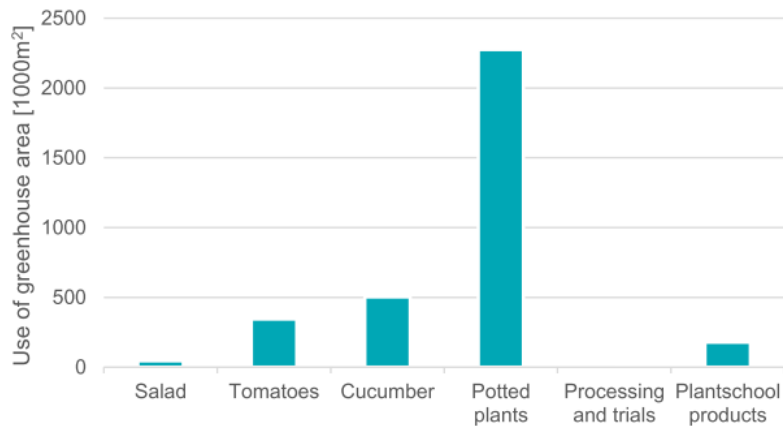


Figure 2-7 Greenhouse product quota in Denmark for the year of 2014 (Danish Agrifish Agency, 2016)

According to Danish Agrifish Agency, 2016; statista.dk, 2020, tomato production is one of the main crops that requires greenhouse implementation for its production, given its optimal temperature like Heuvelink, 1995; Mariani, Cola, Bulgari, Ferrante, & Martinetti, 2016 suggest, rounding 18 – 22 °C and with a critical temperature of 5 °C. As demonstrated in Figure 2-1, especially during the winter period, the ambient temperature falls below the critical temperature, thus making tomato production unlikely to thrive in conventional outside farming, risking freezing and consequential rupture in production. Given this, a temperature pattern was created based on a linear relation between interior temperature and available irradiation.

It was assumed that the highest temperature would be reached on the hour of the highest irradiation and inversely reaching the lowest temperature when there was no radiation. The graphical representation can be seen in Figure 2-8 and the consequent equation 0.3 from the linear regression.

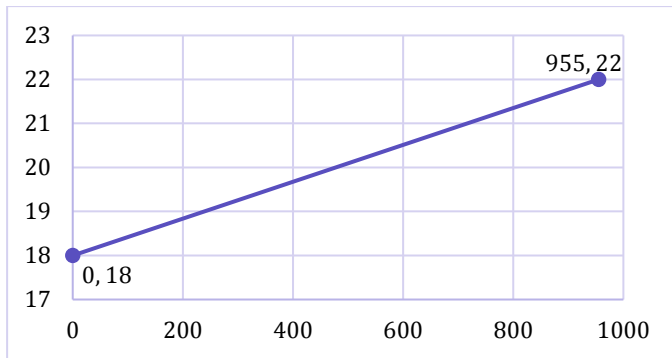


Figure 2-8 Graphical representation of linear regression taken for the determination of the greenhouse temperature

$$T_{GH} = 0.0042(I_b + I_d) + 18, \quad \text{where } 0.0042 = \frac{1}{4} \max(I_b + I_d) \quad (0.3)$$

Finally, the inlet temperature pattern had the trend shown in Figure 2-9.

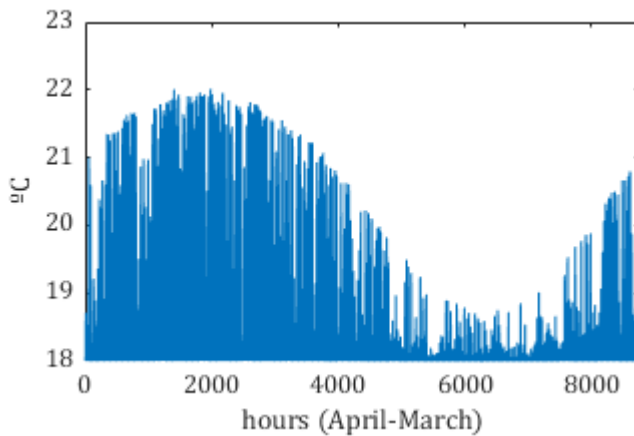


Figure 2-9 Internal greenhouse temperature pattern dependent on global solar irradiation

2.1.1 Greenhouse Energy Balance

The energy balance of a greenhouse is dependent on the required energy to create an optimal microclimate for crop growth, respective heat losses to the surrounding areas and ventilation demand (Bartzanas, Tchamitchian, & Kittas, 2005; Kooli, Bouadila, Lazaar, & Farhat, 2015; Pasgianos et al., 2003). As input energy, two sources are generally assumed: the solar irradiation on the housing and, when this provenance does not meet the requirement for a healthy crop production, an external energy source is used to heat up to the specific project temperature. In some cases, especially for latitudes upper than 40°, it is common that during the winter time the crop necessity of heat from solar irradiation is not met and so it is needed another energy source than direct solar (Griepentrog et al., 2006; Kittas et al., 2013; Von Zabeltitz, 2011).

Taking into account the work done by Arabkoohsar et al., 2017; Mahmood Farzaneh-Gord et al., 2013, the heat balance equation to model the greenhouse unit can be seen in equation 0.4, where the left side is in respect to energy input, and the right side the unit's energetic costs, where the subscripts *green* and *vent* are the greenhouse energy demand and the heat loss/gain from the required ventilation, respectively.

$$\dot{Q}_{solar} + \dot{Q}_{green} = \dot{Q}_{loss} + \dot{Q}_{vent} \quad (0.4)$$

In order to start each term's analysis, some assumptions need to be done:

- Inner temperature set by a pattern in the bounds of [18–22]°C (Heuvelink, 1995; Mariani et al., 2016)
- 3 renovations per hour from ventilation (Von Zabeltitz, 2011)
- Uniform internal temperature dependent on convection, conduction and radiation heat transfer with greenhouse elements and surroundings (Sharma et al., 1999)
- Soil temperature dependent upon thermal penetration depth (Baggs, 1983; Bircher, Skou, Jensen, Walker, & Rasmussen, 2012)

2.1.2 Solar Irradiation

As already mentioned in chapter 1.2, in order to model a greenhouse facility, the influence from the solar radiation is the prime subject to attain. According to ASHRAE, 2017; Bergman et al., 2011; John A. Duffie, 2013; Vliet, 2000, the solar irradiation on a housing depends on its dimensions, location, walls and cover orientation and irradiative properties of covering material, so this section is based on these referencing, taking into account the latitude, L , of the city of Aarhus, Denmark, of $56.16^\circ N$, longitude of $10.2^\circ E$ and the altitude assumed as sea level, i.e. 0 m .

The greenhouse orientation is also an important aspect and so it was oriented East-West, having the bigger wall area North-South oriented as suggested by Ben Ali, Bouadila, & Mami, 2018; Jain & Tiwari, 2003; Taki, Rohani, & Rahmati-joneidabad, 2018. The dimensions, tilted angles, β , and surface azimuth angles, α_w , are stated in Table 2-5, bearing that no direct irradiation was considered for the north wall as sun moves East-South-West in the northern hemisphere.

Table 2-5 Areas of Wall and cover, tilted angles and surface azimuth angles

Orientation	Wall				Cover	
	South	North	East	West	South	North
Area (m)	125	125	130	130	1002	1002
β (°)	90	90	90	90	4.2	-4.2
a_w (°)	0	0	90	-90	0	0

Given the cover is both tilted positively and negatively, the distinction was made by south and north cover, respectively.

During a year, the Earth's translation around the sun is elliptical and at the same time, its polar axis around which it spins, is not perpendicular with the globe's motion around the sun as seen in Figure 2-10, so thrown solar waves reach ground at different angles in different times yearly.

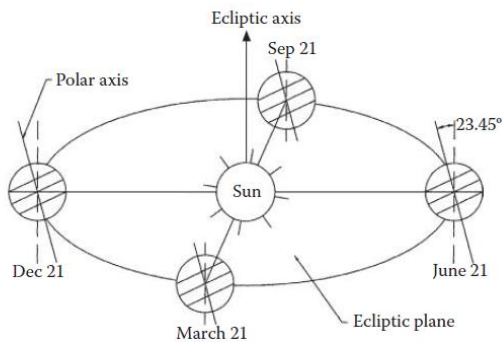


Figure 2-10 Earth's translation around the sun and respective created beam angles

The angle that demonstrates the sun rays' deviation upon Earth is called declination, δ , obtained by equation 0.5, in respect to each day of the year, $n \in \{1:365\}$, starting from the 1st of January. (Salahaldin Na'man, Haval Y. Yacoob, 2013)

$$\delta = 23.45 \sin[360(284 + n)/365^\circ] \tag{0.5}$$

From Figure 2-11 it can be seen the declination variation year-wise, where at the 21st of June and December are shown at the picks, 23.45° and -23.45°.

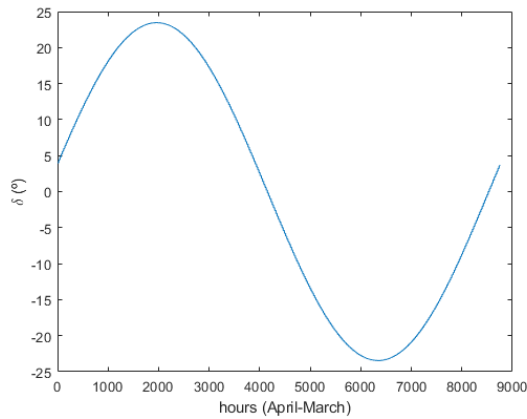


Figure 2-11 Declination angle variation during a year

The sun’s motion, from an Earth’s view, translates on 360° per day, at 15° per hour and for a given location it is known that the noon, i.e. the hour with the sun at its highest point in the sky, it is considered as the degree zero. This is called the hour angle, h_s and it is obtained considering that for every hour there is a -15° deviation from noon towards morning and the inverse after noon, as given by equation 0.6 (Abood, 2015).

$$h_s = (h - 12) \times 15^\circ \text{ where } h \in \{1:24 \text{ hours}\} \tag{0.6}$$

Once obtaining the hour angle, the latitude and the declination for every given hour, it is possible to determine the solar altitude, which is the angle made between the solar rays and the ground’s surface and can be obtained by equation 0.7 (Parkin, 2010).

$$\sin \alpha = \sin L \sin \delta + \cos L \cos \delta \cos h_s \tag{0.7}$$

As demonstrated in Figure 2-12, the sun has its highest point during the warm period and in the other hand the lowest during the cold period.

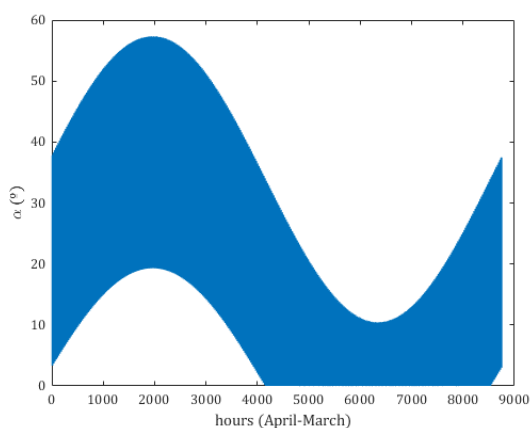


Figure 2-12 Solar altitude angle variation year-round

Finally, the incidence angle, i , as demonstrated in Figure 1-2, is the angle made between the direct rays and the zenith of a certain surface. As shown in equation 2.9, the incidence angle

is dependent on the solar altitude, surface tilt, surface zenith and the solar azimuth, a_s , angles. This last one is the deviation from the ground projection rays with the south, given by equation 0.8, which will vary along the day.

$$\sin a_s = \frac{\cos \delta \sin h_s}{\cos \alpha} \quad (0.8)$$

The formulation to obtain the incidence angle is shown in equation 0.9 and will be determinant to obtain the direct irradiation, I_b , dependent on each specific k surface (Vliet, 2000).

$$\cos i_k = \cos \alpha \cos(a_s - a_{wk}) \sin \beta_k + \sin \alpha \cos \beta_k \quad (0.9)$$

As stated in chapter 1.1, the direct, diffuse and reflected irradiation depend on the sun's motion daily and year-round (Ulgen, 2006). So, knowing the direct and diffuse irradiation on site, as seen in Figure 2-3 and Figure 2-4, will help determine the global irradiation on each surface by means of equations 0.10, 0.11, 0.12 and 0.13, where the subscript k is correspondent to the orientations specified from

The sum of global irradiation for each surface and overall greenhouse are shown in Table 2-6 and can be seen that the south surface and cover account for more than 70% of the total irradiation per unit area on a greenhouse with the configuration of this project, hence proving the higher yield using East-West orientation, as suggested in literature.

Table 2-6.

$$I_{b_k} = I_b \cos i_k \quad (0.10)$$

$$I_{d_k} = I_d(1 + \cos \beta_k)/2 \quad (0.11)$$

$$I_h = I_b \sin \alpha + I_d \quad (0.12)$$

$$I_{r_k} = \rho_{soil} I_h (1 - \cos \beta_k)/2 \quad (0.13)$$

In equation 0.13, the soil's reflectivity, ρ_{soil} , was assumed as 0.2, as a surface composed of grass as suggested by Vliet, 2000 and given the cover's location it was assumed $I_{r_{cover}}$ as null.

Once obtaining the direct, diffuse and reflected irradiation for each k^{th} surface, the global irradiation, I_{global} , could be obtained, as seen in equation 0.14.

$$I_{global_k} = I_{b_k} + I_{d_k} + I_{r_k} \quad (0.14)$$

The sum of global irradiation for each surface and overall greenhouse are shown in Table 2-6 and can be seen that the south surface and cover account for more than 70% of the total irradiation per unit area on a greenhouse with the configuration of this project, hence proving the higher yield using East-West orientation, as suggested in literature.

Table 2-6 Yearly direct, diffuse, reflected and global irradiation dependent on surface

	Unit	Wall			Cover		Greenhouse
Orientation	-	South	East	West	South	North	-
I_b	kWh/m^2	508.4	250.5	261.0	653.6	552.5	2226.3
I_d		55.7	55.7	55.7	111.2	111.2	389.5
I_r		71.7	71.7	71.7	0	0	215.1
I_{global}		635.9	378.0	388.5	764.8	663.7	2830.9

The solar irradiation kept in the greenhouse is dependent on the cover's transmissivity, τ_{PC} , the area of each surface and the absorptivity of the material in which it irradiates, α_{soil} . The soil's absorptivity was assumed as 0.7 as suggested by Arabkoohsar et al., 2017. For this the heat provided to the greenhouse through solar is shown in equation 0.15 (Arfaoui et al., 2017).

$$\dot{Q}_{solar} = \alpha_{soil} \tau_{PC} \sum_k A_k I_{global_k} \quad (0.15)$$

Finally, it was concluded that the highest and lowest peaks of solar irradiation were spotted during the mid-summer and mid-winter, respectively, thus inferring that the highest need of energy from the heat storage will be during the winter period, and lowest during summer, as shown in Figure 2-13.

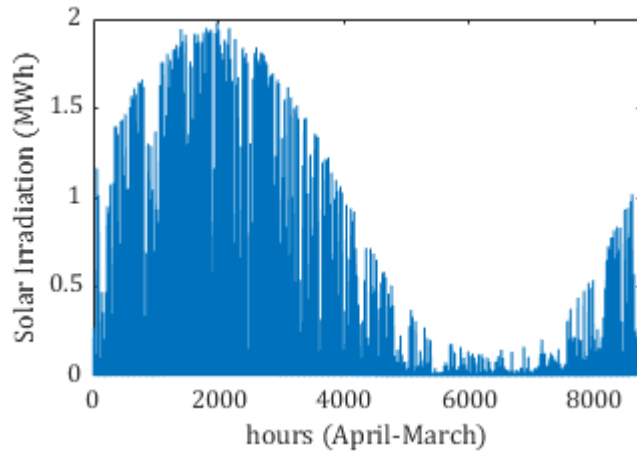


Figure 2-13 Solar heat flux in the greenhouse

By understanding the heat fluxes from solar upon the greenhouse it is viable to determine the losses and necessities, when needed, to maintain the microclimate stable as initially determined in the project.

2.1.3 Greenhouse Losses

The heat losses in a greenhouse are generally towards the ambient surroundings and ground soil. In the ambient surrounding case, the thermal properties and dimensions of covering material are of most importance, alongside with the outer weather conditions like wind. Regarding the soil, it has been demonstrated in the beginning of chapter 0, that soil temperature variations are much lower than ambient, thus inducing lower losses (Taki et al., 2018).

In order to obtain the energy lost to the environment, equations 0.16, 0.17 and 0.18 were used as in work done by Çaylı & Akyüz, 2019; Jain & Tiwari, 2003, dependent on the overall heat transfer between inner and outer conditions, where subscripts *in – soil* and *in – amb* stand for between inner and soil conditions and inner and outer ambient conditions, respectively.

$$\dot{Q}_{loss} = \dot{Q}_{loss_{soil}} + \sum_k \dot{Q}_{loss_k} \quad (0.16)$$

$$\dot{Q}_{loss_k} = U_{in-amb_k} A_k (T_{in} - T_{amb}) \quad (0.17)$$

$$\dot{Q}_{loss_{soil}} = U_{in-soil} A_{soil} (T_{in} - T_{soil}) \quad (0.18)$$

The overall heat loss coefficients between interior and ambient, U_{in-amb} , were determined considering a series of thermal resistances as shown in equation 0.19 and Figure 2-14, where h_{in_k} is the inner convection heat transfer coefficient, k_{PC} the polycarbonate's heat conduction coefficient and h_{amb_k} the outer convection heat transfer coefficient. (Dincer & Ezan, 2018; Nijskens, Deltour, Coutisse, & Nisen, 1984)

$$\frac{1}{U_{in-amb_k}} = \frac{1}{h_{in_k}} + \frac{\delta_{PC}}{k_{PC}} + \frac{1}{h_{amb_k}} \quad (0.19)$$

The calculations of the convection coefficients were based on the correlations given by Bergman et al., 2011.

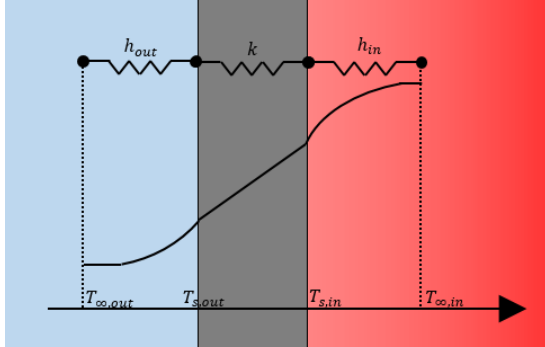


Figure 2-14 Demonstration of thermal resistances of two bulk regions separated by a surface and temperature evolution

Determining a convection coefficient is widely done in literature as dependent on the flow's thermal conductivity, k , the surface's characteristic length, L , and the Nusselt number, Nu . The Nusselt number is determined as the ratio between thermal convective and conductive effects on a medium, as shown in equation 0.20, assuming it as an averaged Nusselt number, given that the surface temperature is kept constant, independent on the length (Bergman et al., 2011; Nijskens, Deltour, Coutisse, & Nisen, 1985).

$$\bar{h} = \frac{\overline{Nu} k}{L} \quad (0.20)$$

In the case that it is not possible to determine the flow's orientation and given that each area of this study is non-quadratic, the characteristic length, $L_c = 4A/P$, was used, where A and P are the surface area and perimeter, respectively, replacing the length, L .

External convection cases like the one where ambient flows interact with a hot surface is often dependent on the wind's velocity (Ben Ali et al., 2018; Bergman et al., 2011), hence knowing if the flow passing through is laminar or turbulent is determinant to choose the proper correlation of convection coefficient, thus the adimensional number Reynolds, Re , from equation 0.21 was determined for this purpose, where ρ, v and μ are the air's density, velocity and dynamic viscosity, respectively.

$$Re = \frac{\rho v L_c}{\mu}, \text{ where } \begin{cases} Re > 5e6 \rightarrow \text{Turbulent} \\ Re \leq 5e6 \rightarrow \text{Laminar} \end{cases} \quad (0.21)$$

With the flow regime perceived, the Nusselt number, \overline{Nu}_{out} , was obtained assuming external convection on vertical/inclined surfaces from Bergman et al., 2011 as seen in equation 0.22, dependent on Reynolds and Prandtl numbers, Pr .

$$\overline{Nu}_{out} = \begin{cases} 0.664Re^{1/2}Pr^{1/3}, & \text{if } Re \leq 5e6 \\ 0.037 \left(Re^{4/5} - 871 \right) Pr^{1/3}, & \text{if } Re > 5e6 \end{cases} \quad (0.22)$$

The internal convection coefficient was determined similarly, however in this case, the internal convection coefficient was assumed as free convection, which states that the created convection is more significantly dependent on buoyancy forces than on kinetic ones, so it will be majorly dependent on its temperature and density gradient within a space while a thermal equilibrium is being reached as time passes, like Figure 2-15 shows. (Bergman et al., 2011)

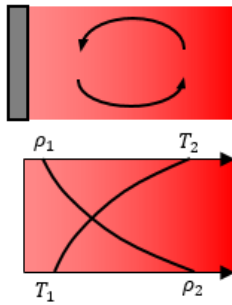


Figure 2-15 Convection phenomenon of a hot medium nearby a cold surface and temperature and density variation

Analog to the Reynolds number in forced convection, which determines the ratio of the effects of inertial by viscous forces, for free convection there is the Grashof number, Gr , that can be demonstrated by the ratio between the buoyancy forces and the viscous forces as seen in equation 0.23. The variables g, ν and β stand for acceleration of gravity, kinematic viscosity and expansion coefficient and subscripts s and ∞ the surface and buoyant fluid, respectively (Chauhan, 2018).

It should be noted that the air was assumed as ideal gas.

$$Gr = \frac{g\beta(T_s - T_\infty)L^3}{\nu^2}, \text{ where } \beta = \frac{1}{T} \text{ for ideal gas} \quad (0.23)$$

Once the Grashoff number is obtained, the proper correlation for Nusselt number can be chosen for vertical surfaces, seen in equation 0.24 from Bergman et al., 2011 and equation 0.25 as suggested by Fujii & Imura, 1972, appropriate for the cover's tilt inclination of 4° .

$$\overline{Nu}_{vertical} = \left(\frac{0.825 + 0.387Ra^{\frac{1}{6}}}{\left(1 + \left(\frac{0.492}{Pr} \right)^{\frac{9}{16}} \right)^{\frac{8}{27}}} \right)^2, \text{ where } Ra = GrPr \quad (0.24)$$

$$\overline{Nu}_{cover} = 0.58Ra^{1/5} \quad (0.25)$$

The Grashof number in equation is shown as dependent on the temperature between the bulk fluid, T_{in} , and the surface's temperature, T_s , but T_s is an unknown variable, given that it is also dependent on the conduction coefficient and the external convection coefficient. For this, an iterative process was created for every internal convection coefficient, where an initial guess was set for T_s^k and once calculated the k^{th} internal convection coefficient, the equality shown in equation 0.26 was used, to check the convergence criteria.

Noting that equation 0.26 was used assuming outer surface temperature as ambient temperature.

$$\frac{k_{PC}}{\delta_{PC}}(T_s - T_{amb}) = \bar{h}_{in}(T_{in} - T_s) \quad (0.26)$$

Finally, having all the Nusselt numbers for external forced and internal free convection, using equation 0.20, the convection heat transfer coefficients were obtained and further the overall heat transfer coefficients, U_{in-amb}^k by equation 0.19.

For the ground soil losses, the inner convection term was calculated by equation 0.27, appropriate for the case of free convection with upper hot flow on a cold surface from Bergman et al., 2011.

$$\bar{Nu}_{soil} = 0.52Ra_{soil}^{1/5} \quad (0.27)$$

As stated by Bergman et al., 2011, a given surface at constant temperature, T_s , or with induced heat flux nearby a big enough bulk region with different temperature, T_∞ , will create a thermal resistance that can be calculated by a transient semi-infinite conduction approach, where a temperature gradient will be created along the distance from the surface until the point at which no more heat propagation is possible (Cui et al., 2011; Lavine & Bergman, 2008; Povstenko, 2015).

Given the low soil thermal diffusivity and temperature variations, as suggested by Bergman et al., 2011, a transient conduction model was used, assuming that the soil will behave as a semi-infinite bulk region, thus creating a temperature gradient tending to its nearby surface temperature along time, as seen in Figure 2-16.

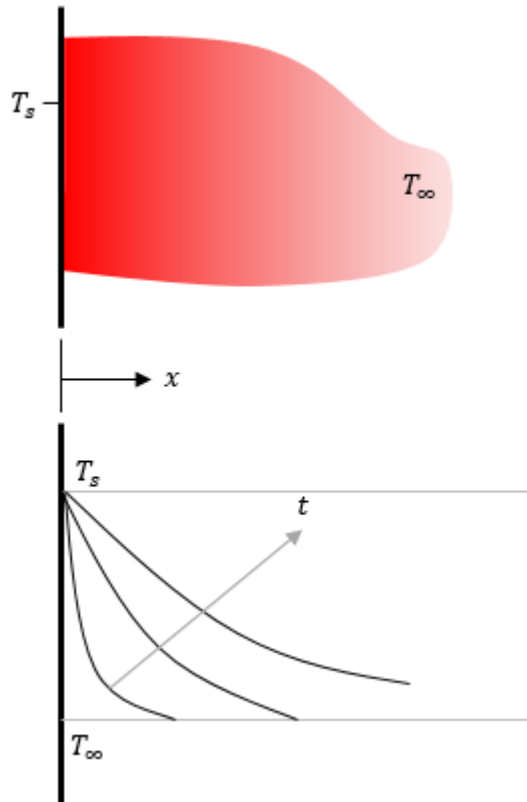


Figure 2-16 Thermal penetration on a cold semi-infinite region with a hot surface nearby

As shown in equation 0.19, the conduction thermal resistance is obtained by the ratio of the thermal conductivity, k , of a material by its thickness, δ . From Pagola, Jensen, Madsen, & Poulsen, 2017 some physical properties of the soil of western Denmark were determined, so the average thermal conductivity of the soil, k_{soil} , at saturated conditions was considered as 2.75 W/mK and a thermal diffusivity, α_{soil} of $0.96 \text{ mm}^2/\text{s}$.

The equation 0.28 for a semi-infinite bulk material with assumed constant surface temperature, is depending on the surface and soil temperatures, distance from the surface, δ_{soil} , time, t , and thermal diffusivity, α_{soil} .

$$\frac{T(x,t) - T_s}{T_{soil} - T_s} = \text{erf}\left(\frac{\delta_{soil}}{2\sqrt{\alpha_{soil}t}}\right), \quad \text{where } t = 3600 \cdot h \quad (0.28)$$

As Bergman et al., 2011; Lavine & Bergman, 2008 suggest, there are limitations for the thermal propagation on a bulk dependent on its physical and thermal characteristics, so the thermal penetration depth, δ_p , was suggested to be used as a barrier at the location x , when $\frac{T - T_s}{T_{soil} - T_s} = 0.9$, where this last condition states that when the variation between $T(x,t)$ and T_{soil} reach 90%, it can be assumed that there is no more possible thermal penetration the more that the distance increases, thus limiting equation 0.28 by equation 0.29.

$$\delta_p = 2.3\sqrt{\alpha_{soil}t} \tag{0.29}$$

The purpose of using the transient approach was to understand the proper distance, δ_{soil} , dependent on the thermal diffusion induced in the soil, so equation 0.28 was set into a loop for each time step, where different values of δ_{soil} were iterated until the value of $T(x,t)$ would reach a value close enough to T_{soil} , bearing in mind the limitation imposed by equation 0.29. Once the distance δ_{soil} was reached, it was possible to determine the conduction thermal resistance and thereafter the overall heat transfer coefficient, $U_{in-soil}$.

In Table 2-7 can be seen the average yearly U-value for each of the surfaces, showing the polycarbonate walls had almost identical ones and with a very small heat transfers between interior and the soil, thus demonstrating that the temperature gradient created on the soil from the greenhouse acted as thermal barrier, thus yielding a huge impact on the heat loss calculations.

Table 2-7 Average yearly overall heat transfer coefficient for each of the greenhouse's barriers

$\bar{U}_{in-amb_{NS}}$	$\bar{U}_{in-amb_{EW}}$	$\bar{U}_{in-amb_{cover}}$	$\bar{U}_{in-soil}$
W/m^2K			
1.28	1.28	1.23	0.03

Finally, the calculation of the greenhouse's losses was done via equation 0.16, where its values' variability through time can be seen in Figure 2-17.

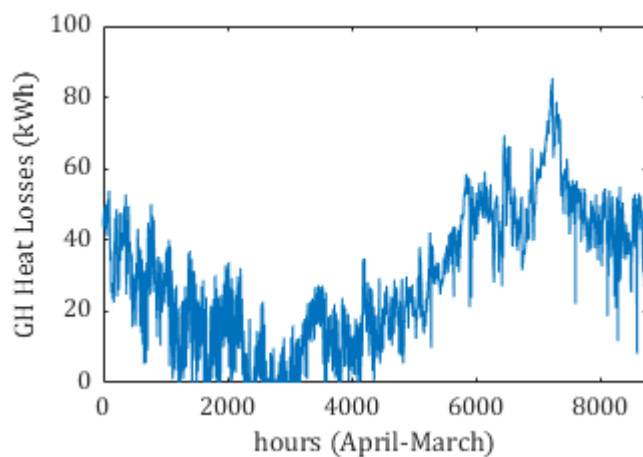


Figure 2-17 Overall heat losses of the greenhouse unit

From Figure 2-17, it can be seen that the heat losses are much larger during winter time due to temperature difference between surroundings and interior, whether during some summer

hours, the losses were very low and at times completely null (Mahmood Farzaneh-Gord et al., 2013).

Lastly, the year-wise heat losses shown a negative impact of about 255 MWh on the greenhouse.

2.1.4 Greenhouse Ventilation

Plant growth is subjected to control of air quality, i.e. CO_2 and O_2 concentrations and relative humidity (Monteith & Unsworth, 2013). Due to this fact, there is a consequent demand for air recycling from time to time (ASAE, 1998). The appropriate air renovations suggested by Von Zabeltitz, 2011 for colder regions can be assumed of up to $18 m^3/hm^2$ of ground area. For this study, it was assumed, $N_{renov} = 3h^{-1}$, so $9.25 m^3/hm^2$.

Knowing the number of renovations, by equation 0.30, the heat fluxes induced by air renovations were calculated, where subscripts *vent*, *renov*, *air* and *GH* are ventilation, renovations, air and greenhouse, respectively.

$$\dot{Q}_{vent} = \frac{N_{renov} V_{GH} \rho_{air} c_{p_{air}} (T_{GH} - T_{amb})}{3600} \quad (0.30)$$

From Figure 2-18, it is shown the heat fluxes from ventilation induced on the greenhouse. Meaning that over a year, the ventilation, even though it is necessary it accounts for a negative thermal input on the greenhouse.

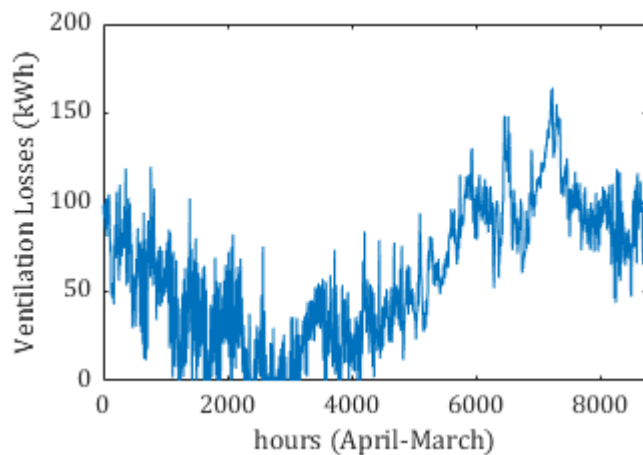


Figure 2-18 Heat fluxes induced on the greenhouse from ventilation

The negative thermal impact from ventilation reported 511 MWh of heat lost to the exterior over a year, reaching almost twice the demand from heat losses.

2.1.5 Internal Energy

In order to maintain a controlled microclimate in the greenhouse due to ventilation, heat losses and crop heat absorption, there will be certain hours in which the solar energy will not be sufficient and so an external power source is required, which is where the purpose of this study lies (Hatirli et al., 2006).

Given the parameters \dot{Q}_{loss} , \dot{Q}_{vent} and \dot{Q}_{solar} were previously determined, from equation 0.4 the remaining heat demand of the greenhouse, \dot{Q}_{green} , was obtained and plotted in Figure 2-19.

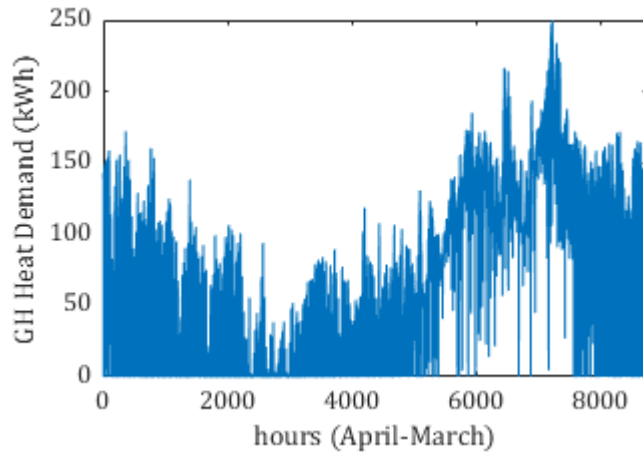


Figure 2-19 Heat demand of the greenhouse

From Figure 2-19 can be seen that the solar energy provided was not sufficient for certain times, in fact for 65.7% of the year, especially during the winter period.

After calculations, roughly 591 MWh of energy were needed to maintain the interior temperature within the set bounds. Using heat exchangers on the greenhouse, the demand of heat was set to be provided from the storage unit and when the storage could not reach total demand an auxiliary source from the district heating (DH) was introduced. For this, using equation 0.31, the heat demand was set equal to the sum of the pit's incoming fluxes, \dot{Q}_{disch} , and the auxiliary, \dot{Q}_{aux} , when required.

$$\dot{Q}_{green} = \dot{Q}_{disch} + \dot{Q}_{aux} \quad (0.31)$$

As it is normal in heat exchangers, the temperature between power source and cold fluid do not meet and so, as seen also in Figure 2-20, a pinch temperature variation was set as $\Delta T_{pinch} = 5^\circ\text{C}$, i.e. the minimum temperature difference between cold and warm flows (Smith, 2005).

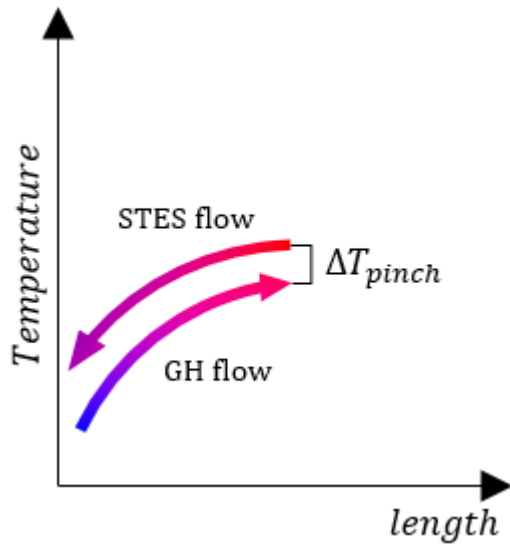


Figure 2-20 Temperature evolution on cold and hot streams on a counter-flow heat exchanger

Using the storage unit and auxiliary DH, the heat demand of the unit was coped and the temperature control was reached.

2.2 U-PIPE EVACUATED SOLAR COLLECTOR MODELLING

Using solar energy for thermal heating is a known technology with high values of usefulness with great focus in heating of buildings, like district heating (Gordon, 2013). But in fact, solar collectors also take place in industries like in combined heat and power (CHP) plants (Vliet, 2000) and many others like greenhouses, where coupled with storage units, the greenhouse's microclimate can be controlled (Mehrpooya et al., 2015; Semple et al., 2017; Taki et al., 2018).

The modelling procedure of the solar collectors was done via an energy analysis loop, dependent on the properties of the incoming flow from the seasonal heat storage, the weather conditions and the characteristics of the collector's materials. Like it is shown in Figure 2-21 the purpose of a collector is to absorb the incoming solar irradiation and transmit it to a fluid medium as form of heat, to further store given the solar irradiation's intermittency (Gordon, 2013). The subscripts *ETC*, *in* and *out* are in respect to solar collector field, incoming fluid and outlet fluid, respectively.

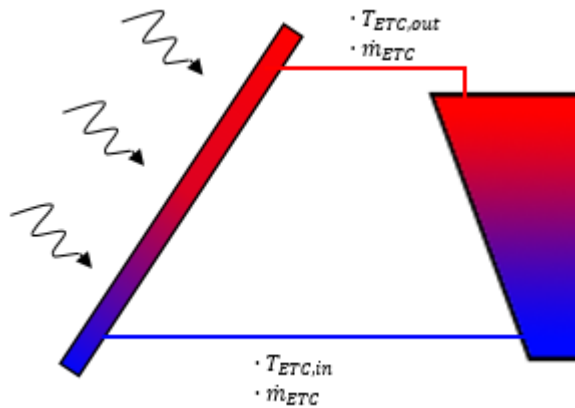


Figure 2-21 Demonstration of the ETC-PTES cycle

Given the collector’s characteristics shown in chapter 1.4, in order to facilitate the analysis, the U-tube was transformed into a single longitudinal pipe, as seen in Figure 2-22, as was suggested by Gu, Neal, & Dennis, 1998, using equation 0.32, where D_t is the real diameter of the tube, l the spacing between the tube ends and subscripts t and eq are tube and equivalent, respectively.

$$D_{teq} = \sqrt{2D_t l} \tag{0.32}$$

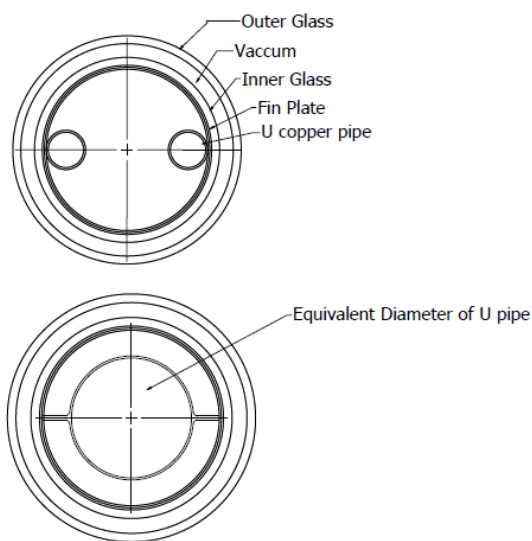


Figure 2-22 U-shaped pipe evacuated collector characteristics (top) and UpETC’s equivalent single pipe (bottom)

Throughout the whole study it was recognized the intermittency of solar irradiation, so the aim was to achieve the higher solar coverage by the collector’s field. In the other hand, due to degrading purposes of the STES film liner, the maximum ETC temperature was set as 85°C. Given this two facts, there was a realization that if the medium’s flow rate could be variant, it would be possible to achieve higher energy yields (Shafieian et al., 2019).

In order to understand the effect of the specific heat variation in respect to temperature, the minimum and maximum cp of water in a temperature interval of $[10:85]^{\circ}\text{C}$, obtained from ASHRAE, 2017, were divided and it has shown that the medium's specific heat vary less than 5% in a 55°C temperature interval. Having this into account, in the fluid's heat balance equation, shown in Figure 2-23, if it is assumed a constant inlet temperature and assuming that the variation of the specific heat is deniable, one can say that the outlet temperature and flow rate, are inversely correlated.

$$T_{f,out} = T_{f,in} + \frac{\dot{Q}}{\dot{m}cp}$$

Figure 2-23 Inverse relation between flow rate and the outlet temperature of ETC

Being $T_{f,out}$ and \dot{m} inversely dependent, then in high irradiative days that the collectors may surpass the maximum imposed medium's temperature, it should be possible to achieve almost the same energy yield by increasing the flow rate. In the case of low inlet temperature and low irradiation, if \dot{m} is low, then the outlet temperature can be increased, thus providing better temperature quality to the storage unit. Once setting the variable flow rate as transient, an iterative process of various flow rate bounds was conducted in order to achieve the higher efficiency, reaching the operating range of $\dot{m}_f \in [0.001:0.020] \text{ kg/s}$.

As demonstrated in Figure 2-24, the variation of the flow rate worked properly, where during the warmer period it was increased and decreased during the colder period thus yielding a higher percentage of absorbed solar radiation (Badar et al., 2012; Naik et al., 2016).

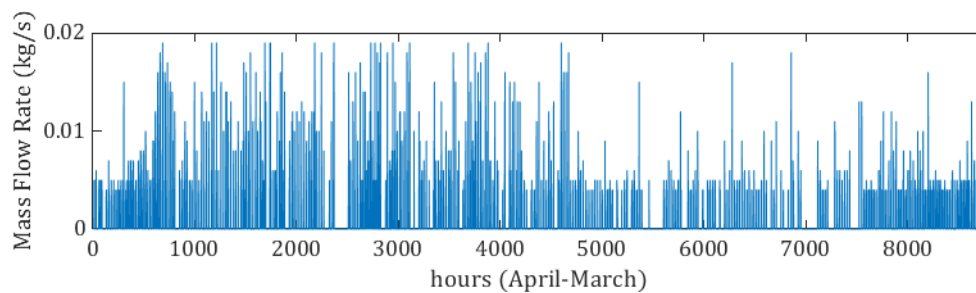


Figure 2-24 Solar collector's mass flow rate variation

2.2.1 UpETC Energy Balance

The energy analysis for the evacuated solar collectors' field was done based on equations 0.33 and 0.34, as has been done by Yan Gao, Zhang, Fan, Lin, & Yu, 2013; Li et al., 2010; Mishra, Garg, & Tiwari, 2015; Shafieian et al., 2019, where the useful solar energy captured by the collector, \dot{Q}_{ETC} , depends on the incident solar irradiation, $I(\tau_g\alpha_p)A_p$, and its losses $U_{loss}A_p(T_p - T_{amb})$. At the same time the potential created by the ETC can be calculated in two ways: in the left side of equation 0.34, by the medium's absorbed heat, dependent on the

fluid mass flow rate, \dot{m}_f , its specific heat, c_p , and difference between outlet and inlet fluid temperature, $(T_{f,out} - T_{f,in})$ and on the right side, by the transmitted heat from the absorbing fin plate to the fluid medium, dependent on the ETC efficiency factor, F' , the convection heat transfer coefficient between the plate and fluid, h_{pf} , and temperature difference between fin plate and fluid inlet, $(T_p - T_{f,in})$.

$$\dot{Q}_{ETC} = I(\tau_g \alpha_p) A_p - U_{loss} A_p (T_p - T_{amb}) \quad (0.33)$$

$$\dot{Q}_{ETC} = \dot{m}_f c_p (T_{f,out} - T_{f,in}) = F' h_{pf} (T_p - T_{f,in}) \quad (0.34)$$

The subscripts *ETC*, *g*, *p*, *loss*, *amb* and *pf* of the above equations stand for unit solar collector, glass, plate, losses, ambient and from plate to fluid, respectively.

The system of equations used to reach the energy balance in this study required an initial guess and some assumptions, as to turning it feasible mathematically and computationally. The assumptions taken are as follow:

- Maximum outlet temperature of 85°C (degradation respects to storage's film liner)
- Preventive temperature from lowest end of storage equal to ETC inlet temperature as seen in Figure 2-21.
- Constant fin-plate temperature along its length
- Mass flow rate operating range of [0.001:0.020] kg/s
- South tilted solar collectors with no shadow effect from the nearby collectors
- Equal inner and outer glass temperatures
- Negligible dirt and dust
- Negligible manifold header heat losses

Decided the constraints and assumptions, an iterative process was created in loop for every given hour to determine all required outputs as seen in Figure 2-25. The iterations were done for an i^{th} number of times until the convergence criteria was reached in respect to the variable of the fin plate's temperature, T_p . Once the convergence was achieved, another iterative process would be run for every j^{th} value of the medium's mass flow rate and finally analysing the number of j outlet temperatures, $T_{f,out}$, its maximum value would be chosen and so the optimal flow rate and consequently every other outputs would be set.

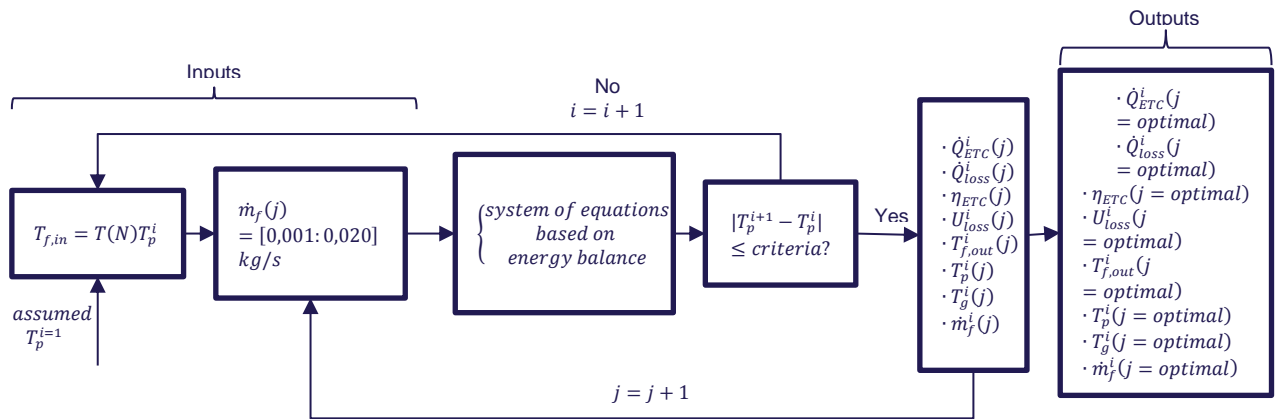


Figure 2-25 Modelling method of the solar collector field

2.2.2 Effective Irradiation

The effective solar irradiation is the parcel of available solar energy that is available to provide heat to the passing medium. It is dependent on the aperture area of the solar collector field, tilted global solar irradiation, transmissivity of the glass and absorptivity of the fin (Vliet, 2000). So, the thermal characteristics of transmitter and absorber materials will affect highly the efficiency of a solar collector (Y. Gao et al., 2014; Sabiha, Saidur, Mekhilef, & Mahian, 2015).

Similarly to the calculations of the greenhouse’s incoming radiation on each surface, the provided year-wise energy is dependent on its solar and surface angles. In this case, from the dataset, a previous study was done in respect to a series of tilted angles, β , with a surface azimuth angle, $a_w = 0^\circ$, i.e. facing south, as suggested for fixed solar collectors by Gordon, 2013; Vliet, 2000.

As seen in Figure 2-26, the sum of the solar irradiation by unit area at the given tilted angles was done and plotted and its maximum was reached at $\beta = 45^\circ$, so it was the optimal, $\beta_{optimal}$, used in the simulations of the solar collector’s field.

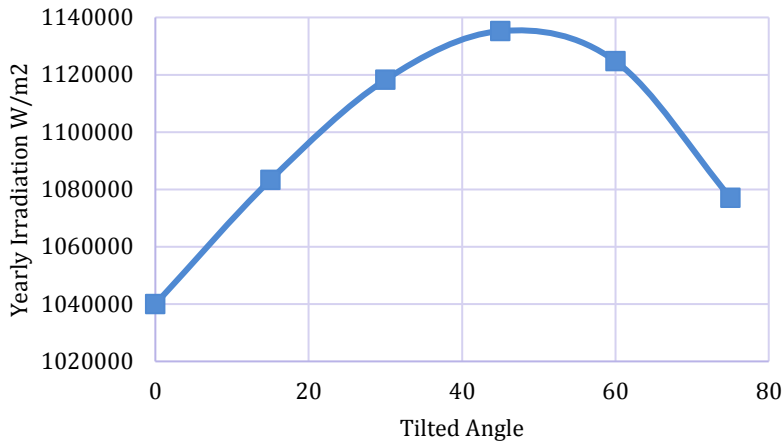


Figure 2-26 Yearly irradiation by the tilted angle, β

At every given hour it was possible to determine the effective irradiation, I_{eff} , by means of equation 0.35, where the aperture area is given by the area of half a cylinder of the fin plate which is dependent on the plate’s length, L_p , and radius, r_p . (Mishra et al., 2015)

$$I_{eff} = I (\tau_g \alpha_p) A_p, \quad \text{where } A_p = \pi r_p L_p \quad (0.35)$$

The effective irradiation per solar collector is shown in Figure 2-27, where there is a descendent trend of availability from the beginning of the charging process as it approached winter time.

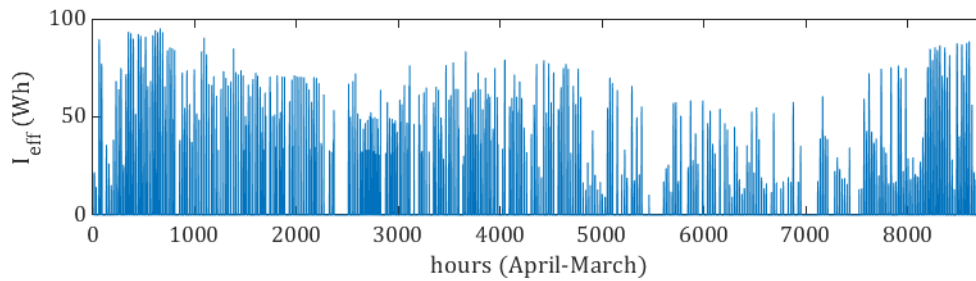


Figure 2-27 Effective solar irradiation per solar collector

In the whole year there were 1094 kWh/m^2 available from solar irradiation and a total of 129.5 kWh per collector of effective available solar irradiation.

2.2.3 Heat Losses

The norm for the determination of the heat losses of each solar collector was determined by Fourier’s law, depending on the overall heat transfer coefficient to the surroundings, U_{loss} , the aperture area, A_p and the temperature difference between the interior plate temperature, T_p , and surroundings temperature, T_{amb} , as seen in equation 0.36 (Mishra et al., 2015).

$$\dot{Q}_{loss} = U_{loss}A_p(T_p - T_{amb}), \quad \text{where } A_p = 2\pi r_p L_p \quad (0.36)$$

Given that the ambient temperature is known from data, the depending variables will be the U-value and the plate's temperature.

The process used for the calculations of the heat transfer coefficient was analogue to the one used for the greenhouse, depending on the thermal resistances present in the structure of the UpETC. For this, it was set the external thermal resistance between the ambient to the glass, R_{g-amb} , and the radiation resistance between the plate and glass, R_{p-g} , as shown in equation 0.37. Denoting that no conduction resistance was considered in the glass due to its low thermal conductivity and thickness (2mm) as done by Y. Gao et al., 2014 and no conduction or convection resistances were assumed in the bulk vacuum region, given that for low working temperatures (< 80 °C) the vacuum deterioration does not affect significantly in heat loss calculations, as was demonstrated by Y. Gao et al., 2014; Saikia et al., 2019; Trushevskii, 2007.

$$\frac{1}{U_{loss}} = R_{g-amb} + R_{p-g}, \quad \text{where } R_{g-amb} = \frac{1}{1/h_{conv,g-amb} + 1/h_{rad,g-amb}} \quad (0.37)$$

From Bergman et al., 2011, the correlation for the convection coefficient was obtained, for a case like the one shown in Figure 2-28, where it was assumed an external flow passing through a cylindrical material with constant surface temperature along its length and for any given range of Reynolds number, so the Nusselt number was set, as seen in equation 0.38.

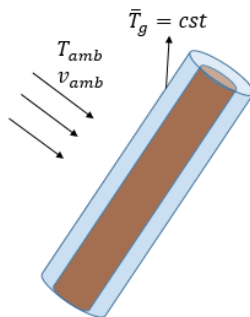


Figure 2-28 Demonstration of concentric tube attacked by the surrounding's flow at T_{amb} and v_{amb} , considering constant glass temperature, T_g , along its height

Denoting that the subscript D accounts for the length used in calculations as the glasse's diameter.

$$\overline{Nu}_D = 0.3 + \left(\frac{0.62 \sqrt{Re_D} (Pr)^{\frac{1}{3}}}{\left(1 + \left(\frac{0.4}{Pr}\right)^{\frac{2}{3}}\right)^{\frac{1}{4}}} \right) \left(1 + \left(\frac{Re_D}{282000}\right)^{\frac{5}{8}} \right)^{\frac{4}{5}}, \text{ for } \begin{cases} 0.7 \leq Pr \leq 500 \\ 1 \leq Re_D \leq 10^6 \end{cases} \quad (0.38)$$

$$\text{where, } Re_D = \frac{\rho_{air} v_{amb} D_g}{\mu_{air}}$$

Having the Nusselt number, it is then possible to determine the convection coefficient between glass and ambient, as seen in equation 0.39.

$$h_{conv,g-amb} = \frac{Nu_D k_{air}}{D_g} \quad (0.39)$$

The correlations used for the radiation thermal resistances were obtained from Bergman et al., 2011, where in the case of radiation loss from the glass to ambient was set assuming a small object in a very large cavity, as demonstrated in equation 0.40. Given the much larger area of the ambient surroundings than of the collector, it can be assumed an area ratio, A_g/A_{amb} , of zero and a view factor of 1.

$$h_{rad,g-amb} = \sigma \varepsilon_g (T_g^2 + T_{amb}^2) (T_g + T_{amb}) \quad (0.40)$$

For the radiation thermal resistance from the plate to the glass, two concentric cylinders were assumed, as seen in equation 0.41, dependent on the Stefan-Boltzmann constant, $\sigma = 5.67e-8 \text{ W/m}^2\text{K}^4$, emissivity, ε , radius, r and temperature of both glass, T_g , and plate, T_p .

$$R_{p-g} = \frac{\frac{1}{\varepsilon_p} + \frac{1 - \varepsilon_g}{\varepsilon_g} \left(\frac{r_p}{r_g}\right)}{\sigma (T_p^2 + T_g^2) (T_p + T_g)} \quad (0.41)$$

As shown in Figure 2-29, for concentric pipes, the correlation used was dependent on the equality between the ratio of both pipes' areas and radius, which was achieved, since the lengths of the tube and glass were considered equal and given that they are parallel, the view factor, F_{p-g} of one (Kumar & Rosen, 2011; Naik et al., 2016) .

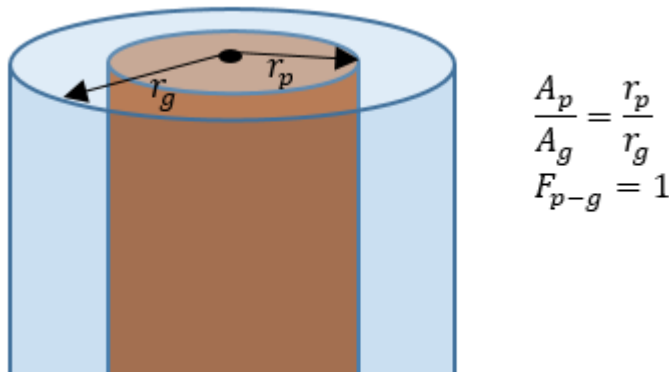


Figure 2-29 Representation of concentric pipe, view factor and relation between inner and outer pipe area and radius

The main problem with equation 0.41 is that the glass temperature is not known, so for this, correlation seen in equation 0.42, was used to estimate the glass temperature as suggested by Akhtar & Mullick, 1999; Mahboub & Moumami, 2012.

$$T_g = T_{amb} + h_{conv,g-amb}^{-0.42} \left(0.66336 \varepsilon_p - 0.6547 + \frac{T_p}{346} - 1.16 e^{-0.072(T_p - T_{amb})} \right) \quad (0.42)$$

Having the appropriate glass temperature and plate temperature, the radiation resistance was determined and thus, by equation 0.37, the overall heat transfer coefficient was set. With the U-value, plate’s temperature, ambient temperature and area of collector the energy losses were obtained by equation 0.36.

As suggested by Badar et al., 2012, in Figure 2-30 can be seen that as inner temperatures were higher and mass flow rates decreased, shown in Figure 2-24, the heat losses increased greatly.

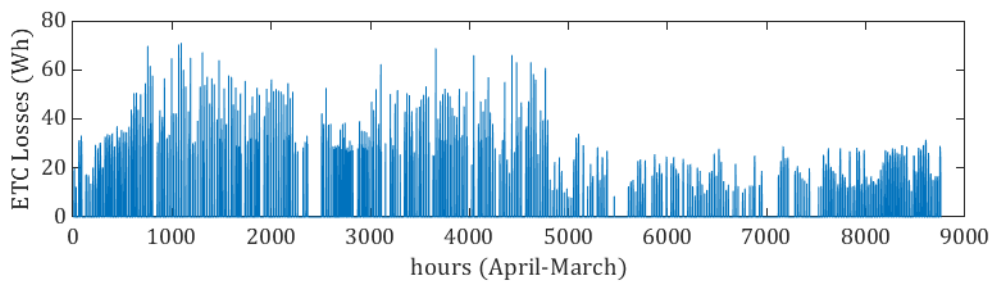


Figure 2-30 Average collector’s heat losses to ambient surroundings

In the end, each collector lost an average yearly 37.3 kWh of heat to ambient surroundings.

2.2.4 Useful Energy

In order to determine the useful energy, one can simply subtract the heat losses to the effective irradiation as demonstrated in equation 0.33, but the medium’s outlet temperature it is still unknown and another equation is required to obtain the new value of the plate’s temperature, in order to check for convergence. For this, initially, from the left side of

equation 0.34, the outlet temperature is determined as function of the inlet temperature, $T_{f,in}$, specific heat, cp , flow rate, \dot{m}_f , and useful energy, \dot{Q}_{ETC} .

Finally, from the right side of equation 0.34, the new plate temperature can be found as function of the collector's efficiency factor, F' , the tube's area, A_t , convection heat transfer from absorber fin to fluid, h_{pf} , the inlet temperature, $T_{f,in}$ and useful energy, \dot{Q}_{ETC} . The determination of the convection transfer coefficient was done based on heat balance and Newton's cooling law as seen in equation 0.43, that states that the heat flux transferred from the hot plate, at constant temperature, and the medium is equal to the heat flux between the inlet and outlet of the fluid and so the temperature variation between the transferring surface and the medium decreases exponentially along the length of the tube as shown in Figure 2-31 (Bergman et al., 2011).

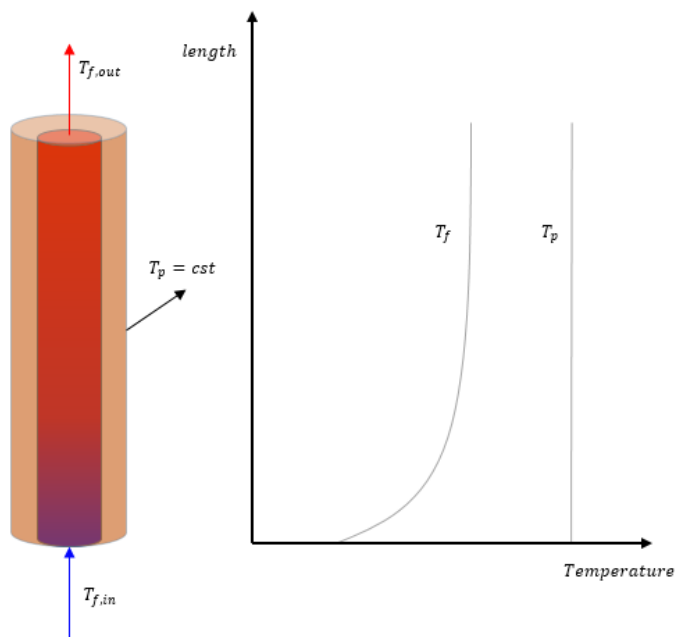


Figure 2-31 Representation of temperature evolution along a pipe with flowing cold medium

$$h_{pf} = \frac{(T_{f,out} - T_{f,in})\dot{m}_f cp}{\Delta T_{ln} A_t} \text{ where:} \quad (0.43)$$

$$A_t = 2\pi r_t L_t$$

$$\Delta T_{ln} = \frac{(T_{f,in} - T_{f,out})}{\ln\left(\frac{T_p - T_{f,out}}{T_p - T_{f,in}}\right)}$$

Having the convection heat transfer it is possible to determine the new plate's temperature and check if the convergence criteria has been met, as was determined in the modelling in Figure 2-25. Finally, the outputs are set and the modelling of the next solar collector in

series, with inlet characteristics equal to the outlet of the previous one will be done (Mishra et al., 2015).

2.2.5 Number of UpETC in series and parallel

Both temperature rise and power requirement will often dictate the necessary amount of solar collectors in series (Vliet, 2000). The way that the collectors are connected is shown in Figure 2-32, where for a number of $i \in [1:N]$ collectors, the incoming cool fluid from the STES will act as the inlet of the first collector and its outlet temperature equal to the inlet temperature of the second one, assuming no heat losses in the connections (Zelzouli et al., 2012). This process will be done until the N^{th} collector in series, where its outlet temperature will be the one injected into the pit.

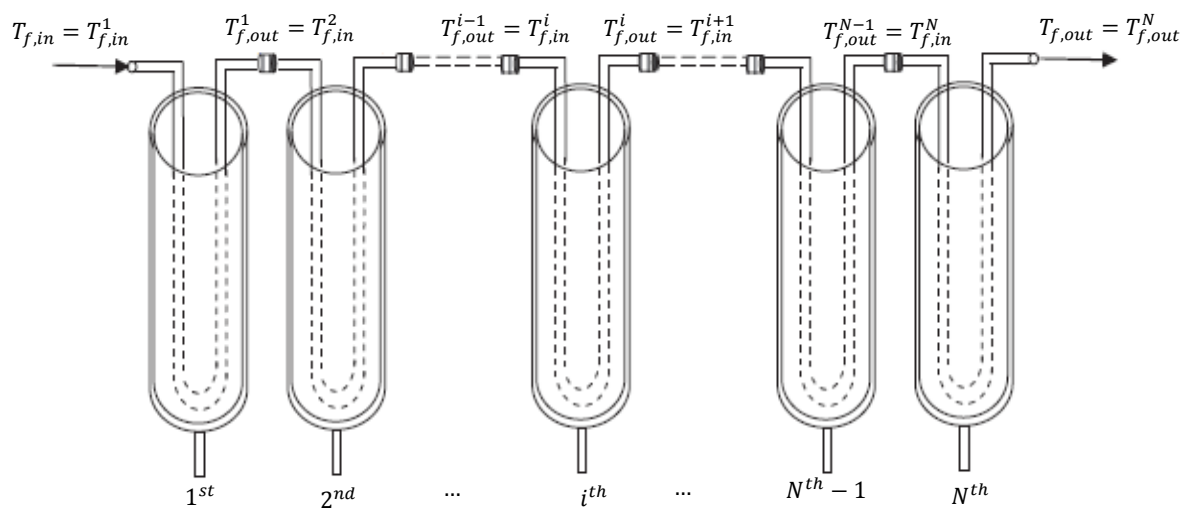


Figure 2-32 Array of UpETC connected with N number of series

As demonstrated in the end of section 0, an analysis was conducted to understand the best thermal and economical behaviour, reaching the conclusion that the system worked best with $N = 20$ collectors in series.

The relation between series and parallel is demonstrated in Figure 2-33, where an incoming flow at initial temperature, $T_{f,in}$, and flow rate, \dot{m}_{ETC} , is divided into the $N_{parallel}$ number of groups of series with flow rate of \dot{m}_f and reaching the end of each series with an outlet temperature of $T_{f,out}$. The groups of series will finally connect with a temperature of $T_{f,out}$ and mass flow rate equal to the sum of the flow rates of each series (Jamshidian et al., 2018).

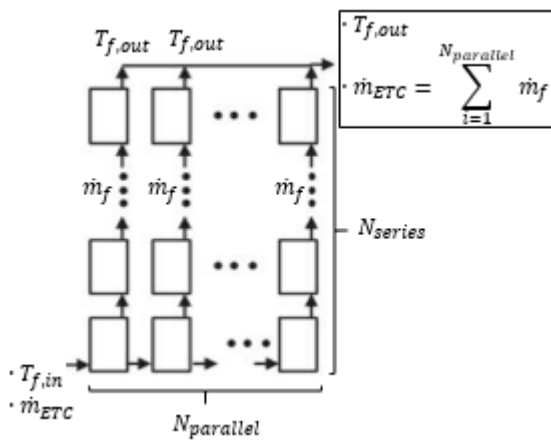


Figure 2-33 Representation of a collector field with N number of collectors in series and N number of groups of series in parallel and their relations with temperature and mass flow rate

The number of parallel groups of series can be set by the ratio between the total aperture area and the product of the aperture area of a single collector and the number of collectors in series as shown in equation 0.44.

$$N_{parallel} = \frac{A_{ETC}}{A_p N_{series}}, \text{ where } N_{series} = 20 \text{ and } A_p = \pi r_p L_p \tag{0.44}$$

The configuration of the UpETC field had a total aperture area of collection of 3000 m², with 1128 parallel groups of 20 single collectors in series.

2.2.6 ETC Efficiency

Having set all parameters and thermodynamic relations for the loop shown in Figure 2-25, the system of equations was generated for all hours under the set constraints and conditions and finally the desired outputs were procured. The outputs with higher importance were the overall useful energy, \dot{Q}_{ETC} , mass flow rate, \dot{m}_{ETC} and outlet temperature, $T_{f,out}$, since they are the charging inputs on the STES unit (Mishra et al., 2015).

The overall useful energy was calculated simply considering each group of series as a thermal resistance, where the potential created between in and out fluxes would provide the generated energy as is shown in equation 0.45. Summing all $N_{parallel}$ groups of collectors in series, the overall ETC useful energy was obtained.

$$\dot{Q}_{ETC} = \sum_{i=1}^{N_{parallel}} \dot{m}_f cp (T_{f,out}^N - T_{f,in}^1) \tag{0.45}$$

The efficiency of the solar collector field, can be calculated as the ratio of the useful energy by the available solar irradiation on the total aperture area, as it is shown in equation 0.46.

$$\eta_{ETC} = \frac{\dot{Q}_{ETC}}{IA_{ETC}} \quad (0.46)$$

In Figure 2-34 is shown the daily efficiency of the collector field, where the efficiencies were greater during the charging periods of the year, given the lower temperature variations and higher flow rates.

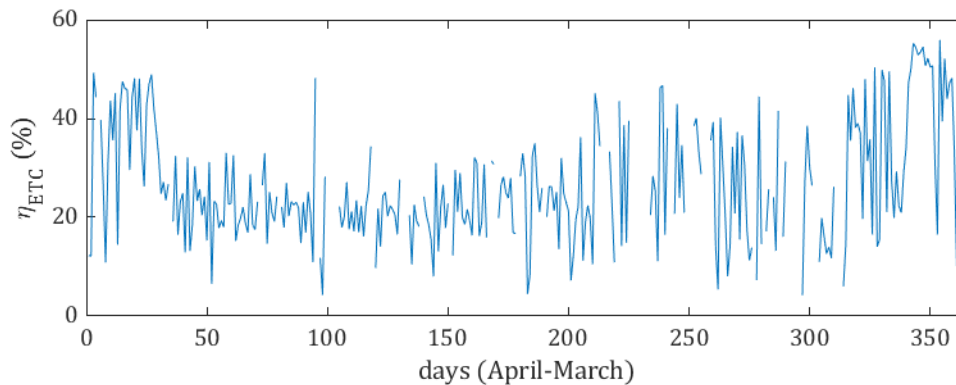


Figure 2-34 Daily efficiency of the collector field

Finally, the system managed to harvest 541.7 MWh of heat out of the available 1618 MWh of solar irradiation, thus yielding an efficiency of 33.5% and having 841.9 MWh of heat losses to the surroundings.

2.3 PIT SEASONAL THERMAL ENERGY STORAGE

As previously explained in section 1.3, the seasonal storage unit used was a pit storage, which consists of a drilled hole in the ground with the shape of a truncated pyramid turned upside down, with a polypropylene film separating the fluid from the surrounding soil, an insulation on the top cover, separating the fluid from the ambient conditions, and with inlet and outlet pipes to/from the charge and discharge units, i.e. ETC field and greenhouse, respectively, as can be seen in Figure 2-35 (Böszörményi & Šiváková, 2012; Fan et al., 2017; IEA, 2011; John A. Duffie, 2013; PlanEnergi, 2013, 2015).

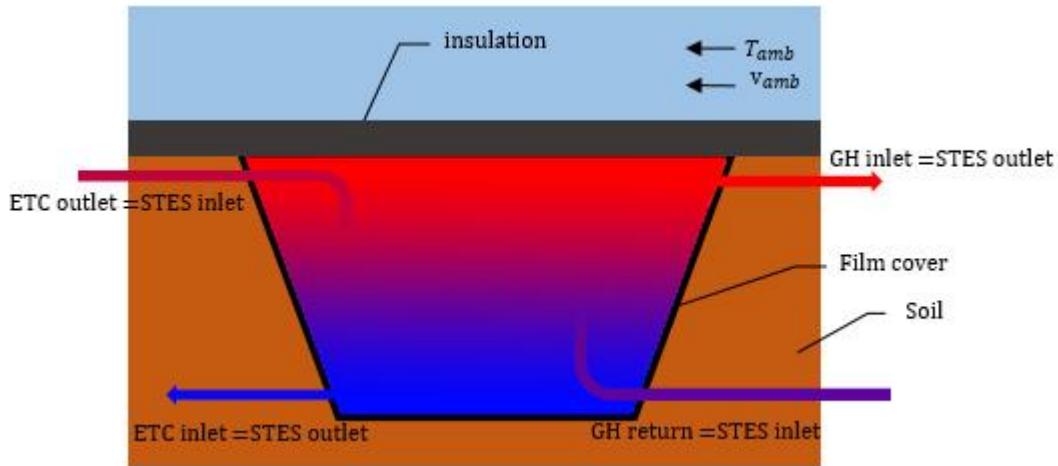


Figure 2-35 Representation of pit storage facility with inlet and outlet streams and surroundings

As seen in Figure 2-35, one of the main aspects was to promote stratification given that no mechanic stratifiers were used, so it was extremely important the proper fitting of each inlet and outlet. For this, the outgoing fluid to the ETC field was set to come from the bottom of the storage, i.e. the colder region, and the charged fluid from the ETC would enter the pit on the top of the unit and follow its path to zone with similar temperature/density. Inversely, the charged GH flow was set to come from the top most charged zone of the pit, ensuring higher quality of provided heat, and the GH return would enter the pit from the bottom and fade in the region with similar temperature/density (Lavan & Thompson, 1977; Soomro, Mokhtar, Akbar, & Abbasi, 2018).

Simulating stratification has been done widely in literature and two main models are commonly used: multi-node and plug flow (Cadau et al., 2019; John A. Duffie, 2013; Soomro et al., 2018). For this study, the multi-node was the strategy used, where a series of $i \in [1:N]$ number of nodes were determined with equal distance, Δx , from themselves vertically wise, as seen in Figure 2-36, hence dividing the pit's volume into N number of sub-volumes. The multi-node model has the goal of discretizing a volume and conduct a system of equations on every discretized region, aiming to get the thermal relation that every i^{th} node has with its neighbour nodes, i.e. with $i^{th} - 1$ and $i^{th} + 1$, alongside with surroundings and passing flows as function of temperature. Given this, an energy balance was created for every i^{th} node (John A. Duffie, 2013; Zelzouli et al., 2012).

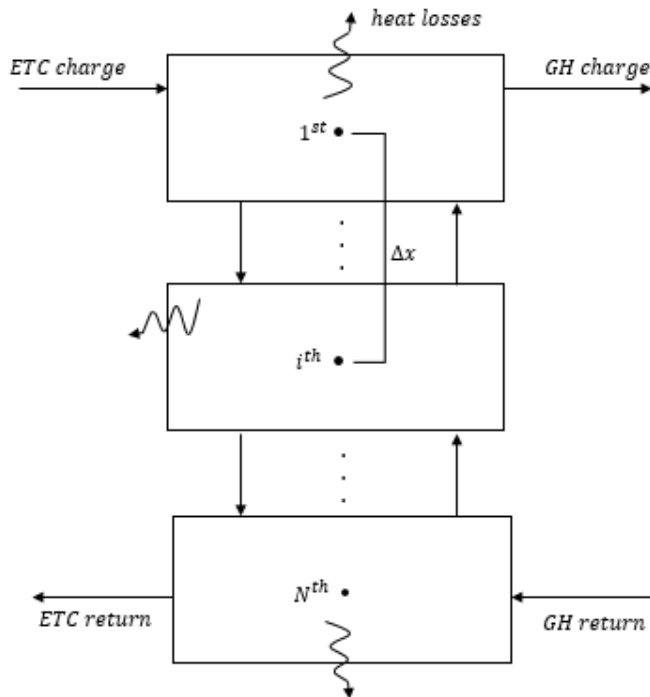


Figure 2-36 Configuration of a tank with N number of nodes

Exactly like the GH and ETC modelling, the PTES simulations were done for every given hour based on heat balance equations, depending on ambient thermal interactions and thermal conditions of incoming and outgoing flows to collector field and greenhouse unit.

2.3.1 Pit thermal energy storage heat balance

Conducting a heat balance for PTES is complex given the multiple number of inlets and outlets at different conditions and interactions with neighbouring nodes and surroundings (Böszörményi & Šiváková, 2012). So, based on the first law of thermodynamics, shown in equation 0.47, some assumptions were taken, to simplify and decrease computational costs.

In equation 0.47, it is stated that the internal energy's changes in respect to time, $\frac{dE}{dt}$, are dependent on the net heat transfer with surroundings, \dot{Q} , the net work done in the system, \dot{W} and mass transfers that may occur into and out of the system. The variables \dot{m} , h , v , g and z stand for mass flow rate, enthalpy, velocity, acceleration of gravity and height, respectively (Dincer & Ezan, 2018; John A. Duffie, 2013).

$$\frac{dE}{dt} = \dot{Q} + \dot{W} + \sum_{in} \dot{m}_{in} \left(h + \frac{v^2}{2} + gz \right)_{in} - \sum_{out} \dot{m}_{out} \left(h + \frac{v^2}{2} + gz \right)_{out} \quad (0.47)$$

In this project, no mechanical work was considered in the pit, the effects from kinetic and potential energy were neglected due to low variations and every incoming flow stream had an analogue outlet with same flow rate, thus in and out mass transfers could be combined into a single term (Dincer & Ezan, 2018; John A. Duffie, 2013). Done these assumptions, the energy balance can be simplified as seen in equation 0.48.

$$\frac{dE}{dt} = \dot{Q} + \sum \dot{m}(h_{in} - h_{out}) \quad (0.48)$$

As stated by Cadau et al., 2019; John A. Duffie, 2013; Soomro et al., 2018, predicting the proper stratification level when using multi-node approach is highly dependent on the number of nodes or divisions assumed, where they demonstrate that the bigger number of nodes, the better prediction of fluid interaction in the tank, thus higher quality of output values. On the other hand, the number of nodes come at great computation expenses given the complexity of STES modelling, so a good comprise should be taken to ensure appropriate thermocline prediction and duration of simulations. In this study 32 nodes were considered in order to have a distance between nodes of less than half a meter from each other, comprising the recommendations of Cadau et al., 2019; John A. Duffie, 2013 of at least 10 nodes to ensure a feasible thermocline prediction.

From equation 0.48, the actual variables of the project at hand were introduced, where the internal energy variation for every i^{th} node is given by the product of its volume, V , density, ρ , specific heat, c_p and the temperature variation between the j^{th} hour and $j^{th} + 1$, $dT = (T^{j+1} - T^j)$. The internal energy is then affected by the several changes in the system as stated in equation 0.49, where \dot{Q}_{loss} , \dot{Q}_{ETC} , \dot{Q}_{GH} and \dot{Q}_{mix} are the heat losses to surroundings, net heat provided by the ETC field, power discharged to the greenhouse unit and the node-to-node heat gains/losses depending on the loads induced by the GH and ETC flows (Arabkoohsar, 2016).

$$\rho V c_p \frac{dT}{dt} = \dot{Q}_{ETC} - \dot{Q}_{GH} - \dot{Q}_{loss} + \dot{Q}_{mix} \quad (0.49)$$

2.3.2 Sub-volumes, areas and nodes

The dimensions of a pit are quite irregular given its truncated pyramidal shape and since throughout simulations a series of areas and volumes are required, this section focus solely on the math behind all dimensions used in the next chapters.

The volume of a truncated pyramid is given by equation 0.50, being dependent on the upper area, A_{top} , the bottom area, A_{bottom} and on the height of the pit, h , as can also be seen in Figure 2-37 (Gillings, 2020).

$$V_{PTES} = \frac{1}{3}h \left(A_{top} + A_{bottom} + \sqrt{A_{top}A_{bottom}} \right) \text{ where} \tag{0.50}$$

$$A_{top} = WL \text{ and } A_{bottom} = wl$$

The walls' areas are also important to know considering the thermal interaction with the soil. So two area groups were considered given the different dimensions: north and south areas, A_{NS} , and east and west areas, A_{EW} , as is demonstrated in Figure 2-37 and given by equation 0.51.

In equation 0.51, W , L , w and l are the width and length of the top area and width and length of bottom area, respectively.

$$A_{NS} = \frac{W + w}{2} h$$

$$A_{EW} = \frac{L + l}{2} h \tag{0.51}$$

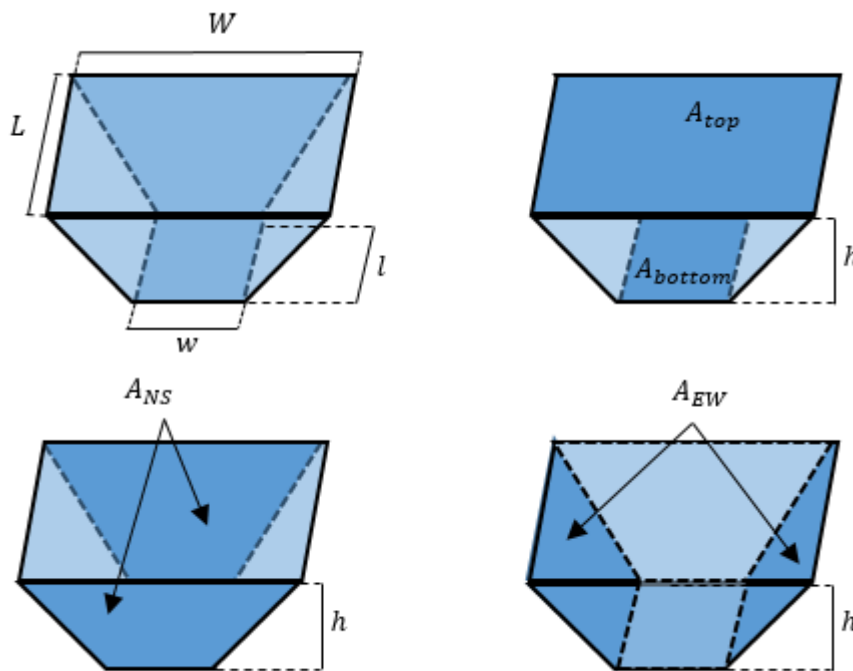


Figure 2-37 Representation of surfaces and dimensions used in the modelling of the pit storage

As the calculations were done for every given sub-volume, the same equations for volume and areas adapt for every i^{th} region. As demonstrated in Figure 2-38 if the angle α is determined, every given distance for every region can be obtained, thus using equations 0.52 and 0.53 the lengths and widths for every divisions were obtained.

$$\alpha_{NS} = \tan^{-1} \frac{(W - w)}{2} / h$$

$$\alpha_{EW} = \tan^{-1} \frac{(L - l)}{2} / h$$
(0.52)

$$w^i = W - 2h^i \tan \alpha_{NS}$$

$$l^i = L - 2h^i \tan \alpha_{EW}$$
(0.53)

where $i \in [i: N + 1]$ and $h^i = h^i - 0.5$ with $h^1 = h$

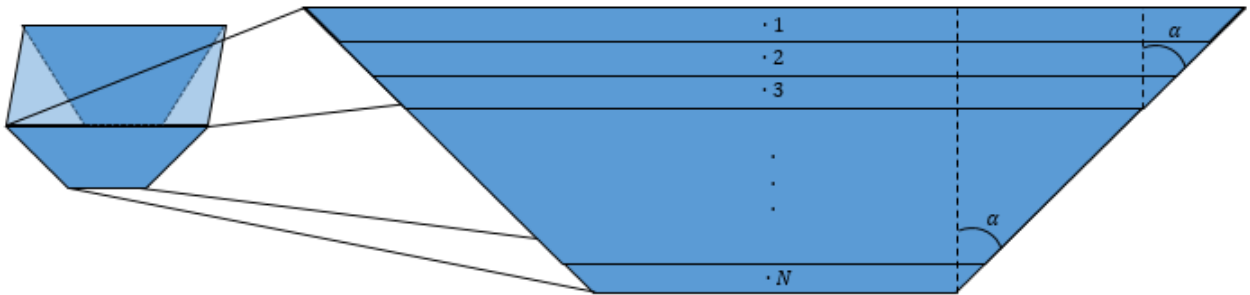


Figure 2-38 Representation of sub-volume's divisions

2.3.3 Storage heat losses to surroundings

The heat loss criteria used in the STES unit were similar to the GH ones, shown in chapter 2.1.3, since there is equally one working fluid separated from a bulk region at distinct thermal conditions. Given this, two separating regions were considered: fluid-to-air and fluid-to-soil, as shown in Figure 2-39, relying on soil and ambient conditions.

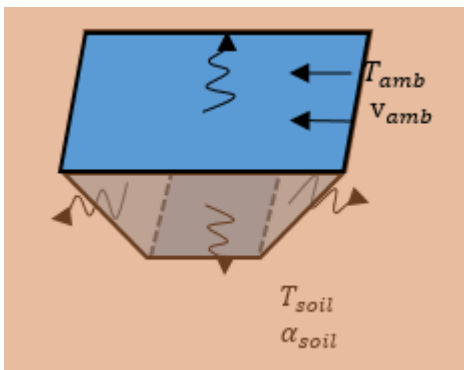


Figure 2-39 Surroundings regions and characteristic considered to generate the heat losses of the seasonal heat storage

The general heat balance between interior and surroundings is shown in equations 0.54, 0.55, 0.56 and 0.57, as node dependent. For the walls' heat losses, given the different areas for north-south and east-west, both were considered and overall heat losses were calculated dependent not only on nodes but also on orientation.

The subscripts, from following equations, *loss*, *wall*, *top*, *bottom*, *i*, *NS*, *EW*, *soil* and *amb* are overall losses, from walls, top and bottom, i^{th} node from 1 to 32, north-south walls, east-west walls, soil/ground dependent on depth and ambient, respectively.

$$\dot{Q}_{loss}^i = \dot{Q}_{wall}^i + \dot{Q}_{top}^i + \dot{Q}_{bottom}^i, \quad \text{where } \begin{cases} \dot{Q}_{bottom} = 0 \text{ if } i \neq N \\ \dot{Q}_{top} = 0 \text{ if } i \neq 1 \end{cases} \quad (0.54)$$

$$\dot{Q}_{wall}^i = (U_{NS}^i 2A_{NS}^i + U_{EW}^i 2A_{EW}^i)(T^i - T_{soil}^i) \quad (0.55)$$

$$\dot{Q}_{bottom}^i = U_{bottom}^i A_{bottom}^i (T^i - T_{soil}^i) \quad (0.56)$$

$$\dot{Q}_{top}^i = U_{top}^i A_{top}^i (T^i - T_{amb}) \quad (0.57)$$

The moving fluid inside kept on changing direction (on Y axis) and intensity, given the variability of the collectors' flow rate and intermittent necessity of GH's loads as will be shown in Figure 2-46 in chapter 2.3.6. Given this and the wide area of the passing fluid, the Reynolds and Grashoff numbers were determined by means of equations 0.21 and 0.23, respectively. A relation between these two, shown in equation 0.58, sets the predominant effects between buoyant and inertial forces, thus it is possible to assume the flow's behaviour as free or forced convection and with it, the variables from which the Nusselt number is dependent on will be defined (Bergman et al., 2011).

$$Nu = \begin{cases} f(Re, Pr) & \text{if } Gr/Re^2 \ll 1 \\ f(Gr, Pr) & \text{if } Gr/Re^2 \gg 1 \end{cases} \quad (0.58)$$

With the Grashoff-squared-Reynolds ratio done, the minimum value for each location was determined and shown in Table 2-8. Since all locations demonstrated much larger values than unity, it was possible to assume that even though there is a flow regime in the pit, the buoyant forces have much higher impact than inertial ones, hence free convection was assumed for any given hour at any given node (Bergman et al., 2011; Jiji, 2006).

Table 2-8 Relation between the Grashoff number and the squared of the Reynolds number for each area

Location	N – S	E – W	Top	Bottom
<i>min</i>(Gr/Re²)	334	427	21970	17796

As suggested by (Bergman et al., 2011; R. Tian, Dai, Wang, & Shi, 2018), the Prandtl number for water was obtained by equation 0.59, as function of the fluid's dynamic viscosity, μ , specific heat, cp , and thermal conductivity, k .

$$Pr = \frac{\mu \cdot cp}{k} \quad (0.59)$$

From equations 0.55, 0.56 and 0.57, areas and temperatures were already set, so the missing parameters were the overall heat transfer coefficients and exactly like in chapter 2.1.3, they were set as the sum of all intervenient thermal resistances. Some of the thermal resistances depend on the polymer's surface temperature that was not previously determined, so an iterative process, with k as iterative counter, was conducted with initial assumption of the surface temperature of each i^{th} surface on the north-south and east-west sides, top and bottom surfaces as seen in Figure 2-40.

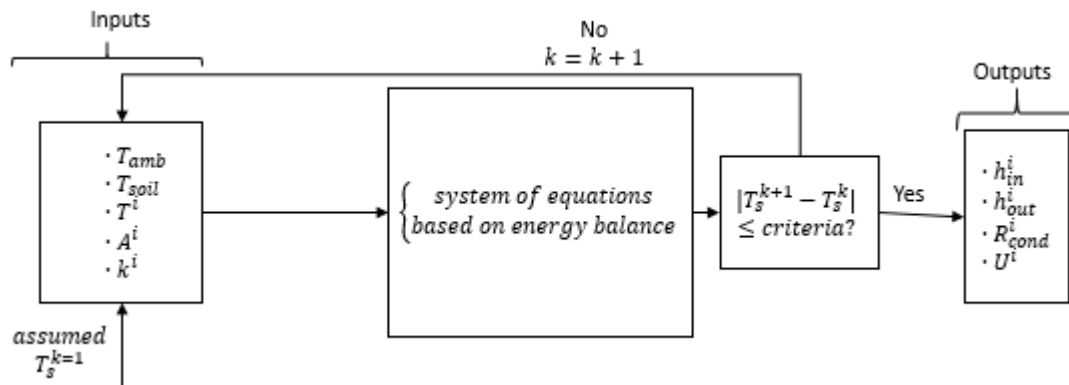


Figure 2-40 Modelling configuration to determine the thermal resistances and overall heat transfer coefficient

In the case of the top cover, a polymer insulation was input separating the medium from the ambient, so convection and conduction between the top node and the insulating material was set as seen in equation 0.60. For walls and bottom, given the quite small thickness of the separating film from the water and soil, only inner convection and external conduction were considered, seen in equations 0.61 and 0.62. From equations 0.60, 0.61 and 0.62, the subscripts *top*, *insu – amb*, *med – insu*, *insu* and *bottom* are top cover, between ambient and insulation and ambient and surroundings, between medium at top node and insulation, insulation and lower surface of pit, respectively.

$$\frac{1}{U_{top}} = \frac{1}{h_{insu-amb}} + \frac{x_{insu}}{k_{insu}} + \frac{1}{h_{med-insu}} \quad (0.60)$$

$$\frac{1}{U^i} = \frac{1}{h^i} + \frac{x_{soil}^i}{k_{soil}} \quad (0.61)$$

$$\frac{1}{U_{bottom}} = \frac{1}{h_{bottom}} + \frac{x_{soil,bottom}}{k_{soil,bottom}} \quad (0.62)$$

From PlanEnergi, 2015; Thomas Schmidt et al., 2018, it was shown that a commonly used insulation in pit thermal storage units in Denmark is the NOMALEN polymer, which is a layered polyethylene agglomerate. This material was the one considered for the simulations and it is generally sold with a thickness, x_{insu} , of 10 cm and thermal conductivity, k_{insu} , of

0.04 W/mK , so the conduction thermal resistance on the top of the unit can be obtained as shown in equation 0.60.

Similarly to the convection heat transfer between ambient and the outer layers of the greenhouse in chapter 2.1.3, the same correlations for external flows passing a horizontal flat plate were used to obtain the Nusselt number, dependent on the wind's flow laminar/turbulent behaviour passing the insulation's outer surface, as seen in equation 0.22. Thus $\overline{Nu}_{insu-amb}$ and consequently $h_{insu-amb}$ were determined (Bergman et al., 2011).

Assuming the inner surface of the insulation as a top cold surface with hot flow passing as shown in Figure 2-41(a), the correlation in equation 0.63 was determined as function of Rayleigh number. The Rayleigh number it is simply obtained as the product of the Grashoff and Prandtl numbers (Bergman et al., 2011).

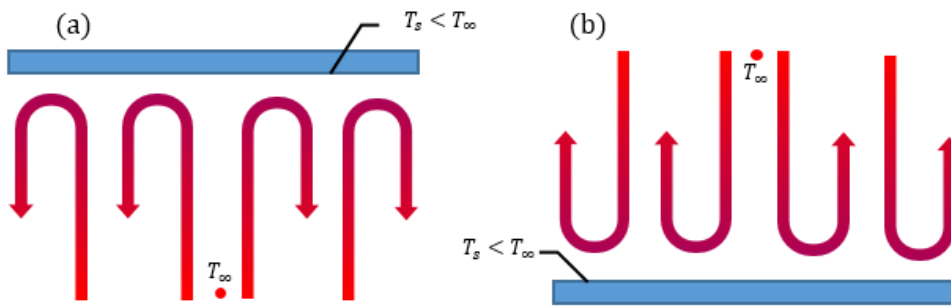


Figure 2-41 Representation of down hot flow on a top cold surface (a) and upper hot flow on a bottom cold surface

$$\overline{Nu}_{med-insu} = 0.15Ra_{top}^{1/3}, \quad \text{where } Ra = GrPr \quad (0.63)$$

With the $\overline{Nu}_{med-insu}$ calculated, the inner convection heat transfer, $h_{med-insu}$, was set by equation 0.20. Having all the thermal resistances respectant to the top cover, the overall heat transfer coefficient, U_{top} was determined.

Inversely to the top wall, the inner convection coefficient from the medium to the bottom surface was set assuming a hot flow passing through the top surface of a cold plate, as shown in Figure 2-41(b). For this, the Nusselt number was given by the correlation seen in equation 0.64 (Bergman et al., 2011; Jiji, 2006).

$$\overline{Nu}_{bottom} = 0.52Ra_{bottom}^{1/5} \quad (0.64)$$

For the soil's heat transfer by conduction, so much for walls or bottom, exactly the same transient approach was taken from chapter 2.1.3, so from equation 0.28, the soil's distance from the surface to the nearest point at constant T_{soil} was set, bearing that the soil's temperature was depended on depth as was demonstrated in Figure 2-5. Once determining the x_{soil} , for every i^{th} node and bottom, the conduction thermal resistance was calculated.

Lastly, the inner convection coefficient, h_{wall} , was determined assuming free convection on an inclined plate with \overline{Nu}_{wall} set by equation 0.65 (Bergman et al., 2011).

$$\overline{Nu}_{wall} = \left\{ 0.825 + \frac{0.387Ra^{\frac{1}{6}}}{\left[1 + \left(\frac{0.492}{Pr} \right)^{\frac{9}{16}} \right]^{\frac{8}{27}}} \right\}^2 \quad (0.65)$$

Having both \overline{Nu}_{bottom} and \overline{Nu}_{wall} the convection heat transfers h_{bottom} and h_{wall} were obtained by equation 0.20 and along with the conduction term, the overall heat transfer coefficients U_{bottom} and U_{wall} were calculated.

Finally, by equations 0.54, 0.55, 0.56 and 0.57, all net heat fluxes to the surroundings were obtained in respect to each orientation and node at every given hour.

In Figure 2-42, it was plotted the overall heat losses of the storage unit, where it can be seen the were much higher losses during the charging period, which could be due to increase in temperature variation between pit and surroundings.

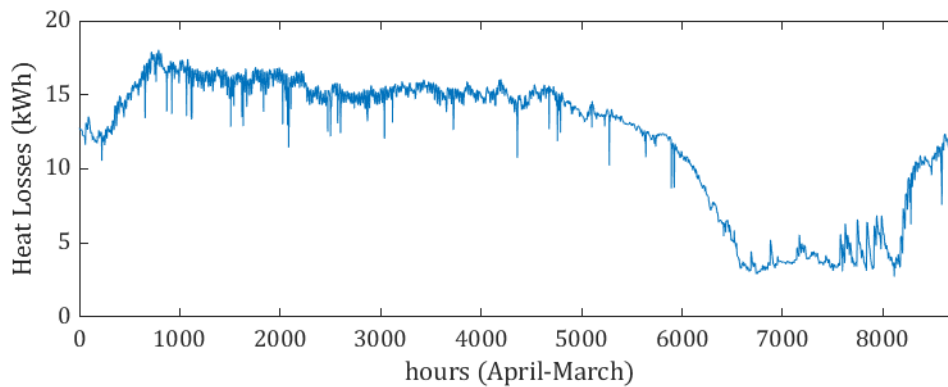


Figure 2-42 Heat losses to surroundings of the pit

Lastly, it was accounted an overall year-round 105,7 MWh of heat lost to neighbouring areas, with the highest impact coming from the top cover given the higher weather variabilities, as suggested by Ochs et al., 2020.

2.3.4 Charge into the pit

The purpose of the charging mechanism was to ensure stratification in the pit, so the temperature of the charged incoming flow from the UpETC field should be analysed to lead it into the appropriate node (Başçetinçelik et al., 1999). In Figure 2-43 is shown a charged flow coming at conditions $(\dot{m}_{ETC}, T_{f,out})$ and N possibilities that it may follow, so to properly conduce the incoming charged fluxes, a dummy variable/ charge coefficient, F_c was added to every i^{th} routes (Andersen et al., 2007; Arabkoohsar, 2016; Zelzouli et al., 2012).

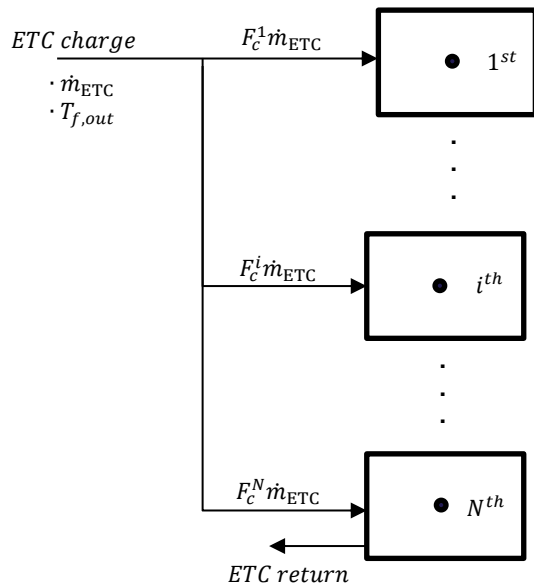


Figure 2-43 Charged flow's streams under the conditions of the charge coefficient, F_c^i

The heat balance for the charging process was conducted, admitting no mix with the previous nodes from which the flow would be set, i.e. if the charged medium would fit in the 3rd node's region, no thermal interactions would be considered with the adjacent 1st and 2nd ones as will be explained in section 2.3.6. So, once more, by the first law of thermodynamics, the charge heat flux, \dot{Q}_{charg} , was determined by the product of the charge coefficient, F_c , incoming flow rate, \dot{m}_{ETC} , specific heat, cp , and the temperature difference between the outlet ETC field, $T_{f,out}$ and specific node, T^i . The heat balance equation and conditions to set the route dependent on F_c are shown in equation 0.66 (Arabkoohsar, 2016; Mahmood Farzaneh-Gord et al., 2013; John A. Duffie, 2013).

$$\dot{Q}_{charg}^i = F_c^i \dot{m}_{ETC} cp (T_{f,out} - T^i), \quad \text{where } F_c = \begin{cases} 1 & \text{if } i = 1 \text{ and } T_{f,out} > T^1 \\ 1 & \text{if } 1 < i \leq N \text{ and } T^{i-1} > T_{f,out} > T^i \\ 0 & \text{else} \end{cases} \quad (0.66)$$

The factor F_c was set regarding the conditions shown in equation 0.66, where if the inlet flow' temperature is higher than the first node's temperature, then that will be the node to mix with. Otherwise, for any other i^{th} nodes that the temperature from the ETC field would be higher than that node and lower than the adjacent one, that will be the i^{th} sub-volume to mix with. Any other possible conditions, like having a temperature lower than the bottom node's temperature, there would be no incoming flow to the storage, given that it would discharge it (Cadau et al., 2019; John A. Duffie, 2013).

2.3.5 Discharge of the pit

As stated in chapter 1.3, the greenhouse energy load was set to always flow from the top region of the PTES and the return to the bottom, but in this case following the node at which the temperature would fit best (M. Farzaneh-Gord, Arabkoohsar, Deymi Dasht-bayaz, & Farzaneh-Kord, 2012; Soomro et al., 2018). Exactly like it was done for the charge of the storage, it was introduced a dummy variable, F_L , to control the path of the return flow.

As seen in Figure 2-44, after the heat is exchanged, a return flow enters the bottom of the pit at conditions $(\dot{m}_{GH}, T_{return})$ and dependent on the temperature of the return and on the temperature of each node, it will follow to the i^{th} discretized region.

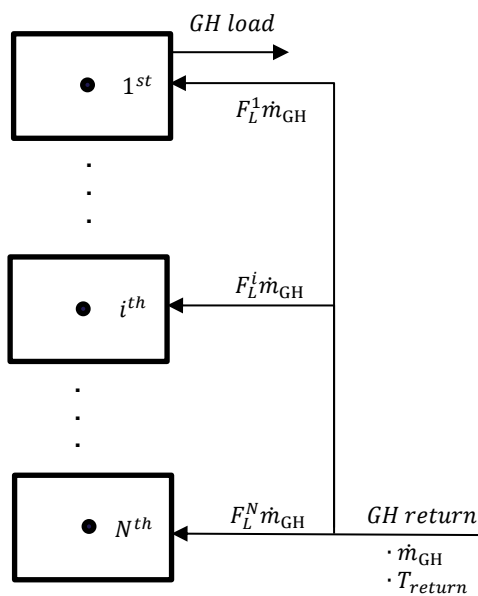


Figure 2-44 Greenhouse return flow's streams under the conditions of the return coefficient, F_L^i

The heat balance, similarly to the pit's charge, was set as in equation 0.67, where subscripts *disch*, *GH*, *L* and *return* are the discharge of the pit, greenhouse, load and return from greenhouse, respectively. The load coefficient, F_L , was set as: if the bottom node's temperature, T^N , would be higher than the return, then the discharged flow from the greenhouse would mix with the bottom node; if the return temperature would be higher than any i^{th} node, T^i , and lower than the adjacent one, T^{i-1} , then region i would be the one to diffuse with. (M. Farzaneh-Gord et al., 2012)

$$\dot{Q}_{disch}^i = F_L^i \dot{m}_{GH} cp (T^i - T_{return}) \text{ where } F_L = \begin{cases} 1 & \text{if } i = N \text{ and } T_{return} < T^N \\ 1 & \text{if } T^{i-1} \geq T_{return} > T^i \\ 0 & \text{else} \end{cases} \quad (0.67)$$

In order to determine the flow rate of the load to the greenhouse, a condition was set to ensure the flow rate wouldn't surpass the maximum value established. For this, it was

assumed that the STES would be able to provide 70% of the more critical hour of demand and the remaining would have to be provided by the external heat source, here considered from the district heating.

The hour with bigger heat requirement accounted for 36 kWh, so with the aid of equation 0.67, the flow rate was put in evidence and obtained with a 70% of the total heat load and assumed a temperature difference between source and return of 20°C. With this assumption, the maximum flow rate was set as 5 kg/s and with it, the condition to determine the discharged heat from the pit was established by equation 0.68, as either the total GH demand or if $\dot{m}_{GH} > \dot{m}_{GH,max}$, then the discharged flow would be set with mass flow rate $\dot{m}_{GH,max}$.

$$\dot{Q}_{disch} = \begin{cases} \dot{Q}_{GH}, & \text{if } \dot{m}_{GH} \leq \dot{m}_{GH,max} \\ \dot{m}_{GH,max} cp(T^1 - T_{return}), & \text{if } \dot{m}_{GH} > \dot{m}_{GH,max} \end{cases} \quad (0.68)$$

Finally, to assure the heat demand, the auxiliary heat flux was determined as the difference between the greenhouse demand and the discharge availability, as seen in equation 0.69.

$$\dot{Q}_{aux} = \dot{Q}_{GH} - \dot{Q}_{disch} \quad (0.69)$$

Given the conditions, the heat provided from the pit accounted for a total of 65.9% of the heat demand from the greenhouse.

2.3.6 **Mixing flows**

In the previous chapters 2.3.4 and 2.3.5, the charge and discharge flows were set to enter and exit in the top and bottom or in the bottom and top, respectively. Due to this and in order to ensure heat balance throughout the storage unit, this fluxes must be accounted from node 1 to N and so it will induce mixing of flows from every i^{th} node with its neighbouring ones, positively or negatively, dependent on the magnitudes of the greenhouse and ETC flows (Andersen et al., 2007; Fan, Furbo, & Yue, 2015; M. Farzaneh-Gord et al., 2012).

The mixing rule, as shown in Figure 2-45, will be dependent on the initial node where the incoming fluid will sit and afterwards following its path to its exit. So for example, if the greenhouse return would mix in the N^{th} region, then a flow would have to pass through every N^{th-i} nodes until reaching node one, fulfilling the flow that was removed to charge the greenhouse (John A. Duffie, 2013). In order to control where the flow would pass through, a mixing flow rate, \dot{m}_{mix} , was established, being dependent on the net fluxes from the GH and ETC.

The greenhouse flow's effect on \dot{m}_{mix} were established for every node, being dependent on the sum of all load coefficients of the nodes below a specific node i , where for the charge by being dependent on the sum of all charge coefficients of the above regions, as can be seen in equation 0.70 (O. Paksoy, 2005).

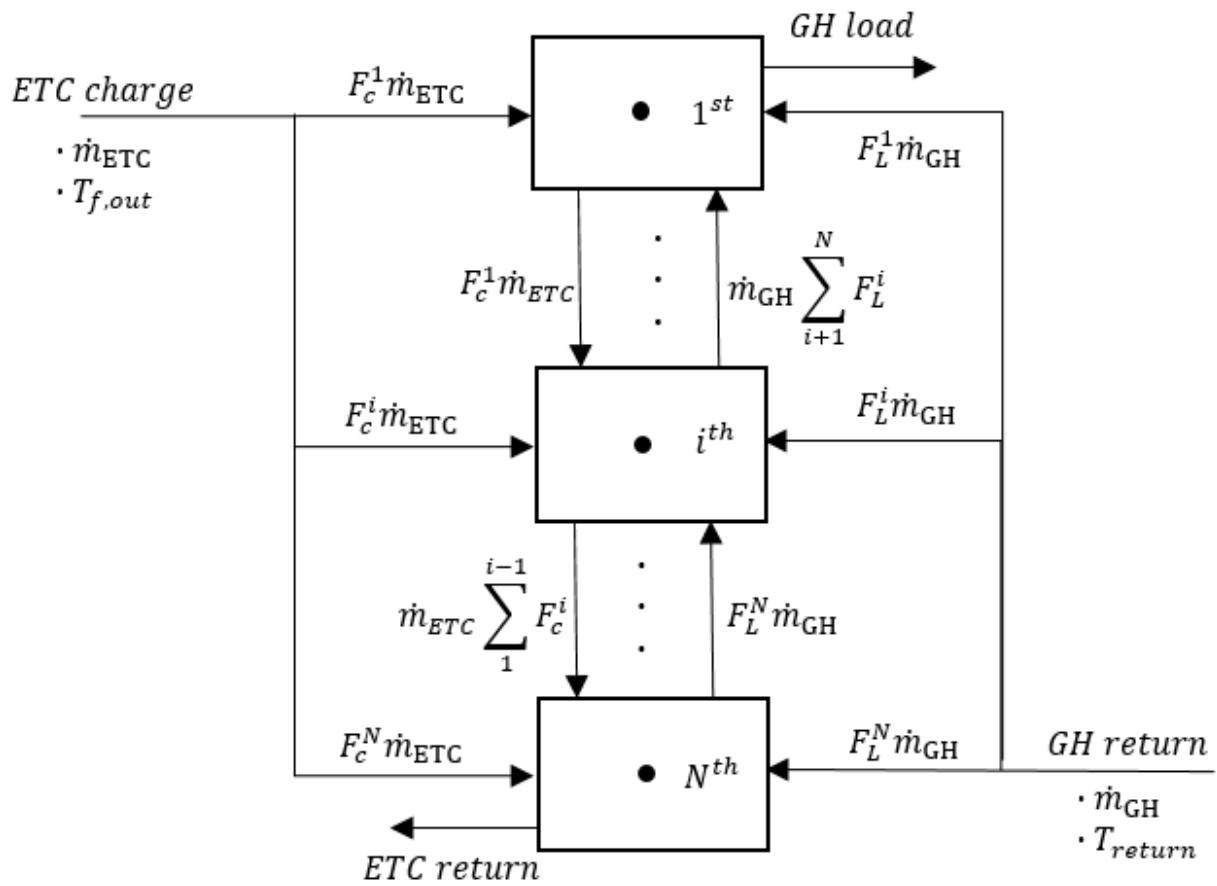


Figure 2-45 Representation of all the possible streams from charge and discharge of the pit dependent on the charge and return coefficients

$$\dot{m}_{mix}^i = \begin{cases} \dot{m}_{ETC} \sum_1^{i-1} F_c^i - \dot{m}_{GH} \sum_{i+1}^N F_L^i \\ 0, & \text{if } i = 1 \vee i = N + 1 \end{cases} \quad (0.70)$$

In Figure 2-46 is shown the mixing flow rate at the 16th node and it is clear that during the summer period, the higher mixing effects are due to charging of the pit, thus having a positive \dot{m}_{mix}^{16} , whether during winter period, the incoming load from the greenhouse is the more preponderant mixing effect, so having a higher percentage of negative \dot{m}_{mix}^{16} .

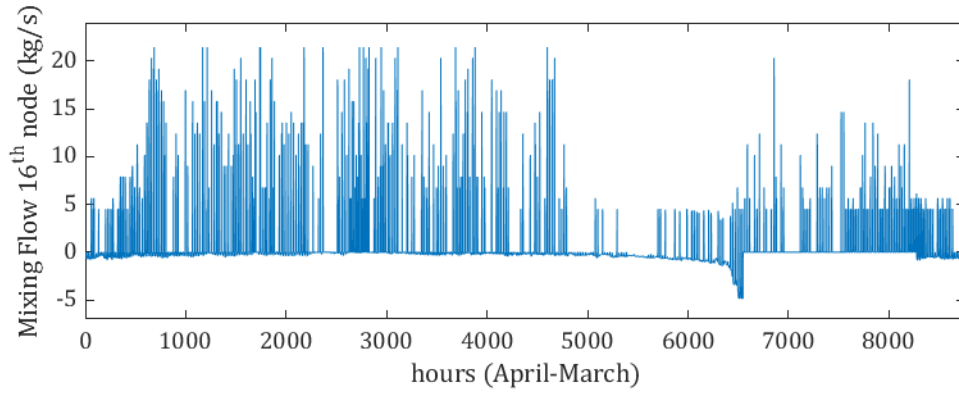


Figure 2-46 Yearly net flow rate on the 16th node

Having the net flow rate of every i^{th} node, simply by heat balance, it can be determined the heat influences from nearby nodes, \dot{Q}_{mix}^i , depending on the flow's direction, as shown in equation 0.71, given that if the flow is negative every i^{th} node is affected by its i^{th+1} node and inversely when positive affected by its i^{th-1} node (Arabkoohsar, 2016; John A. Duffie, 2013).

$$\dot{Q}_{mix}^i = \begin{cases} \dot{m}_{mix}^i cp(T^{i-1} - T^i), & \text{if } \dot{m}_{mix}^i > 0 \\ \dot{m}_{mix}^{i+1} cp(T^i - T^{i+1}), & \text{if } \dot{m}_{mix}^{i+1} < 0 \end{cases} \quad (0.71)$$

2.3.7 Temperature variation on the i^{th} node

Once determined all the net heat fluxes by charging, \dot{Q}_{charg} , discharging, \dot{Q}_{disch} , heat losses, \dot{Q}_{loss} , and induced mixing, \dot{Q}_{mix} , from equation 0.49 it is possible to determine the temperature change for every j^{th} hour at every i^{th} node.

As set in equation 0.49, the internal energy variations on the i^{th} node is dependent on the ratio between the product of the pit's volume, V^i , with its density ρ^i , specific heat cp^i and temperature variation during an hour, $(T^{i,j+1} - T^{i,j})$ by the time variation, Δt , in this case an hour, so 3600 seconds. So putting the desired temperature of the next hour in evidence, equation 0.72 was obtained for every node at any given hour of the year (Arabkoohsar, 2016; O. Paksoy, 2005).

$$\begin{aligned} T^{i,j+1} = T^{i,j} + \frac{\Delta t}{\rho^{i,j} cp^{i,j}} & (F_c^{i,j} \dot{m}_{ETC}^j cp^{i,j} (T_{f,out}^j - T^{i,j}) - F_L^{i,j} \dot{m}_{GH}^j cp^{i,j} (T^{i,j} - T_{return}^j) \\ & - (U_{NS}^{i,j} 2A_{NS}^i + U_{EW}^{i,j} 2A_{EW}^i + U_{bottom}^{i,j} A_{bottom}) (T^{i,j} - T_{soil}^j) - U_{top}^{i,j} A_{top} (T^{i,j} - T_{amb}^j) \\ & + \begin{cases} \dot{m}_{mix}^{i,j} cp^{i,j} (T^{i-1,j} - T^{i,j}), & \text{if } \dot{m}_{mix}^{i,j} > 0 \\ \dot{m}_{mix}^{i+1,j} cp^{i,j} (T^{i,j} - T^{i+1,j}), & \text{if } \dot{m}_{mix}^{i+1,j} < 0 \end{cases} \end{aligned} \quad (0.72)$$

Managing to achieve stratification required a study on a multi-node level, so being able to conduct the hourly temperature variation, allows to analyse the evolution of the seasonal heat storage facility on a layer basis.

Achieving stratification using the multi-node approach on an hourly-basis, allowed a dynamic analysis of the seasonal heat storage facility and once achieving the new temperature from equation 0.72, the loop was closed and it was possible to conduct the modelling of every terms of PTES, GH and UpETC for every $j^{th} + 1$ hour, thus concluding the formulation.

In Figure 2-47, it is shown the overall computation strategy in which all the modelling was based on and it is mainly based on three streams connected by the seasonal heat storage pit. The three units start by introducing an initial pit temperature, which was the last recorded one from the modelling of the first period. Given the initial temperature, each of the three initial values' streams follow to each system and the model starts.

The greenhouse, which can be followed by the green arrows, starts by introducing the initial load temperature, $T^{i=1,j=1}$ and dependent on the overall characteristics of the GH, weather and conditions set, the system of equations based on heat balance are conducted and the desired outputs are reached.

The solar collector field starts exactly like the GH unit, but in this case with inlet temperature set as the bottom of the pit's temperature, $T^{N,j=1}$. With this, a loop is created to determine the proper flow rate at which the outlet temperature is maximized on an equation's system and as outlet the charged flow rate, \dot{m}_{ETC}^j is obtained along with its outlet temperature, $T_{f,out}^j$.

In the seasonal heat storage unit, the same initial procedure is conducted based on heat balance and dependent on the incoming and outgoing fluxes from the solar collector field and to the greenhouse. After the collector and greenhouse's inputs are discovered, then the heat losses, gains/losses from node-to-node due to mixing flow effects are obtained for every i^{th} node and the temperature change, $T^{i,j+1}$ is reached. With this value is possible to start the loop once again until reaching the 8760th hour of the modelling period.

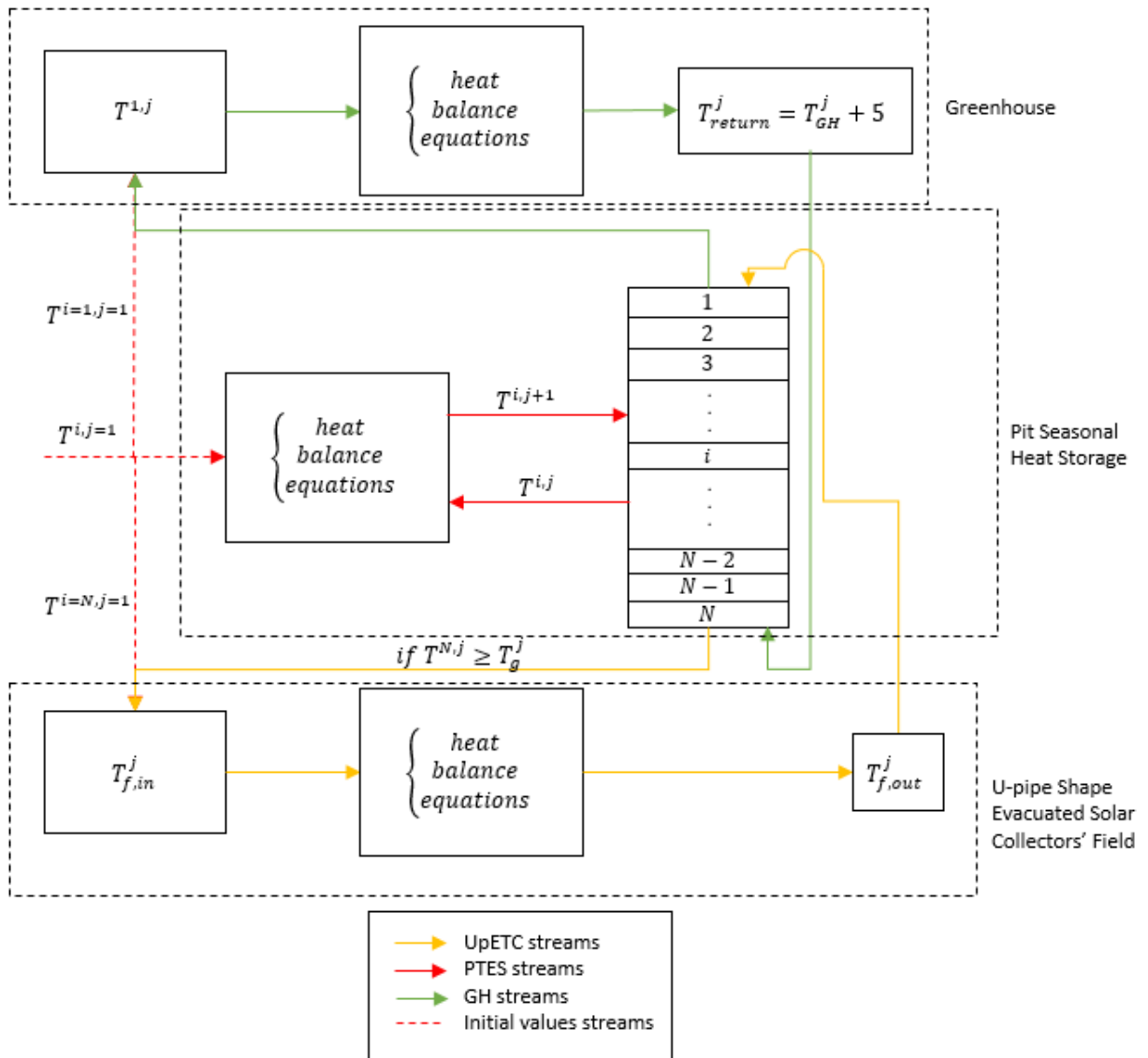


Figure 2-47 Representation of the overall modelling system with the streams coupling ETC-STES-GH

2.3.8 Pit-storage Efficiency

After conducting all the modelling process and getting the desired outputs, the efficiency was determined to assure the energetic feasibility of the system. For this, using equation 0.75, the efficiency of the seasonal heat storage was conducted as function of the ratio between the overall stored energy, \dot{Q}_{STES} , by the provided energy from the solar collectors, \dot{Q}_{ETC} .

The overall stored energy, set in equation 0.74, was determined as the difference between provided energy and the heat losses, \dot{Q}_{loss} , where the last one was obtained as the sum of losses of all $i \in [1:N]$ sub-volumes to the surroundings, as shown in equation 0.73.

$$\dot{Q}_{loss} = \sum_{i=1}^N \dot{Q}_{loss}^i \tag{0.73}$$

$$\dot{Q}_{STES} = \dot{Q}_{ETC} - \dot{Q}_{loss} \tag{0.74}$$

$$\eta_{STES} = \frac{\dot{Q}_{STES}}{\dot{Q}_{ETC}} \tag{0.75}$$

Finally, the storage unit managed to store a total of 436.6 MWh out of the 541.7 GWh provided energy from the solar collector field, with 105.7 MWh of total losses thus yielding an efficiency of 80.5 %.

2.4 VALIDATION OF ENERGY MODEL

Numerical modelling is very important to decrease initial project costs, but they require validity in order to be accepted as a feasible model (Singh & Tiwari, 2010). For this, the validations of the GH, ETC field and the PTES unit were conducted in respects to previous studies found in literature.

In order to validate the greenhouse setup, a comparison was made with the work done by Arabkoohsar et al., 2017, with similar greenhouse dimensions, U-value of covering material of 0.65 W/m² K and of ground of 0.5 W/m² K and monthly irradiation of the northern region of Iran.

As can be seen in Figure 2-48, the heat demand trend held quite similar to the reference work, showing small over prediction on some months of the discharge period and small under predictions on the charging period. All in all, the comparison showed an overall comprise of 91%, thus validating the model as a good predictive of greenhouse heat demand.

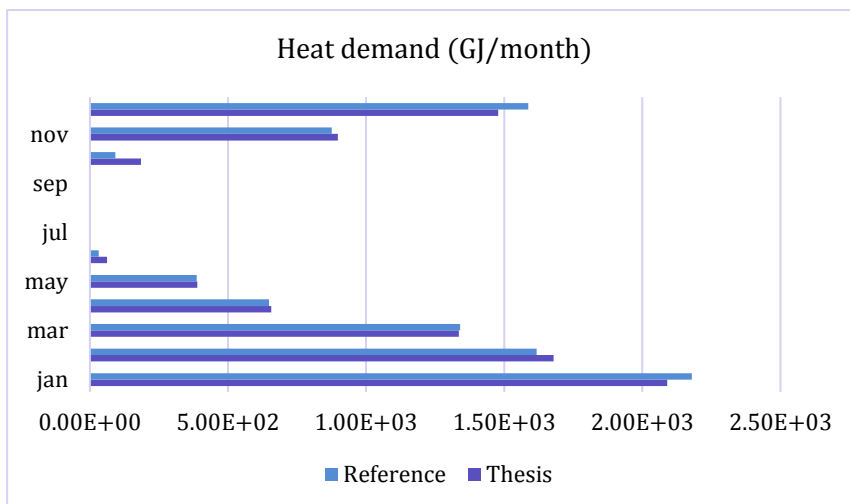


Figure 2-48 Validation of greenhouse model, comparing heat demand of reference work

In Figure 2-49, it is shown the comparison between the experimental data given by George & Kalaivanan, 2017, where they connect 15 U-pipe shaped evacuated tube collectors in series and using a constant inlet temperature of 20 °C and flow rate of 15 kg/hr · m² and with a spacing of 65 mm between U-pipe ends. The data points taken were from hour 11 till 15 and according to the Figure 2-49, there is a strong agreement between their results and those reported by the model used in this study. This is a strong approval of the validity of the developed model of this study.

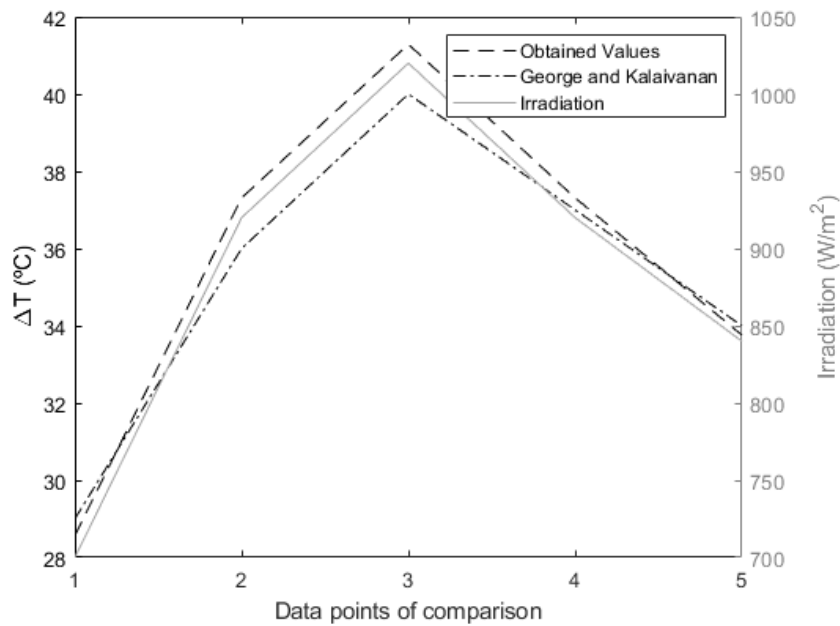


Figure 2-49 Collector's outlet temperature comparison for different hours of the day and available irradiation

Figure 2-50 validates the model of stratification used for the STES. For the validation of the model, it is used for a storage tank and operating conditions reported in an experimental work reported in Oppel, Ghajar, & Moretti, 1986. In this experiment, a stratified storage tank with a primary uniform temperature of 20.5 °C is heated up with a hot stream at 39 °C for different periods (0.5, 1 and 1.5 hours) at a constant flow rate of 1364 kg/h. The height of the tank, its diameter, the thickness of the insulation are 1.93 m, 1.16 m and 0.05 m, respectively. As seen, the model is accurately predicting the stratification within the tank and the temperatures of different nodes over the heating process, which is a strong proof of the reliability of the model used for the STES.

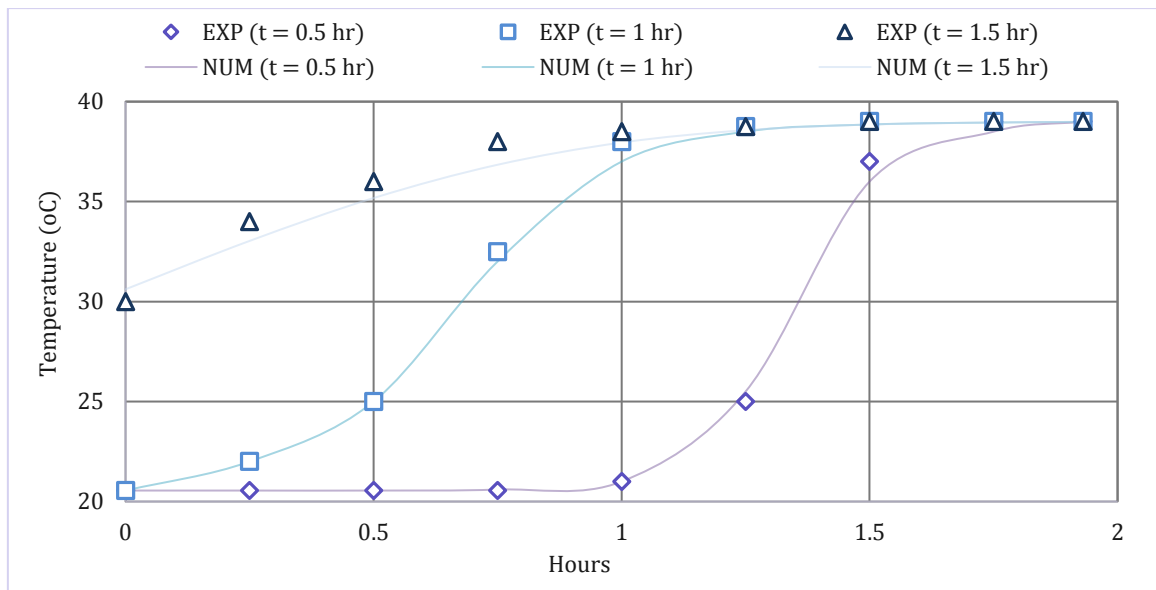


Figure 2-50 Validation between experimental data and values obtained by STES model

3 ECONOMIC ANALYSIS

Alongside with an energy analysis, the economic viability is fundamental to determine if a setup is feasible to implement in the market, since a technology can be highly energetically profitable, but may be far away from being lucrative. For this, an economic analysis was implemented, where based on the dimensions of the pit seasonal heat storage, energy yield, requirement of external energy sources, market costs of heat and implementation costs, the system's net present value was determined assuming a 20 year running period, according to the reports of PlanEnergi, 2013, 2015; T Schmidt, Mangold, & Müller-Steinhagen, 2003.

The net present value (NPV) represents the cumulative discounted cash flow of the considered useful life, i.e. on a 20 year period it will provide the sum of the difference between the benefits from the provided heat to the greenhouse and the initial costs, auxiliary demand tariff and the charge from running the facility (O. Paksoy, 2005).

The NPV was calculated via equation 3.1, where P , B , $CAPEX$, r and t are the costs of production, benefits, operational and running costs, interest rate and years.

$$NPV = CAPEX - \sum_{t=1}^{t=20} \frac{B - C}{(1 + r)^t}, \quad \text{where} \quad (3.1)$$

$$CAPEX = cost_{STES} V_{STES}$$

$$B = cost_{heat} (\dot{Q}_{GH} - \dot{Q}_{aux})$$

$$C = cost_{run} (2\% \dot{Q}_{GH})$$

The costs of implementation, $cost_{STES}$, the rated price of heat, $cost_{heat}$ and running costs, $cost_{run}$ are values obtained from literature, assuming similar seasonal heat storage units and shown in table (IEA, 2015; O. Paksoy, 2005; PlanEnergi, 2013, 2015; T. Schmidt et al., 2004).

The report from IEA, 2015 states that overall costs of a pit seasonal heat storage are concentrated from 40 – 250€/MWh, so as reference from PlanEnergi, 2015, the construction costs of the charging unit were determined. As the report stated, excluding piping costs to district heating and heating pumps that do not constitute in this case study, their construction costs for a PTES unit with 75000 m³ was roughly 7.4 M€, thus yielding a cost per unit volume of 98 €/m³.

From the data of Danish Energy Agency, 2016, the heating production cost without operation and maintenance costs round the 58 €/MWh, thus considered equal to the $cost_{heat}$. The running costs, $cost_{run}$, were considered as 2% of the construction costs as done by O. Paksoy, 2005; PlanEnergi, 2015.

From the gathered information, Table 3-1 was created to show the inputs used on the net present value analysis done for a 20 years period.

Table 3-1 Values considered for NPV economic analysis

V_{STES}	\dot{Q}_{GH}	\dot{Q}_{aux}	$cost_{STES}$	$cost_{run}$	$cost_{heat}$	t	lifetime
m^3	MWh	MWh	€/m ³	€/MWh	€/MWh	years	years
2000	591	159.6	98	1.96	58	[1: 20]	20

Given that the importance of the interest rate on a NPV study and that it is very variable, several scenarios with different interest rates were conducted, in order to understand the feasibility of this system (Djørup, Sperling, & Østergaard, 2020; Grøn Energi, 2018). In Figure 3-1, can be seen 4 case scenarios using interest rates of 1, 2, 5 and 10%. Out of the 4 cases, having 10% interest rate concludes that the system does not turn almost any profit on a 20 year lifetime, whether for the remaining, there is a positive revenue, reaching its maximum of 209000€ of profits with 1% interest, having a payback period of 9 years. The remaining 2 and 5% scenarios demonstrated a turn point after 10 and 12 years, respectively.

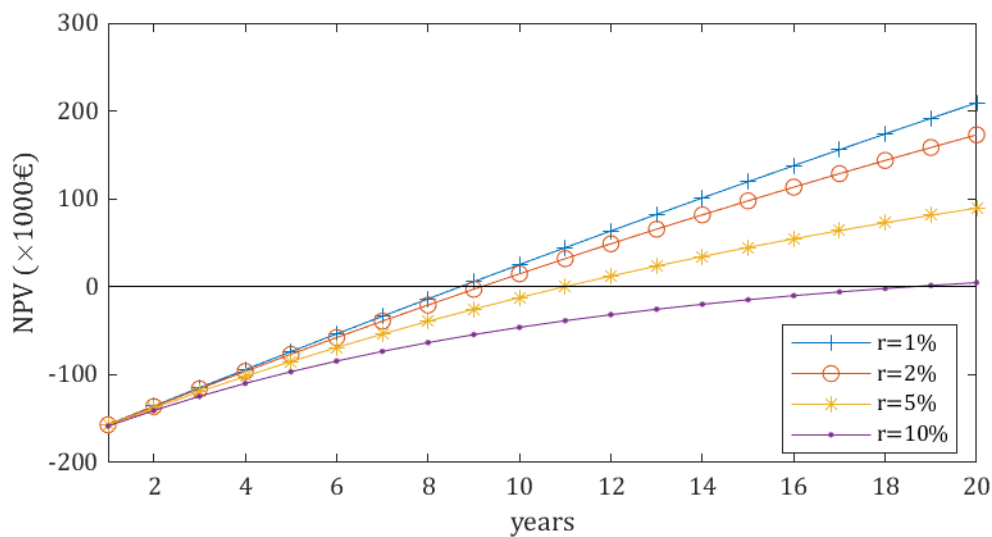


Figure 3-1 Net present value evolution for different scenarios of interest rate

As shown by Djørup et al., 2020, the interest rate in Denmark has been decreasing for the last 30 decades being at values below the 2%, thus reaching the conclusion that for the given market trend, this setup would be profitable, reaching 150 to 200 thousand euros of positive net cash flow, with an estimated payback period of 9 to 10 years.

4 RESULTS AND DISCUSSION

The results from the modelling process for the charging-storing system and beneficial output will be shown in this chapter, providing the relevant outputs and aiming to prove if the assumptions and behaviours set were correspondent with the results.

4.1 GREENHOUSE

Modelling a greenhouse showed to be a complex system, depending on the local weather, specific optimum conditions of produce growth, which will affect the materials to use, available solar irradiation, ventilation rates and the heating requirements (Von Zabeltitz, 2011). The greenhouse modelled in this study had as reference the work done by Mahmood Farzaneh-Gord et al., 2013, with a built of double polycarbonate walls, separating it from the ambient surroundings, with a thickness of 8 mm and solar irradiation transmissivity of 0.84. It was considered with a ground area of 2000 m², a volume of 6500 m³, and a ranging minimum temperature of 18–22 °C, with the purpose of creating an optimal micro-climate for tomato growth in the region of Aarhus, Denmark and based on hourly weather data.

In Figure 4-1 it is shown the heat that was lost from the induced ventilation and through walls and soil. In both streams can be seen a very similar pattern, where during the summer the requirements are lesser than during winter, given the lower variation between internal and ambient temperatures. There were 760 MWh of total heat lost to the environment from both ends, where ventilation alone accounted for 67% of it.

Given the much larger impact from ventilation, it can be stated that the system would profit greatly from extra passive mechanisms, like the insertion of a ventilation heat recovery system (Ooteghem, 2010; Taki et al., 2018).

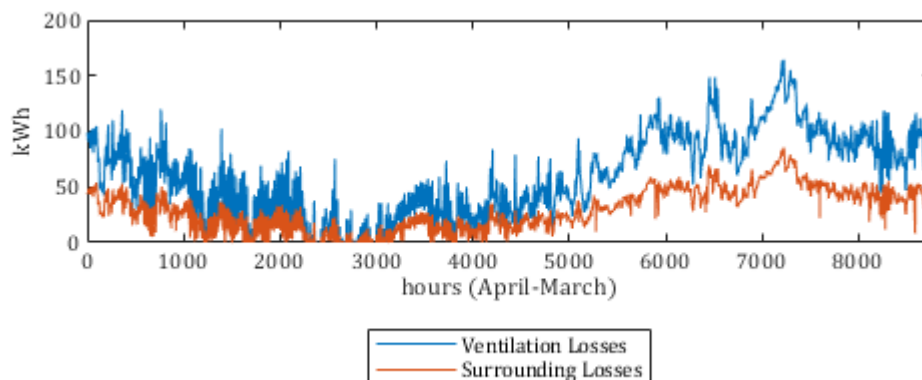


Figure 4-1 Ventilation and heat losses to surroundings

The heat losses on a greenhouse depend greatly on the surrounding temperatures, but as Bendimerad, Chermiti, Mahdjoub, Draoui, & Abène, 2011 suggested, the wind speed is also

an important factor and from Figure 4-2, it was made the comparison between heat losses from the walls and the year-round wind speed. The pattern of both seems similar having in common several picks, like the ones between the 6000 and 7000 hours, where wind speed increases were accompanied by heat loss rises, thus concluding that wind was a strong decisive factor of heat losses through the covering film.

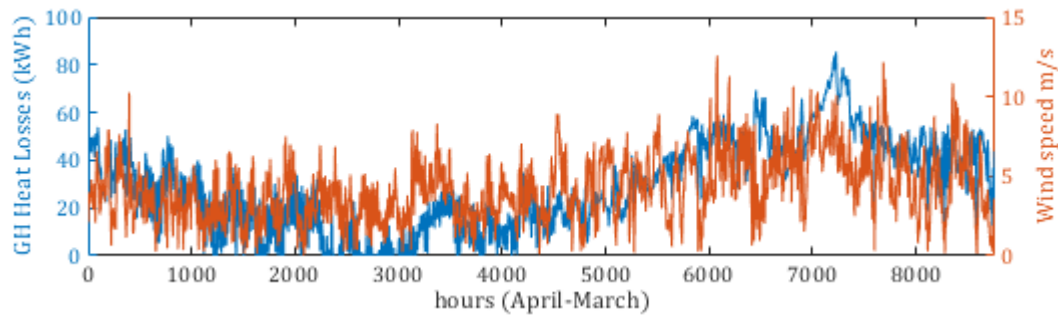


Figure 4-2 Graphical comparison between wind speed and greenhouse heat losses from the walls

The heat losses through the soil were very residual, showing a 1.5% influence on the heat losses to surroundings and like it can be seen in Figure 4-3, its trend had some influence due to the soil's temperature variation along the year, and due to the semi-infinite approach, becoming less and less significant as time passed. (Jiji, 2006)

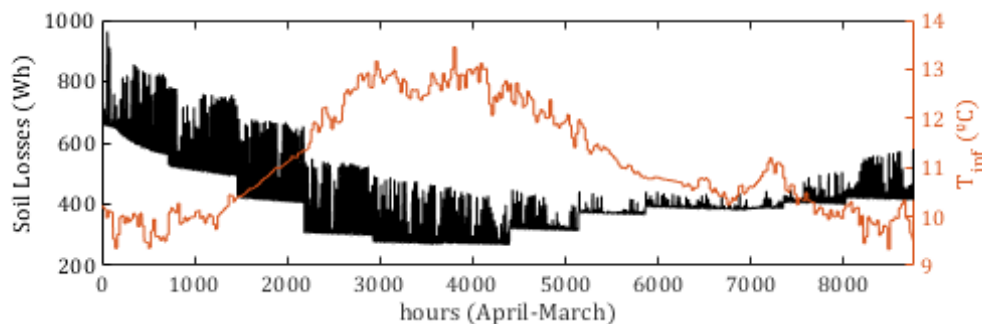


Figure 4-3 Comparison between the greenhouse heat losses through the soil and average soil temperature

As mentioned in chapter 2.1.3, a transient approach was taken to conduct the calculations of heat losses to the soil assuming it as a semi-infinite bulk region and with soil temperature dependent on a correlation that would provide the appropriate temperature on specific depth as function of the temperature variations of the ground's surface.

Lavine & Bergman, 2008; Suárez, Pino, Rosa, & Guerra, 2019; Tsui, Lin, & Ding, 2014 have demonstrated that a cold bulk region close to a hot surface will tend to increase its temperature along time, approaching the surface's temperature.

As shown in Figure 4-4, the distance between the soil's surface and depth at which the soil is at T_{soil} , increases in a logarithmic way, thus becoming less meaningful on the heat losses as time passes. (Bergman et al., 2011; Tsui et al., 2014)

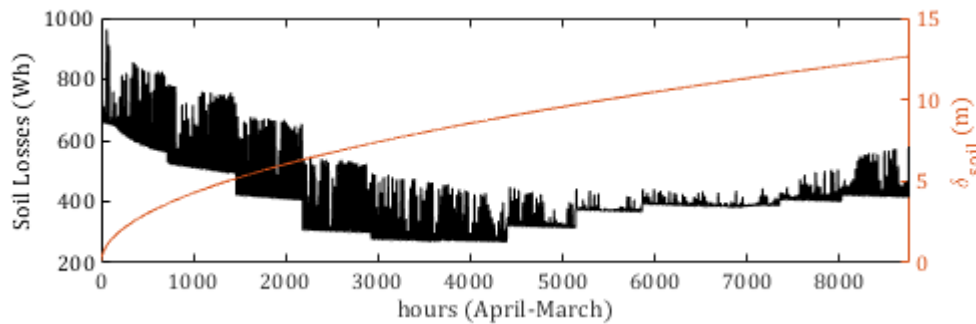


Figure 4-4 Greenhouse heat losses from interior to soil and distance from soil's surface and the point of depth where the temperature is considered constant

From Figure 4-5, it can be seen the available solar irradiation upon the greenhouse and the heat losses induced from neighbouring regions. The solar irradiation accounted for a large energy provider of the greenhouse, allowing to sustain its minimum temperature set on this project, just by greenhouse effect, for 34.3% of the time by its own, whereas the energy requirements from the greenhouse were more noticeable during the winter periods given the lower ambient temperatures and low solar irradiation. It can also be seen that during the months of November till February, the solar irradiation was not nearly enough to cope the demand, which inferred a higher necessity of heat from the external source during this period (Arabkoohsar et al., 2017; Henson & Henson, 2006).

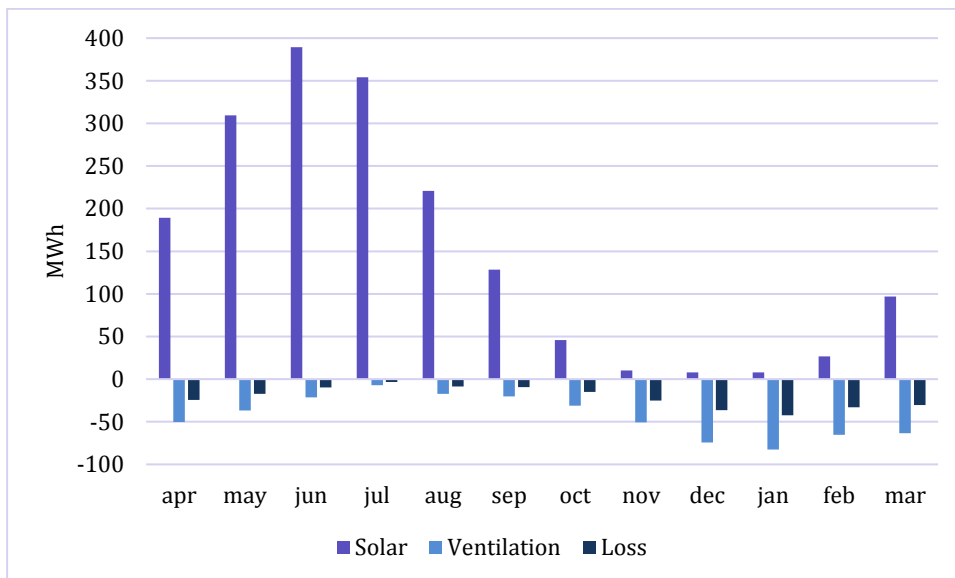


Figure 4-5 Graphical representation of available solar irradiation and heat demand from ventilation and losses from walls and soil of the greenhouse

In Figure 4-6, it can be seen the total heat demand that could not be sustained by solar greenhouse effect for each month of the year, with the quota of each energy source, being STES and auxiliary. During the months of April to November, the seasonal heat storage held the total requirements, whereas during the remaining months, the DH auxiliary source was necessary, especially for the colder months of January and December. When comparing with the work of Arabkoohsar et al., 2017; Mahmood Farzaneh-Gord et al., 2013, the demand pattern of the greenhouse showed a rising necessity of external energy sources from July till January, and a decrease for the remaining.

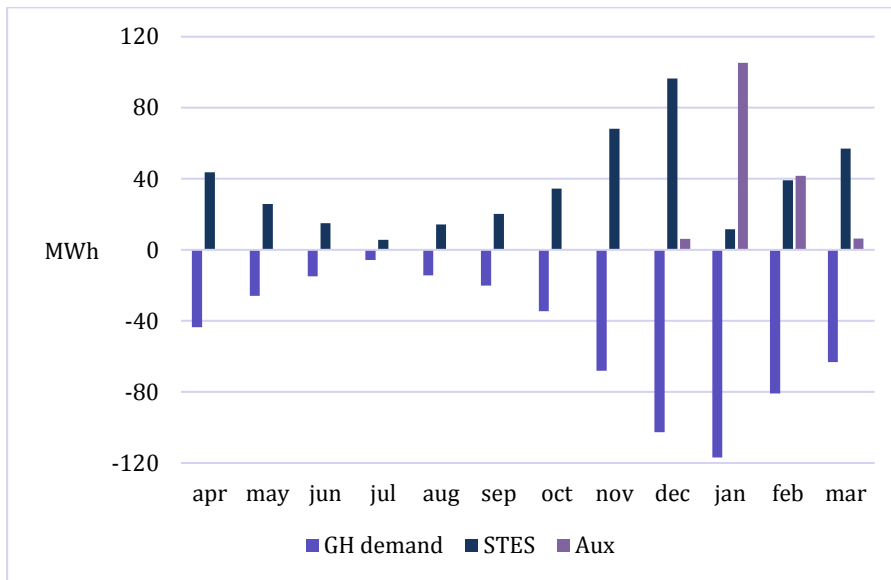


Figure 4-6 Greenhouse monthly heat demand and quota of heat provided from STES and auxiliary heat sources

As shown in Figure 4-7, every time the solar irradiation could not cope with temperature demand, energy from a pit seasonal heat storage and auxiliary power source would be used for its climate-control. Summing all hours, there was a total heat demand from external sources of 591 MWh, from which 73% was provided by the stored heat of the pit and the remaining from the auxiliary energy source.

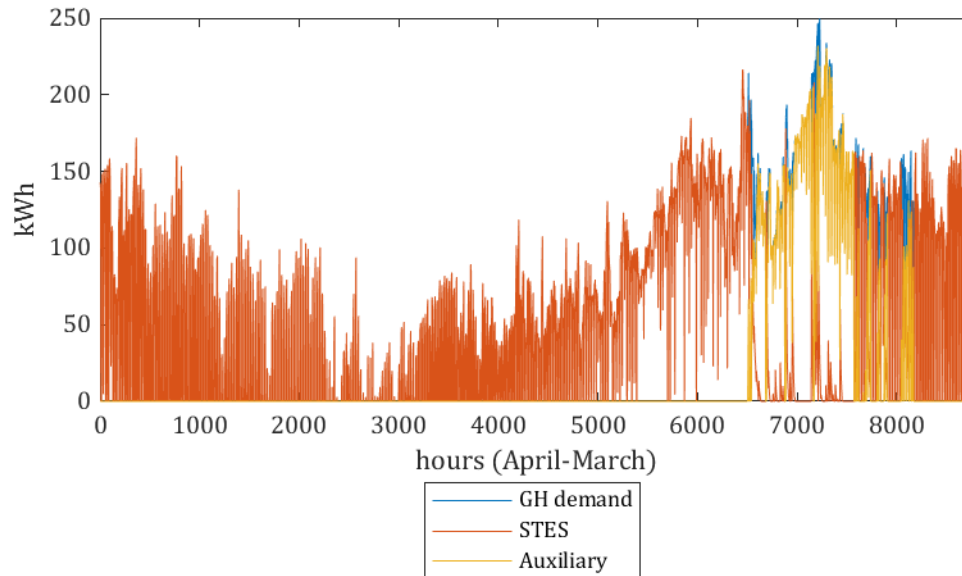


Figure 4-7 Hourly greenhouse heat demand and provided heat from the pit and district heating auxiliary

The modelling of the greenhouse was primordial to understand its temperature and heat demand patterns, in order to be able to model the energy source accordingly (Canakci & Akinci, 2006; Krasimirov Pavlov, 2014).

4.2 SOLAR COLLECTORS

The solar collector field was modelled assuming a variable flow rate would provide better output results. As can be seen in Figure 4-8 the highest availability of irradiation is shown during the warm period of the year and consequently from Figure 4-9, it is the region where the flow rate is larger, thus proving the agreement that when the irradiation is too high, the system will adapt by increasing the flow rate. On the other hand, during low irradiative days, it can be seen that the flow rate was considerably smaller, thus increasing residence time in the collectors (Badar et al., 2012; Naik et al., 2016).

The captured energy from the collectors has shown fairly low results when comparing with the solar availability. As stated by Braun, Klein, & Mitchell, 1981; John A. Duffie, 2013; Kumar & Rosen, 2011, the decrease of Volume/Area ratio between storage and collectors will cause lower solar coverage, given the faster charges of the pit and high inlet temperatures coming from the bottom of the pit.

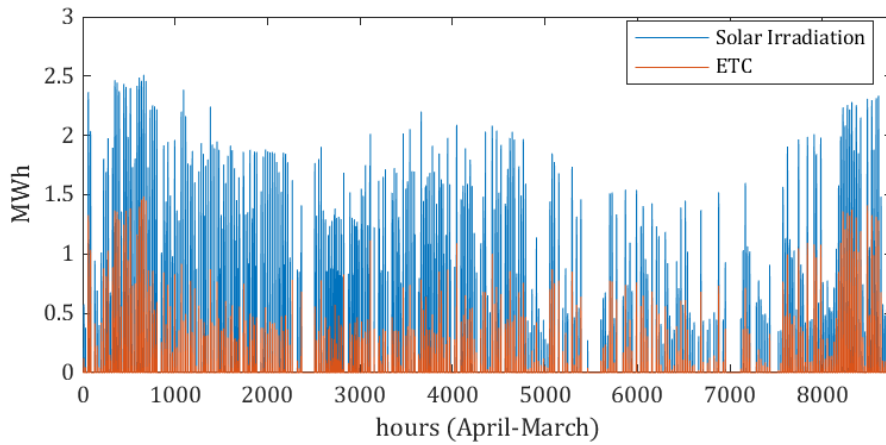


Figure 4-8 Available irradiation and absorbed heat from the collector field

By comparison when looking at Figure 4-8 and Figure 4-9, can be seen that regardless of the low solar coverage spotted during the charging period, the outlet temperature reached its maximum value for the most part of the time, concluding once more, that given the high incoming temperatures from the storage, the solar availability was too high for the conditions imposed on the collector's charging process (Abdoly & Rapp, 1982; Neupauer & Kupiec, 2017).

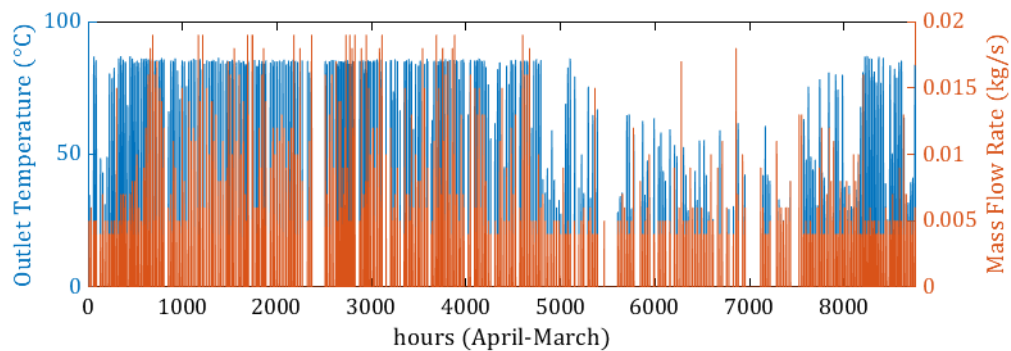


Figure 4-9 Variation mass flow rate on each group of series

In Figure 4-10 it is shown the temperature variation between inlet and outlet of each group of series, showing the highest temperature yields during beginning and end of the period. In

this hours the maximum temperature rises were of 60 °C, thus reaching an average maximum 3 °C increase per collector (George & Kalaivanan, 2017).

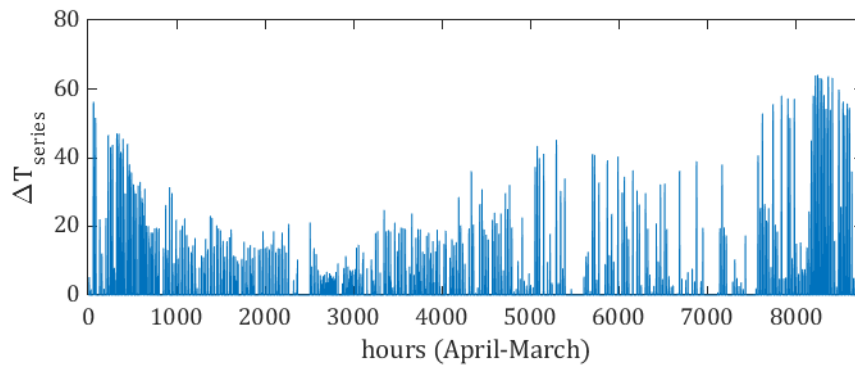


Figure 4-10 Temperature difference between inlet and outlet of each group of series

When analysing the daily efficiency and mass flow rate of the ETC field in Figure 4-11, both have a similar pattern, with regions with higher flow rates achieving higher efficiencies of the solar collectors, as the residence time in the tubes was lesser, thus lowering heat losses to the surroundings, as stated by Badar et al., 2012.

In the end, the solar collector field held a low efficiency of 33,5%, which as stated by Dannehl et al., 2013; O. Paksoy, 2005, given the low volume-area ratio, the effectiveness of solar collectors decreases due to higher inlet fluid temperatures, hence lower solar coverage.

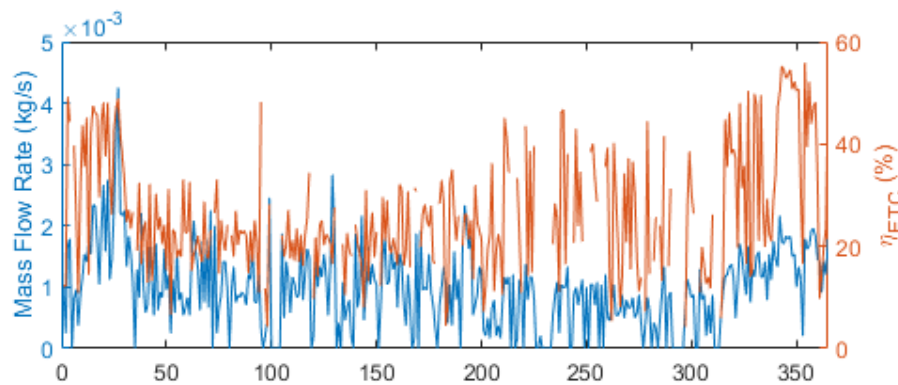


Figure 4-11 Daily ETC field's mass flow rate and efficiency

From Table 4-1, it can be seen the main important aspects of the solar collector’s modelling, where \dot{Q}_{ETC} , I , $\bar{T}_{f,out}$, $\bar{\Delta T}_{out-in}$, \bar{m}_f , \bar{U}_{loss} , η_{STES} , A_{ETC} , A_{total} are the absorbed heat per unit area, the available irradiation per unit area during the working hours, average yearly outlet temperature, average yearly temperature difference between inlet and outlet of each series, average yearly mass flow rate of each series, overall efficiency, total aperture area and total solar collector field’s area, respectively.

Badar et al., 2011 have demonstrated that for evacuated tube collectors, the U-value should be in the bounds of $2:4 W/m^2K$, whereas Y. Gao et al., 2014 state that for UpETC should be $0.8:2.4 W/m^2K$, thus showing a comprise on the U-value obtained in simulations.

The overall efficiency, when compared with values on the bounds of 30:60 % from Yan Gao et al., 2013; George & Kalaivanan, 2017, shows that it is in accordance with researched results.

Table 4-1 Outputs from the evacuated tube collector's modelling

\dot{Q}_{ETC}	I	$\bar{T}_{f,out}$	$\overline{\Delta T}_{out-in}$	\bar{m}_f	\bar{U}_{loss}	η_{ETC}	A_{ETC}	A_{total}
kWh/m^2	kWh/m^2	$^{\circ}C$	$^{\circ}C$	kg/s	W/m^2K	%	m^2	m^2
180.6	539.4	59.5	15.9	0.006	2.1	33.5	3000	3690

Finally, it can be assumed that the UpETC modelling provided accurate results, with comprising with data from the literature and managed to provide a total of 33.5 % of the year-round available solar irradiation.

4.3 PIT STORAGE

Given the solar irradiation's intermittent accessibility, solar collectors have been coupled with heat storage units, to cope the necessities, regardless of the solar availability (T Schmidt et al., 2003). The seasonal thermal energy storage pit suited the purpose of harvesting the summer high irradiative days and dispatch it to the greenhouse during the winter, when the heat requirements were greater. From Figure 4-5, can be seen that the energy needs were not solely during winter time, which brings the conclusion that the storage unit was also able to sustain any night time necessities, regardless of the period of the year (Djemoui et al., 2018).

In Figure 4-12 it is shown the temperature evolution on the pit, with initial temperature gradient from the last hour of the simulations from the first year. As suggested by Tulus et al., 2016, the pit was initially charged up to the storing period, in which the loads from the collector field would be mainly to contradict heat losses and eventual discharges from the greenhouse night needs. Starting from September/October, the greenhouse started having lower availability of solar irradiation and with more distressing weather conditions, demanded the discharge of the pit from the highest heat quality region, maintaining optimal internal temperature on the GH. The discharging period would last until no more heat could be provided, thus having a backup auxiliary energy source to hold the lack of heat from the pit.

Achieving stratification was one of the goals of the modelling procedure and as can be seen if Figure 4-12, the temperature of each of the 32 nodes during the charging and discharging

period shows that a gradient was held at any given hour, until the moment that it became fully charged (Tulus et al., 2016).

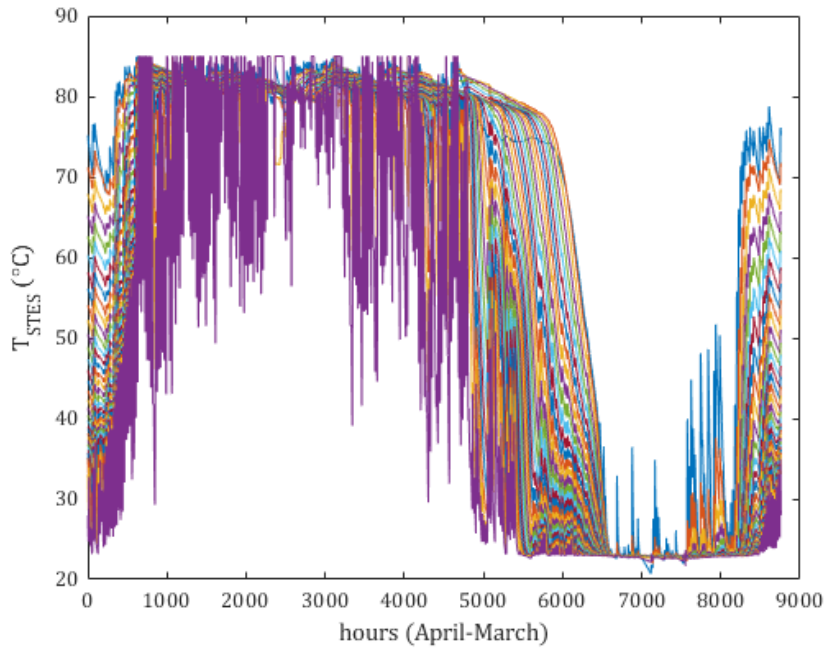


Figure 4-12 Pit storage temperature evolution

From Figure 4-13 can be seen the evolution of the temperature gradient of a typical hour of the 15th day of each month along its height/node. As demonstrated by PlanEnergi, 2015, the months of January and February demonstrated an almost fully-mixed tank with temperature of 20°C, indicating it as fully discharged, hence the indicated higher auxiliary need on these months, shown in Figure 4-6. From the month of March till June it is possible to see a generated thermocline region increasing as time passed, thus indicating a good stratification happening on the pit. On the months of May till August, the thermocline region almost faded, given there was a nearly equity of temperature on the nodes, reaching the states of fully-mixed and fully-charged (Dincer & Ezan, 2018). On the ongoing months, as the higher portion of discharge demand from the greenhouse started, the temperature of the pit decreased gradually having always higher impact from bottom to top nodes, reaching a smoother de-stratification, thus allowing the pit to have higher quality of heat during this period. As discharging mode progressed, all energy was removed from the unit reaching the states of fully-mixed and fully-discharged on the month of January.

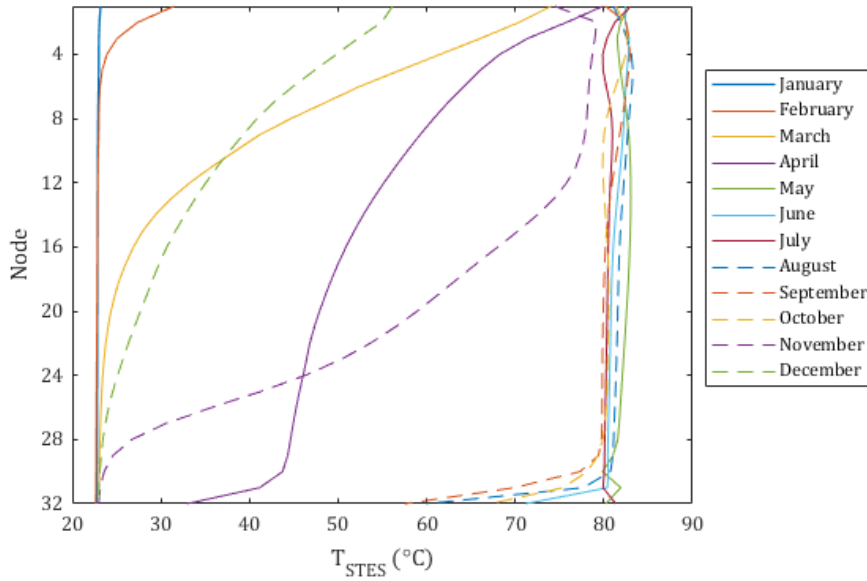


Figure 4-13 Temperature gradient of a typical day of each month of the running period

One thing noticed from the months of August till October, was that even though almost all the pit was fully-charged, on the bottom there were accounted return loads from the greenhouse, thus decreasing the bottom nodes' temperature, which indicated that even during the charging period, the unit was able to provide heat to the night hours of the greenhouse with very little effect on the overall thermal state of the medium (Tulus et al., 2016).

The neighbouring regions of the pit induced heat losses throughout the year given their lower temperatures and higher weather variability, as can be seen in Figure 4-14. The heat losses from the figure bellow demonstrate a similar trend amongst each other, where higher losses were accounted during the charging period given the higher temperature difference between pit a surrounding ambient and soil. Given the more stable variations of temperature set on the soil, it can be seen a smoother pattern for bottom and walls' heat losses, when compared with the top cover, given that both ambient temperatures and wind conditions were highly variable.

The losses, when summed, accounted for a total of 105 MWh of heat lost, with the top cover yielding the higher impact of 53.7%, thus concluding that the more important region to isolate is the top cover (Thomas Schmidt et al., 2018) and proving that top heat losses impose the higher negative thermal effect on a pit as Ochs et al., 2020 suggested.

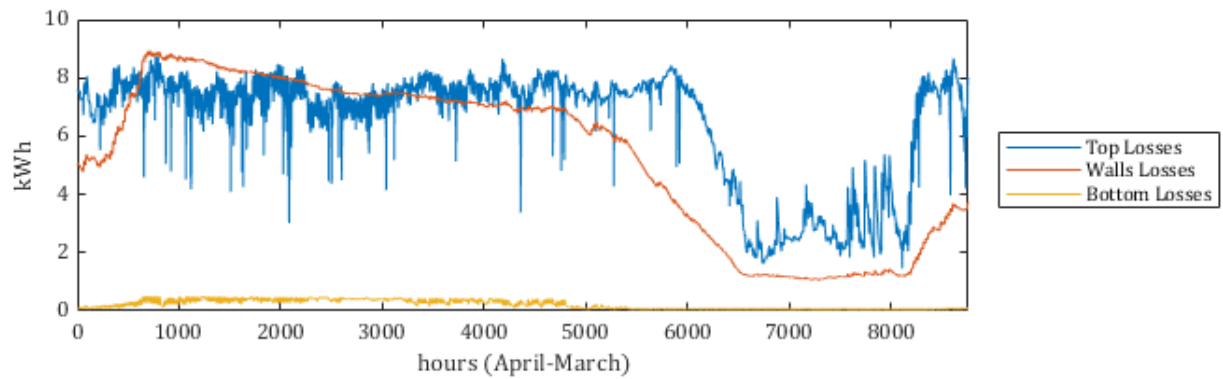


Figure 4-14 Heat losses from top cover, walls and bottom of the pit

In Figure 4-15(a) can be seen the soil's temperature variation along the year, with higher fluctuations on the nodes closer to the soil's surface, hence having more interactions and dependability with the outer weather conditions. As depth increases, this fluctuations are lesser, up to the point where a constant temperature is reached (Baggs, 1983; Cui et al., 2011). Figure 4-15(b) demonstrates the node dependent heat interactions with the soil on the first year period of simulations and when compared with Figure 4-15(a), its unsteadiness is greater in nodes with higher fluctuations, i.e. with upper nodes (Suárez et al., 2019).

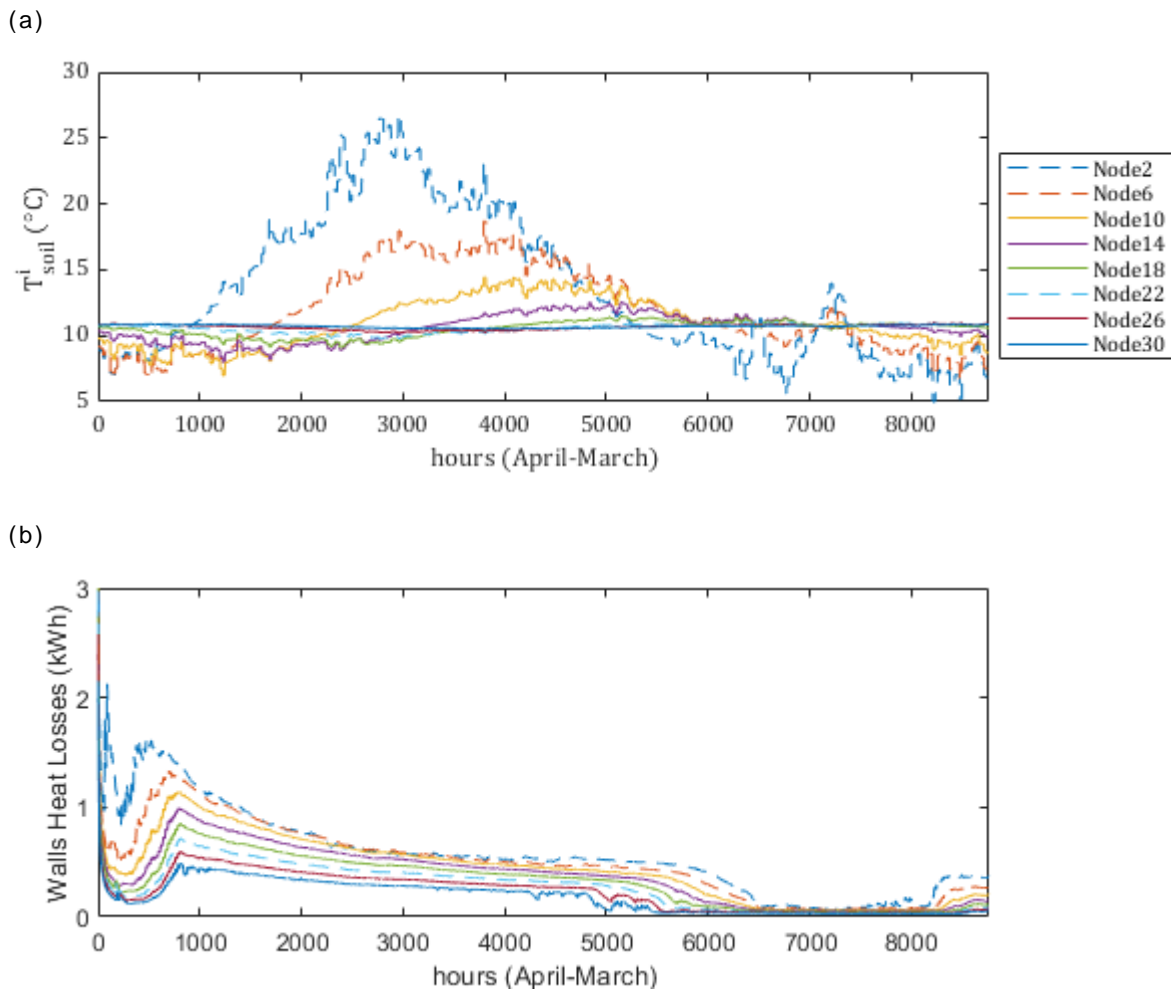


Figure 4-15 Soil temperature variation dependent on depth/node (a) and heat losses from walls to soil (b)

The heat losses from the bottom and walls were determined dependent on a semi-infinite transient heat conduction approach, predicting that as time passes a thermal gradient will be created as distance increases from the surfaces of the pit, up to the point that no more thermal penetration can be achieved on the soil. Given this assumption, the distance δ_{soil} was plotted in Figure 4-16, for the two years period of this study, in which can be seen a logarithmic rise, reaching 18m at the end of the second year.

Using the semi-infinite approach led to the conclusion, that due to thermal diffusion a barrier is created around the pit, which will induce less impact on the thermal interaction with the soil, thus perceiving the statement of Thomas Schmidt et al., 2018, that there is no economic benefit in placing insulation on the walls and bottom of the pit. On the other hand, this assumption requires validation due to lack of literature results.

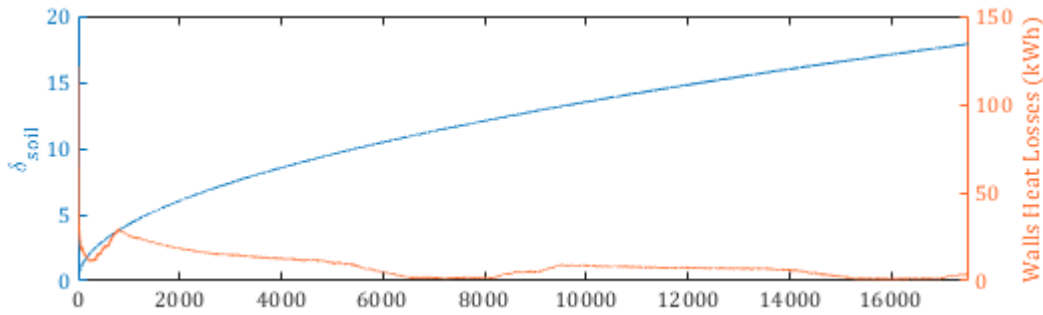


Figure 4-16 Distance of the soil at constant temperature T_{soil}^i and heat losses through walls on a two year period

In Figure 4-17 it is shown the daily temperature pattern on the top, middle and bottom nodes of the pit. The top node temperature is kept at high constant levels for the most part of the year, but the winter time, given that the tank is completely discharged. As demonstrated by PlanEnergi, 2015, in the beginning of the discharging region, the temperature of node 1 falls below some of the nodes beneath, which contradicts stratification quality. A possible explanation is that the sudden rise in demand induces a fast discharge of the top node and the lack of incoming charged fluxes from the collector field will create a delay on the time to thermally diffuse with the neighbouring nodes. On the other hand, given that during the storing period the highest impacts on heat losses were from the top cover, can explain the fact that a more thermally stable node, like node 16 or 32, could surpass the top node's temperature for brief moments.

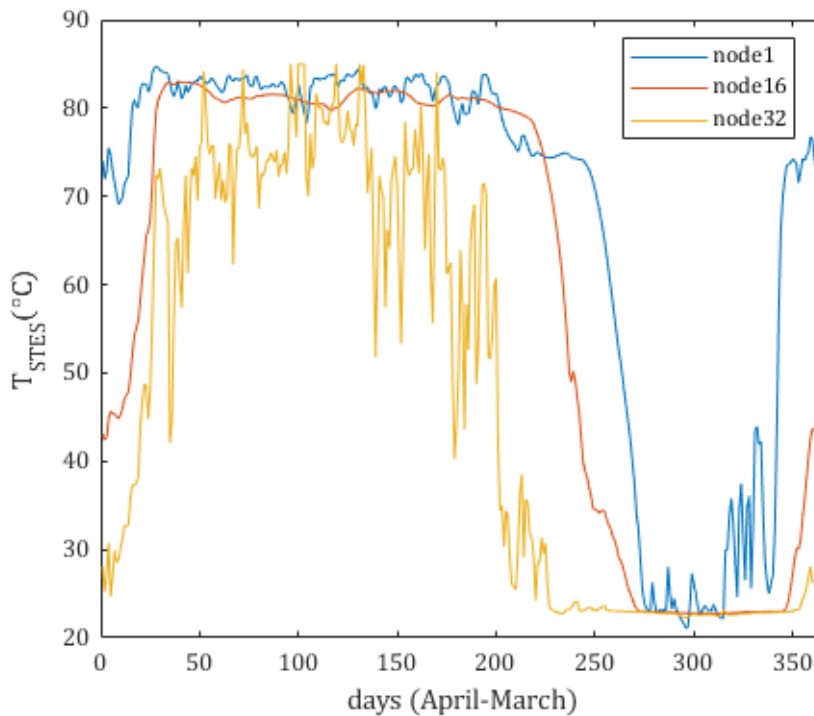


Figure 4-17 Average daily temperature evolution on top, mid and bottom nodes

Lastly the overall results from the pit are shown in Table 4-2, where η_{STES} , \dot{Q}_{charg} , \dot{Q}_{STES} , \dot{Q}_{disch} , \dot{Q}_{loss} , \bar{U}_{top} , \bar{U}_{wall} , \bar{U}_{bottom} , N_{nodes} , V_{STES} , ΔT_{max} and ΔT_{i-f} are the efficiency of the pit, charged heat from ETC, discharge to the GH, average overall heat transfer coefficient of top, walls and bottom, number of considered nodes, volume of pit, temperature difference between maximum temperature and minimum of the pit and temperature difference between the final and initial hour of the second period.

Table 4-2 Overall final parameters of the STES obtained from the calculations

η_{STES}	%	80.5
\dot{Q}_{charg}	MWh	541.7
\dot{Q}_{STES}	MWh	436.0
\dot{Q}_{disch}	MWh	431.4
\dot{Q}_{loss}	MWh	105.7
\bar{U}_{top}	W/m ² K	0.37
\bar{U}_{wall}	W/m ² K	0.15
\bar{U}_{bottom}	W/m ² K	0.15
N_{nodes}	—	32
V_{STES}	m ³	2000
ΔT_{max}	°C	64.3
ΔT_{i-f}	°C	0.25

From Table 4-2 it can be seen that a residual amount of energy was left in the pit, which can also be concluded by the positive, although rather small, value of the temperature difference between initial hour and final hour of the pit, ΔT_{i-f} .

Lastly, it can be stated that the pit storage formulation taken in this study provided a satisfactory behaviour, managing to provide 431.4 MWh of heat to the greenhouse, so coping 73% of the demand and yielding an overall yearly efficiency of 80.5%.

5 CONCLUSIONS

This thesis had the aim of understanding the thermo-economic feasibility of a solar pit thermal energy storage unit, using water as medium and a charged by an evacuated tube collector field, with the purpose of reaching the heat demand of a tomato growth greenhouse farm, thus holding internal minimum temperatures to provide tomatoes an optimal microclimate for ultimate sprout.

Understanding the heat demand pattern of the greenhouse manifested a primordial goal to properly set dimensions and conditions of both PTES and UpETC units. Reaching this trend, led to a search of the available solar irradiation on the greenhouse, its possible weather impacts and so, determining the materials and dimensions to be implemented.

The greenhouse showed a controlled microclimate from direct solar irradiation on 33.4% of the time and for the remaining part of the studied period, requiring aid from an external source. The heat demand was more impacted by air renovations, which led to the conclusion that passive heating systems, like ventilation heat recovery systems, could be implemented to decrease heat needs. Although, the general most required energy from the greenhouse was spotted during the winter season of the year, it was also denoted heat demands on the remaining months, coming to the conclusion that days with harsher weather conditions and night time heat losses cannot be entirely sustained by solar irradiation.

To stand the heat demand, a solar collector field of 3000 m² with U-pipe shaped evacuated tube collectors was used to harvest the solar irradiation. These collectors were modelled with a transient flow rate, dependent on highest outlet temperature yield, aiming to increase solar coverage, in which flow rate adaptability was reached, showing a good comprise of the system.

When determining a volume-area ratio lower than 1, the solar coverage decreased, but coming as necessity so that economical utility could be reached. The collector field provided 541.7 MWh of energy to the storage unit, having an overall efficiency of 33.5%, which showed to be in-between expected bounds.

Solar irradiation is an intermittent energy source that often possesses a far deviation from attainability and necessity, making storage units a crucial part on solar heating systems. In the simulations, the collector field reached 541.7 MWh and the heat demand of the greenhouse was of 591 MWh, which could indicate that solar collectors directly connected to the greenhouse could cope most necessities. In reality, during the discharging period, the harvested energy from the ETC field was lower than 30% of its total yield, whereas the greenhouse showed more than 67% of the total demand in the same period, thus concluding the mandatory necessity of an energy storing unit.

The storage unit selected for the simulations was a pit storage, recessed beneath the ground's surface, with a total depth of 14 m, separating the fluid and soil with a polypropylene liner and insulated on the top cover by a layered polypropylene sheet, denominated NOMALEN (PlanEnergi, 2013; Thomas Schmidt et al., 2018). The storage was considered

with a total operating volume of 2000 m^3 filled with water and with maximum operating temperature of 85°C . Its purpose was to achieve the highest heat demand of the greenhouse, under the constraint of reaching optimal net cash flow benefits.

The energy modelling strategy was done based on heat balance between internal energy, surroundings and in and out fluxes of the GH and UpETC field. For this, a multi-node approach was conducted, by discretizing the volume on a series of sub-volumes with thermal conditions given by the most centred region of each discretised region, called node. The multi-node approach turned out to be a good approximation of the vertical thermal behaviour of the unit, managing to explain stratification, thermal mixing between nodes, heat losses to surroundings and effects from entering and exiting fluxes with dynamic thermal conditions.

Using the charge and discharge coefficients, allowed the choosing of the region in which incoming charged and discharged flows would mix with, thus promoting higher stratification quality and setting incoming fluxes to the ETC and GH on the bottom and top, respectively, showed a higher quality of available heat to the greenhouse and lower inlet temperatures on the ETC field, thus increasing solar coverage.

A transient conduction heat transfer approach was considered between the walls and bottom of the pit, considering the surrounding ground as a semi-infinite bulk region that due to thermal diffusion would create a thermal barrier near the walls, increasing as time passed. The heat losses accounted for 19.5% of the total heat provided from the ETC field, which went with accordance with the literature. The higher impact on heat losses come from the top cover, proving to be the region with higher necessity of insulation (Thomas Schmidt et al., 2018). Even though the results held similar results to past works, it would be required further studies to understand the true feasibility of this approach.

In the end, the pit provided a thermal behaviour similar to present cases in literature, concluding it as feasible numerical model, with 436 MWh of thermal capacity, completing almost 3 cycles of charging-discharging per year-period (Schach & Wollstein-Lehmkuhl, 2018), with an overall efficiency of 80.5%. From the stored heat, it provided 98.9% of its energy, reaching 73% of the total heat demand of the greenhouse farm, with remaining energy coming from an auxiliary energy source from the district heating net.

Along with the energetic analysis, a net present value economic approach was taken for a life-cycle of 20 years, where a net cash flow was done for every year summing all in and out flows of previous running years. Using the NPV, economic feasibility was reached, when 4 case scenarios, with interest rates of 1, 2, 5 and 10% interest rate, were studied and showed positive benefits on the last year of the lifecycle. Given the present interest rates in Denmark range the 1–2%, the prospected payback period was of 10 years with a benefit of 200 thousand euros in the end of the life-cycle.

Lastly, conducting a numerical simulation of a solar pit thermal energy storage unit for micro-climate control of a tomato greenhouse in the region of Aarhus, Denmark, proved to be a challenging strategy, but yielding positive energetic and economic revenues, thus proving

the feasibility of the implementation of these units on the farming industry, allowing to decrease the liability on fossil-fuel based heating systems.

6 FUTURE WORKS

Even though, comprising results were achieved in this thesis, it can be denoted that further studies could be done to increase its feasibility.

- After the results were discussed, it was possible to conclude that the greenhouse could be further studied with the introduction of passive mechanisms, like the introduction of north walls or the usage of ventilation heat recovery;
- The collector field showed a small solar coverage, which would require a comparison study, to understand the most fitting kind of collectors between ETC and FPC, given the lower costs of it;
- The semi-infinite conduction heat transfer approach could further benefit of an experimental work to check the comprising with the numerical simulations;
- Lastly, a multi-objective optimization analysis could be taken to reach higher thermo-economic profits and confidence level.

7 REFERENCES

- Abdi, H., Mohammadi-ivatloo, B., Javadi, S., Khodaei, A. R., & Dehnavi, E. (2017). Energy Storage Systems. In *Distributed Generation Systems: Design, Operation and Grid Integration*. <https://doi.org/10.1016/B978-0-12-804208-3.00007-8>
- Abdoly, M. A., & Rapp, D. (1982). Theoretical and experimental studies of stratified thermocline storage of hot water. *Energy Conversion and Management*, 22(3), 275–285. [https://doi.org/10.1016/0196-8904\(82\)90053-X](https://doi.org/10.1016/0196-8904(82)90053-X)
- Abood, A. A. (2015). A comprehensive solar angles simulation and calculation using matlab. *Energy and Environment*, 6(4), 367–376.
- Akelah, A. (2013). *Functionalized Polymeric Materials in Agriculture and the Food Industry*.
- Akhtar, N., & Mullick, S. C. (1999). Approximate method for computation of glass cover temperature and top heat-loss coefficient of solar collectors with single glazing. *Solar Energy*, 66(5), 349–354. [https://doi.org/10.1016/S0038-092X\(99\)00032-8](https://doi.org/10.1016/S0038-092X(99)00032-8)
- Almeida, J., Achten, W. M. J., Verbist, B., Heuts, R. F., Schrevels, E., & Muys, B. (2014). Carbon and water footprints and energy use of greenhouse tomato production in Northern Italy. *Journal of Industrial Ecology*, 18(6), 898–908. <https://doi.org/10.1111/jiec.12169>
- Andersen, E., Furbo, S., & Fan, J. (2007). Multilayer fabric stratification pipes for solar tanks. *Solar Energy*, 81(10), 1219–1226. <https://doi.org/10.1016/j.solener.2007.01.008>
- Arabkoohsar, A. (2016). *Dynamic modeling of a Compressed Air Energy Storage system in a grid connected photovoltaic plant*. Federal University of Minas Gerais.
- Arabkoohsar, A., Farzaneh-Gord, M., Ghezelbash, R., & Koury, R. N. N. (2017). Energy consumption pattern modification in greenhouses by a hybrid solar–geothermal heating system. *Journal of the Brazilian Society of Mechanical Sciences and Engineering*, 39(2), 631–643. <https://doi.org/10.1007/s40430-016-0569-8>
- Arfaoui, N., Bouadila, S., & Guizani, A. (2017). A highly efficient solution of off-sunshine solar air heating using two packed beds of latent storage energy. *Solar Energy*, 155, 1243–1253. <https://doi.org/10.1016/j.solener.2017.07.075>
- ASAE. (1998). Heating, Ventilating, and Cooling Greenhouses(EP406.3). *ASAE Standards*, 222.
- ASHRAE. (2017). *ASHRAE HANDBOOK FUNDAMENTALS* (I-P Editio; M. S. Owen, Ed.). W. Stephen Comstock.
- Badar, A. W., Buchholz, R., & Ziegler, F. (2011). Experimental and theoretical evaluation of the overall heat loss coefficient of vacuum tubes of a solar collector. *Solar Energy*, 85(7), 1447–1456. <https://doi.org/10.1016/j.solener.2011.04.001>
- Badar, A. W., Buchholz, R., & Ziegler, F. (2012). Single and two-phase flow modeling and analysis of a coaxial vacuum tube solar collector. *Solar Energy*, 86(1), 175–189. <https://doi.org/10.1016/j.solener.2011.09.021>
- Badescu, V. (2007). Optimal control of flow in solar collectors for maximum exergy extraction. *International Journal of Heat and Mass Transfer*, 50(21–22), 4311–4322. <https://doi.org/10.1016/j.ijheatmasstransfer.2007.01.061>
- Baggs, S. A. (1983). Remote prediction of ground temperature in Australian soils and mapping its distribution. *Solar Energy*, 30(4), 351–366. [https://doi.org/10.1016/0038-092X\(83\)90189-5](https://doi.org/10.1016/0038-092X(83)90189-5)
- Balaras, C. A., Dascalaki, E. G., & Aidonis, A. (2010). *High Solar Combi Systems in Europe*. (January). <https://doi.org/10.13140/2.1.2501.9686>
- Bartzanas, T., Tchamitchian, M., & Kittas, C. (2005). *Influence of the Heating Method on Greenhouse Microclimate and Energy Consumption*. 91, 487–499. <https://doi.org/10.1016/j.biosystemseng.2005.04.012>
- Başçetinçelik, A., Öztürk, H. H., Paksoy, H. Ö., & Demirel, Y. (1999). Energetic and exergetic efficiency of latent heat storage system for greenhouse heating. *Renewable Energy*, 16(1–4), 691–694. [https://doi.org/10.1016/S0960-1481\(98\)00253-5](https://doi.org/10.1016/S0960-1481(98)00253-5)
- Baytorun, A. N., Önder, D., & Gügerç, Ö. (2016). *Comparison of Fossil Fuel and Geothermal Energy Sources Used for Greenhouse Heating*. 4(10), 832–839.
- Ben Ali, R., Bouadila, S., & Mami, A. (2018). Development of a Fuzzy Logic Controller applied to an agricultural greenhouse experimentally validated. *Applied Thermal Engineering*, 141(February 2017), 798–810. <https://doi.org/10.1016/j.applthermaleng.2018.06.014>
- Bendimerad, S., Chermiti, A., Mahdjoub, T., Draoui, B., & Abène, A. (2011). Modeling , Characterization and Analysis of the dynamic behavior of heat transfers through polyethylene and glass walls of Greenhouses. *Physics Procedia*, 21, 67–74. <https://doi.org/10.1016/j.phpro.2011.10.011>
- Benli, H., & Durmuş, A. (2009). Evaluation of ground-source heat pump combined latent heat

- storage system performance in greenhouse heating. *Energy and Buildings*, 41(2), 220–228. <https://doi.org/10.1016/j.enbuild.2008.09.004>
- Bergman, T. L., Lavine, A. S., Incropera, F. P., & Dewitt, D. P. (2011). *FUNDAMENTALS OF HEAT and MASS TRANSFER* (7th ed.; L. Ratts, Ed.). Jefferson City: Don Fowley.
- Bircher, S., Skou, N., Jensen, K. H., Walker, J. P., & Rasmussen, L. (2012). A soil moisture and temperature network for SMOS validation in Western Denmark. *Hydrology and Earth System Sciences*, 16(5), 1445–1463. <https://doi.org/10.5194/hess-16-1445-2012>
- Böszörményi, L., & Šiváková, E. (2012). Contribution to mathematical modelling of charging and discharging of the seasonal heat storage tank. *International Review of Applied Sciences and Engineering*, 3(1), 75–79. <https://doi.org/10.1556/irase.3.2012.1.9>
- Boulard, T., Raeppele, C., Brun, R., Lecompte, F., Hayer, F., Carmassi, G., & Gaillard, G. (2011). Environmental impact of greenhouse tomato production in France. *Agronomy for Sustainable Development*, 31(4), 757–777. <https://doi.org/10.1007/s13593-011-0031-3>
- Braun, J. E., Klein, S. A., & Mitchell, J. W. (1981). Seasonal storage of energy in solar heating. *Solar Energy*, 26(5), 403–411. [https://doi.org/10.1016/0038-092X\(81\)90219-X](https://doi.org/10.1016/0038-092X(81)90219-X)
- Cadau, N., Lorenzi, A. De, Gambarotta, A., & Morini, M. (2019). *Development and Analysis of a Multi-Node Dynamic*.
- Campos Celador, A., Odriozola, M., & Sala, J. M. (2011). Implications of the modelling of stratified hot water storage tanks in the simulation of CHP plants. *Energy Conversion and Management*, 52(8–9), 3018–3026. <https://doi.org/10.1016/j.enconman.2011.04.015>
- Canakci, M., & Akinci, I. (2006). Energy use pattern analyses of greenhouse vegetable production. *Energy*, 31(8–9), 1243–1256. <https://doi.org/10.1016/j.energy.2005.05.021>
- Çaylı, A., & Akyüz, A. (2019). The Experimental Determination of The Impact of Overall Heat Consumption Coefficient and Thermal Screens on Heat Saving in Plastic Greenhouses. *Kahramanmaraş Sütçü İmam Üniversitesi Tarım ve Doğa Dergisi*, 2(2), 270–280. <https://doi.org/10.18016/ksutarimdoga.vi.493745>
- Chalabi, Z., & Zhou, W. (1996). Optimal Control of Greenhouse Heating. *IFAC Proceedings Volumes*, 29(1), 895–901. [https://doi.org/10.1016/S1474-6670\(17\)57777-0](https://doi.org/10.1016/S1474-6670(17)57777-0)
- Chauhan, P. S. (2018). *Thermal analysis of insulated north-wall greenhouse with solar collector under passive mode*. 37(4), 325–339.
- Chung, M., Park, J. U., & Yoon, H. K. (1998). Simulation of a Central Solar Heating system with Seasonal Storage in Korea. *Solar Energy*, 64(4–6), 163–178. [https://doi.org/10.1016/S0038-092X\(98\)00101-7](https://doi.org/10.1016/S0038-092X(98)00101-7)
- Cui, W., Liao, Q., Chang, G., Chen, G., Peng, Q., & Jen, T. C. (2011). Measurement and prediction of undisturbed underground temperature distribution. *ASME 2011 International Mechanical Engineering Congress and Exposition, IMECE 2011*, 4(PARTS A AND B), 671–676. <https://doi.org/10.1115/imece2011-63311>
- Czyzyk, K. A., Bement, S. T., Dawson, W. F., & Mehta, K. (2014). Quantifying water savings with greenhouse farming. *Proceedings of the 4th IEEE Global Humanitarian Technology Conference, GHTC 2014*, 325–332. <https://doi.org/10.1109/GHTC.2014.6970300>
- D'Arpa, S., Colangelo, G., Starace, G., Petrosillo, I., Bruno, D. E., Uricchio, V., & Zurlini, G. (2016). Heating requirements in greenhouse farming in southern Italy: evaluation of ground-source heat pump utilization compared to traditional heating systems. *Energy Efficiency*, 9(5), 1065–1085. <https://doi.org/10.1007/s12053-015-9410-y>
- Danish Agrifish Agency. (2016). *The State of the World's Biodiversity for Food and Agriculture in Denmark*. Retrieved from https://lbst.dk/fileadmin/user_upload/NaturErhverv/Filer/Landbrug/Genetiske_ressourcer/Denmark_SoWBFA_FINAL.pdf
- Danish Energy Agency. (2016). *Regulation and planning of district heating in Denmark*. 27. Retrieved from http://www.ens.dk/sites/ens.dk/files/climate-co2/Global-Cooperation/Publications/Publications/regulation_and_planning_of_district_heating_in_denmark.pdf
- Dannehl, D., Schuch, I., & Schmidt, U. (2013). Plant Production in Solar Collector Greenhouses - Influence on Yield, Energy Use Efficiency and Reduction in CO2 Emissions. *Journal of Agricultural Science*, 5(10), 34–45. <https://doi.org/10.5539/jas.v5n10p34>
- Dilara, P. A., & Briassoulis, D. (1998). *Standard Testing Methods for Mechanical Properties and Degradation of Low Density Polyethylene (LDPE) Films Used as Greenhouse Covering Materials : a Critical Evaluation*. 17, 549–585.
- Dincer, I., & Ezan, M. A. (2018). *Heat Storage: A Unique Solution For Energy Systems*. <https://doi.org/10.1007/978-3-319-91893-8>
- Djemoui, L., Bensaha, H., Benseddik, A., Zarrit, R., Guermoui, M., Rabehi, A., & Bouzاهر, M. T. (2018). Comparative study of geometrical configuration at the thermal

- performances of an agricultural greenhouse. *E3S Web of Conferences*, 61. <https://doi.org/10.1051/e3sconf/20186100003>
- Djørup, S., Sperling, K., & Østergaard, P. A. (2020). *District Heating Tariffs , Economic Optimisation and Local Strategies during Radical Technological Change*. 1–15.
- Druske, M., Fopah-lele, A., Korhammer, K., & Urs, H. (2014). Developed materials for thermal energy storage: synthesis and characterization. *Energy Procedia*, 61, 96–99. <https://doi.org/10.1016/j.egypro.2014.11.915>
- Fan, J., Furbo, S., & Yue, H. (2015). Development of a Hot Water Tank Simulation Program with Improved Prediction of Thermal Stratification in the Tank. *Energy Procedia*, 70, 193–202. <https://doi.org/10.1016/j.egypro.2015.02.115>
- Fan, J., Huang, J., Andersen, O. L., & Furbo, S. (2017). Thermal performance analysis of a solar heating plant. *ISES Solar World Congress 2017 - IEA SHC International Conference on Solar Heating and Cooling for Buildings and Industry 2017, Proceedings*, 291–300. <https://doi.org/10.18086/swc.2017.06.05>
- Farzaneh-Gord, M., Arabkoohsar, A., Deymi Dasht-bayaz, M., & Farzaneh-Kord, V. (2012). Feasibility of accompanying uncontrolled linear heater with solar system in natural gas pressure drop stations. *Energy*, 41(1), 420–428. <https://doi.org/10.1016/j.energy.2012.02.058>
- Farzaneh-Gord, Mahmood, Arabkoohsar, A., Bayaz, M. D. D., & Khoshnevis, A. B. (2013). New method of solar energy application in greenhouses to decrease fuel consumption. *International Journal of Agricultural and Biological Engineering*, 6(4), 64–75. <https://doi.org/10.3965/j.ijabe.20130604.008>
- Fujii, T., & Imura, H. (1972). Natural-convection heat transfer from a plate with arbitrary inclination. *International Journal of Heat and Mass Transfer*, 15(4), 755–767. [https://doi.org/10.1016/0017-9310\(72\)90118-4](https://doi.org/10.1016/0017-9310(72)90118-4)
- Furbo, S., Vejen, N. K., & Shah, L. J. (2005). Thermal performance of a large low flow solar heating system with a highly thermally stratified tank. *Journal of Solar Energy Engineering, Transactions of the ASME*, 127(1), 15–20. <https://doi.org/10.1115/1.1767190>
- Gao, Y., Fan, R., Zhang, X. Y., AN, Y. J., Wang, M. X., Gao, Y. K., & Yu, Y. (2014). Thermal performance and parameter analysis of a U-pipe evacuated solar tube collector. *Solar Energy*, 107, 714–727. <https://doi.org/10.1016/j.solener.2014.05.023>
- Gao, Yan, Zhang, Q., Fan, R., Lin, X., & Yu, Y. (2013). Effects of thermal mass and flow rate on forced-circulation solar hot-water system: Comparison of water-in-glass and U-pipe evacuated-tube solar collectors. *Solar Energy*, 98(PC), 290–301. <https://doi.org/10.1016/j.solener.2013.10.014>
- George, I., & Kalaivanan, R. (2017). *Experimental Study on U- pipe Evacuated Tube Solar Collector with Reflected Shield*. 21079–21090. <https://doi.org/10.15680/IJIRSET.2017.0611010>
- Gillings, R. J. (2020). *The volume of a truncated pyramid in ancient Egyptian papyri*. 57(8), 552–555.
- Gordon, J. (2013). *Solar Energy - The State of the Art* (Earthscan).
- Griepentrog, H. W., Blackmore, B. S., & Vougioukas, S. G. (2006). *CIGR Handbook of Agricultural Engineering Volume VI: Information Technology*.
- Grøn Energi. (2018). *The competitiveness of district heating compared to individual heating*.
- Gu, Y., Neal, O., & Dennis, L. (1998). *Development of an equivalent diameter expression for vertical U-tubes used in ground-coupled heat ...*
- Hatirli, S. A., Ozkan, B., & Fert, C. (2006). Energy inputs and crop yield relationship in greenhouse tomato production. *Renewable Energy*, 31(4), 427–438. <https://doi.org/10.1016/j.renene.2005.04.007>
- Henson, A., & Henson, A. (2006). *Conceptual Design of a Solar-Thermal Heating System with Seasonal Storage for a Vashon Greenhouse*.
- Hepbasli, A. (2011). A comparative investigation of various greenhouse heating options using exergy analysis method. *Applied Energy*, 88(12), 4411–4423. <https://doi.org/10.1016/j.apenergy.2011.05.022>
- Heuvelink, E. (1995). Growth, development and yield of a tomato crop: periodic destructive measurements in a greenhouse. *Scientia Horticulturae*, 61(1–2), 77–99. [https://doi.org/10.1016/0304-4238\(94\)00729-Y](https://doi.org/10.1016/0304-4238(94)00729-Y)
- IEA. (2011). *Technology Roadmap - Energy Storage*. In *IEA*. https://doi.org/10.1007/springerreference_7300
- IEA. (2015). *Seasonal thermal energy storage - Report on state of the art and necessary further R + D*. In *IEA-SHC Task 45 Large Systems*. Retrieved from http://task45.iea-shc.org/data/sites/1/publications/IEA_SHC_Task45_B_Report.pdf
- Jadidi, M. R., Sabuni, M. S., Homayounifar, M., & Mohammadi, A. (2012). Assessment of

- energy use pattern for tomato production in Iran: A case study from the Marand region. *Research in Agricultural Engineering*, 58(2), 50–56. <https://doi.org/10.17221/32/2010-rae>
- Jain, D., & Tiwari, G. N. (2003). Modeling and optimal design of ground air collector for heating in controlled environment greenhouse. *Energy Conversion and Management*, 44(8), 1357–1372. [https://doi.org/10.1016/S0196-8904\(02\)00118-8](https://doi.org/10.1016/S0196-8904(02)00118-8)
- Jamshidian, F. J., Gorjian, S., & Far, M. S. (2018). An Overview of Solar Thermal Power Generation Systems ; Components and 5 th International Conference and Exhibition on Solar Energy (ICESE-2018). *Solar Energy*, (August). Retrieved from <https://www.researchgate.net/publication/327160943%0AAa>
- Jiji, L. M. (2006). *Heat convection apparatus*.
- John A. Duffie, W. A. B. (2013). *Wiley: Solar Engineering of Thermal Processes, 4th Edition - John A. Duffie, William A. Beckman*. Retrieved from <http://eu.wiley.com/WileyCDA/WileyTitle/productCd-0470873663.html>
- Kittas, C., Katsoulas, N., Bartzanas, T., & Bakker, S. (2013). *Good Agricultural Practices for greenhouse vegetable crops*.
- Kooli, S., Bouadila, S., Lazaar, M., & Farhat, A. (2015). The effect of nocturnal shutter on insulated greenhouse using a solar air heater with latent storage energy. *Solar Energy*, 115, 217–228. <https://doi.org/10.1016/j.solener.2015.02.041>
- Kozai, T., Shida, K., & Watanabe, I. (1986). Thermal performance of a solar greenhouse with water tanks for heat storage and heat exchange. *Journal of Agricultural Engineering Research*, 33(2), 141–153. [https://doi.org/10.1016/S0021-8634\(86\)80036-1](https://doi.org/10.1016/S0021-8634(86)80036-1)
- Krasimirov Pavlov, G. (2014). Building Thermal Energy Storage. *Ph.D. Thesis BYG?DTU - Department of Civil Engineering Technical University of Denmark*, (April), 313.
- Krug, A. H., Romey, A., Rath, T., European, S., Science, H., August, N., ... Rath, T. (2020). *Control by Modelling . II . Modelling Plant Growth Decision Support for Climate Dependent Greenhouse Production Planning and Climate Control by Modelling . II . Modelling Plant*. 72(4), 145–151.
- Kumana, J. (2017). *Predict storage tank heat transfer precisely*. (January).
- Kumar, R., & Rosen, M. A. (2011). REVIEW OF SOLAR WATER HEATERS WITH INTEGRATED COLLECTOR-STORAGE UNITS. *International Journal of Energy, Environment and Economics*, 21(4), 345–382.
- Lafont, F., & Balmat, J. (2002). *Optimized fuzzy control of a greenhouse*. 128, 47–59.
- Lavan, Z., & Thompson, J. (1977). Experimental study of thermally stratified hot water storage tanks. *Solar Energy*, 19(5), 519–524. [https://doi.org/10.1016/0038-092X\(77\)90108-6](https://doi.org/10.1016/0038-092X(77)90108-6)
- Lavine, A. S., & Bergman, T. L. (2008). Small and large time solutions for surface temperature, surface heat flux, and energy input in transient, one-dimensional conduction. *Journal of Heat Transfer*, 130(10). <https://doi.org/10.1115/1.2945902>
- Lehr, J. H. (2016). *Alternative Energy and Shale Gas Encyclopedia* (J. H. Lehr, J. Keeley, & T. B. Kingery, Eds.). <https://doi.org/10.1002/9781119066354>
- Li, Z., Chen, C., Luo, H., Zhang, Y., & Xue, Y. (2010). All-glass vacuum tube collector heat transfer model used in forced-circulation solar water heating system. *Solar Energy*, 84(8), 1413–1421. <https://doi.org/10.1016/j.solener.2010.05.001>
- Lund, P. D., & Peltola, S. S. (1992). SOLCHIPS-A fast predesign and optimization tool for solar heating with seasonal storage. *Solar Energy*, 48(5), 291–300. [https://doi.org/10.1016/0038-092X\(92\)90057-H](https://doi.org/10.1016/0038-092X(92)90057-H)
- Mahboub, C., & Moumami, N. (2012). Calculation of the glass cover temperature and the top heat loss coefficient for 60° vee corrugated solar collectors with single glazing. *Solar Energy*, 86(2), 804–808. <https://doi.org/10.1016/j.solener.2011.11.019>
- Maraj, A., Londo, A., Firat, C., & Gebremedhin, A. (2019). Comparison of the energy performance between flat-plate and heat pipe evacuated tube collectors for solar water heating systems under mediterranean climate conditions. *Journal of Sustainable Development of Energy, Water and Environment Systems*, 7(1), 87–100. <https://doi.org/10.13044/j.sdewes.d6.0228>
- Mariani, L., Cola, G., Bulgari, R., Ferrante, A., & Martinetti, L. (2016). Space and time variability of heating requirements for greenhouse tomato production in the Euro-Mediterranean area. *Science of the Total Environment*, 562, 834–844. <https://doi.org/10.1016/j.scitotenv.2016.04.057>
- Mehrpooya, M., Hemmatabady, H., & Ahmadi, M. H. (2015). Optimization of performance of Combined Solar Collector-Geothermal Heat Pump Systems to supply thermal load needed for heating greenhouses. *Energy Conversion and Management*, 97, 382–392. <https://doi.org/10.1016/j.enconman.2015.03.073>
- Mishra, R. K., Garg, V., & Tiwari, G. N. (2015). Thermal modeling and development of

- characteristic equations of evacuated tubular collector (ETC). *Solar Energy*, 116, 165–176. <https://doi.org/10.1016/j.solener.2015.04.003>
- Monteith, J. L., & Unsworth, M. H. (2013). *Principles of Environmental Physics Plants , Animals , and the Atmosphere*. Elsevier Ltd.
- Naik, B. K., Varshney, A., Muthukumar, P., & Somayaji, C. (2016). *Modelling and Performance Analysis of U Type Evacuated Tube Solar Collector Using Different Working Fluids.pdf* (pp. 227–237). pp. 227–237. <https://doi.org/10.1016/j.efypro.2016.11.186>
- Nelson, P. V. (2004). *Greenhouse Operation and Management*, 6th ed. <https://doi.org/https://doi.org/10.21273/HORTTECH.14.3.0455A>
- Neupauer, K., & Kupiec, K. (2017). Heat Transfer Storage of Hot Liquid in the Tank. *Czasopismo Techniczne*, 4/2017, 27–38. <https://doi.org/10.4467/2353737xct.17.045.6356>
- Nijsskens, J., Deltour, J., Coutisse, S., & Nisen, A. (1984). *Heat Transfer Through Covering Materials of Greenhouses*. 33, 193–214.
- Nijsskens, J., Deltour, J., Coutisse, S., & Nisen, A. (1985). Radiation transfer through covering materials, solar and thermal screens of greenhouses. *Agricultural and Forest Meteorology*, 35(1–4), 229–242. [https://doi.org/10.1016/0168-1923\(85\)90086-3](https://doi.org/10.1016/0168-1923(85)90086-3)
- O. Paksoy, H. (2005). *Thermal Energy Storage for Sustainable Energy Consumption - Fundamentals, Case Studies and Design*. Izmir, Turkey: Springer.
- Ochs, F., Dahash, A., Tosatto, A., & Bianchi Janetti, M. (2020). Techno-economic planning and construction of cost-effective large-scale hot water thermal energy storage for Renewable District heating systems. *Renewable Energy*, 150, 1165–1177. <https://doi.org/10.1016/j.renene.2019.11.017>
- Ooteghem, R. J. C. Van. (2010). *Optimal Control Design for a Solar Greenhouse*. <https://doi.org/10.3182/20101206-3-JP-3009.00054>
- Oppel, F. J., Ghajar, A. J., & Moretti, P. M. (1986). Computer simulation of stratified heat storage. *Applied Energy*, 23(3), 205–224. [https://doi.org/10.1016/0306-2619\(86\)90055-3](https://doi.org/10.1016/0306-2619(86)90055-3)
- Ozgener, O., & Hepbasli, A. (2005). Experimental performance analysis of a solar assisted ground-source heat pump greenhouse heating system. *Energy and Buildings*, 37(1), 101–110. <https://doi.org/10.1016/j.enbuild.2004.06.003>
- Öztürk, H. H. (2005). Experimental evaluation of energy and exergy efficiency of a seasonal latent heat storage system for greenhouse heating. *Energy Conversion and Management*, 46(9–10), 1523–1542. <https://doi.org/10.1016/j.enconman.2004.07.001>
- Pagola, M. A., Jensen, R. L., Madsen, S., & Poulsen, S. E. (2017). *Measurement of thermal properties of soil and concrete samples*.
- Parkin, R. E. (2010). Solar angles revisited using a general vector approach. *Solar Energy*, 84(6), 912–916. <https://doi.org/10.1016/j.solener.2010.02.005>
- Pasgianos, G. D., Ar, K. G., & Polycarpou, P. (2003). *A nonlinear feedback technique for greenhouse environmental control*. 40. [https://doi.org/10.1016/S0168-1699\(03\)00018-8](https://doi.org/10.1016/S0168-1699(03)00018-8)
- Pavlov, G. K., & Olesen, B. W. (2012). Thermal energy storage-A review of concepts and systems for heating and cooling applications in buildings: Part 1-Seasonal storage in the ground. *HVAC and R Research*, 18(3), 515–538. <https://doi.org/10.1080/10789669.2012.667039>
- Pfeil, M., & Koch, H. (2000). *HIGH PERFORMANCE – LOW COST SEASONAL GRAVEL / WATER STORAGE PIT*. 69(6), 461–467.
- PlanEnergi. (2013). *Summary technical description of the SUNSTORE 4 plant in Marstal*. 1–7.
- PlanEnergi. (2015). *Final report SUNSTORE 3 Phase 2 Implementation*. Skørping.
- Pluimers, J. C., Kroeze, C., Bakker, E. J., Challa, H., & Hordijk, L. (2000). Quantifying the environmental impact of production in agriculture and horticulture in The Netherlands: Which emissions do we need to consider? *Agricultural Systems*, 66(3), 167–189. [https://doi.org/10.1016/S0308-521X\(00\)00046-9](https://doi.org/10.1016/S0308-521X(00)00046-9)
- Povstenko, Y. (2015). Fractional heat conduction in a semi-infinite composite body. *Communications in Applied and Industrial Mathematics*, 6(1), 1–13. <https://doi.org/10.1685/journal.caim.482>
- Rehman, S., Al-Hadhrami, L. M., & Alam, M. M. (2015). Pumped hydro energy storage system: A technological review. *Renewable and Sustainable Energy Reviews*, 44, 586–598. <https://doi.org/10.1016/j.rser.2014.12.040>
- Sabiha, M. A., Saidur, R., Mekhilef, S., & Mahian, O. (2015). Progress and latest developments of evacuated tube solar collectors. *Renewable and Sustainable Energy Reviews*, 51, 1038–1054. <https://doi.org/10.1016/j.rser.2015.07.016>
- Saikia, S. S., Nath, S., & Bhanja, D. (2019). *Effect of vacuum deterioration on thermal*

- performance of coaxial evacuated tube solar collector considering single and two phase flow modelling_ A numerical study.pdf* (pp. 127–143). pp. 127–143. <https://doi.org/10.10176/j:solener.20178.10.089>
- Salahaldin Na'man, Haval Y. Yacoob, O. S. O. (2013). OPTIMUM TILT ANGLE FOR SOUTH FACING FLAT SOLAR. *Journal of University of Zakho (JUOZ)*, 1(1), 405–413.
- Saltuk, B., & Artun, O. (2019). *MULTI-CRITERIA DECISION SYSTEM FOR GREENHOUSE SITE SELECTION IN MULTI-CRITERIA DECISION SYSTEM FOR GREENHOUSE SITE SELECTION IN GEDIZ BASIN , TURKEY USING GEOGRAPHIC INFORMATION SYSTEMS (GIS)*. (August).
- Santamouris, M., Argiriou, A., & Vallindras, M. (1994). DESIGN AND OPERATION OF A LOW ENERGY CONSUMPTION PASSIVE SOLAR. *Solar Energy*, 52(5), 371–378.
- Schach, R., & Wollstein-Lehmkuhl, A. E. (2018). Decentralized heat supply with seasonal heat storage systems: Comparison of different heating systems. *Energy Procedia*, 155, 320–328. <https://doi.org/10.1016/j.egypro.2018.11.046>
- Schmidt, T., Mangold, D., & Müller-Steinhagen, H. (2004). Central solar heating plants with seasonal storage in Germany. *Solar Energy*, 76(1–3), 165–174. <https://doi.org/10.1016/j.solener.2003.07.025>
- Schmidt, T, Mangold, D., & Müller-Steinhagen, H. (2003). Seasonal thermal energy storage in germany. *ISES Solar World Congress*, 1–7. Retrieved from <http://www.solites.de/download/literatur/03-03.pdf>
- Schmidt, Thomas, Alex, P., Schmidt, T., Djebbar, R., Boulter, R., Thornton, J., ... Corre, O. Le. (2018). Design Aspects for Large-scale Pit and Aquifer Thermal Energy Storage for District Heating and Cooling. *Energy Procedia*, 149, 585–594. <https://doi.org/10.1016/j.egypro.2018.08.223>
- Semple, L., Carriveau, R., & Ting, D. S. K. (2017). A techno-economic analysis of seasonal thermal energy storage for greenhouse applications. *Energy and Buildings*, 154, 175–187. <https://doi.org/10.1016/j.enbuild.2017.08.065>
- Shafieian, A., Khiadani, M., & Nosrati, A. (2019). Thermal performance of an evacuated tube heat pipe solar water heating system in cold season. *Applied Thermal Engineering*, 149(August 2018), 644–657. <https://doi.org/10.1016/j.applthermaleng.2018.12.078>
- Sharma, P. K., Tiwari, G. N., & Sorayan, V. P. S. (1999). *Temperature distribution in different zones of the micro- climate of a greenhouse : a dynamic model*. 40, 335–348.
- Singh, R. D., & Tiwari, G. N. (2010). Energy conservation in the greenhouse system : A steady state analysis. *EGY*, 35(6), 2367–2373. <https://doi.org/10.1016/j.energy.2010.02.003>
- Smith, R. (2005). *Chemical Process Design and Integration*. McGraw Hill.
- Soomro, A. A., Mokhtar, A. A., Akbar, A., & Abbasi, A. (2018). Modelling Techniques Used in the Analysis of Stratified Thermal Energy Storage: A Review. *MATEC Web of Conferences*, 225(January). <https://doi.org/10.1051/mateconf/201822501015>
- statista.dk. (2020). statista.dk. Retrieved from www.statista.dk
- Sturm, B., Maier, M., Royapoor, M., & Joyce, S. (2014). Dependency of production planning on availability of thermal energy in commercial greenhouses - A case study in Germany. *Applied Thermal Engineering*, 71(1), 239–247. <https://doi.org/10.1016/j.applthermaleng.2014.05.095>
- Suárez, C., Pino, J., Rosa, F., & Guerra, J. (2019). Analytical approach to ground heat losses for high temperature thermal storage systems. *International Journal of Energy Research*, 43(1), 439–454. <https://doi.org/10.1002/er.4278>
- Taki, M., Rohani, A., & Rahmati-joneidabad, M. (2018). Solar thermal simulation and applications in greenhouse. *Information Processing in Agriculture*, 5(1), 83–113. <https://doi.org/10.1016/j.inpa.2017.10.003>
- Tian, R., Dai, X., Wang, D., & Shi, L. (2018). Study of Variable Turbulent Prandtl Number Model for Heat Transfer to Supercritical Fluids in Vertical Tubes. *Journal of Thermal Science*, 27(3), 213–222. <https://doi.org/10.1007/s11630-018-1002-7>
- Tian, Z., Perers, B., Furbo, S., & Fan, J. (2018). Thermo-economic optimization of a hybrid solar district heating plant with flat plate collectors and parabolic trough collectors in series. *Energy Conversion and Management*, 165(March), 92–101. <https://doi.org/10.1016/j.enconman.2018.03.034>
- Tisun. (2020). Tisun Storage Tanks Catalogue. Retrieved from <https://pdf.archiexpo.com/pdf/tisun/tisun-tanks/>
- Trushevskii, S. N. (2007). *Heat Conductivity Metamorphoses in Narrow Gaps Using the Example of Vacuum-Processed Glass Packs*. 43(3), 144–152. <https://doi.org/10.3103/S0003701X07030061>
- Tsui, Y. Y., Lin, S. W., & Ding, K. J. (2014). Modeling of heat transfer across the interface in two-fluid flows. *Numerical Heat Transfer, Part B: Fundamentals*, 66(2), 162–180.

- <https://doi.org/10.1080/10407790.2014.894450>
- Tulus, V., Boer, D., Cabeza, L. F., Jiménez, L., & Guillén-gosálbez, G. (2016). Enhanced thermal energy supply via central solar heating plants with seasonal storage : A multi-objective optimization approach. *Applied Energy*, 181, 549–561. <https://doi.org/10.1016/j.apenergy.2016.08.037>
- Ulgen, K. (2006). Optimum tilt angle for solar collectors. *Energy Sources, Part A: Recovery, Utilization and Environmental Effects*, 28(13), 1171–1180. <https://doi.org/10.1080/00908310600584524>
- van Henten, E. J. (1994). Greenhouse Climate Management: an Optimal Control Approach. In *Society*. [https://doi.org/10.1016/S0308-521X\(94\)90280-1](https://doi.org/10.1016/S0308-521X(94)90280-1)
- Verhaegh, A. P. (1996). *Efficiëntie van energie en gewasbeschermingsmiddelen bij tomaten en rozen in kassen; Nederland, Israël, Spanje en Marokko*.
- Vliet, G. C. (2000). Principles of Solar Engineering. In *Journal of Solar Energy Engineering* (Vol. 122). <https://doi.org/10.1115/1.1288930>
- Von Zabeltitz, C. (2011). Integrated greenhouse systems for mild climates: Climate conditions, design, construction, maintenance, climate control. In *Integrated Greenhouse Systems for Mild Climates: Climate Conditions, Design, Construction, Maintenance, Climate Control* (Vol. 9783642145). <https://doi.org/10.1007/978-3-642-14582-7>
- Xu, J., Li, Y., Wang, R. Z., & Liu, W. (2014). Performance investigation of a solar heating system with underground seasonal energy storage for greenhouse application. *Energy*, 67, 63–73. <https://doi.org/10.1016/j.energy.2014.01.049>
- Yan, H., Zhang, H., & Shao, Q. (2013). *Comparative Studies on the Efficiency of Solar Flat-plate Collector and Evacuated Tube Collector*. 294, 3–8. <https://doi.org/10.4028/www.scientific.net/AMM.291-294.3>
- Zaimoglu, Z. (2017). *REDUCING CO2 EMISSIONS IN GREENHOUSES REGARDING HEAT EFFICIENCY*. (November 2016). <https://doi.org/10.21474/IJAR01/2295>
- Zelzouli, K., Guizani, A., Sebai, R., & Kerkeni, C. (2012). Solar Thermal Systems Performances versus Flat Plate Solar Collectors Connected in Series. *Engineering*, 04(12), 881–893. <https://doi.org/10.4236/eng.2012.412112>
- Zhang, L., Xu, P., Mao, J., Tang, X., Li, Z., & Shi, J. (2015). A low cost seasonal solar soil heat storage system for greenhouse heating: Design and pilot study. *Applied Energy*, 156, 213–222. <https://doi.org/10.1016/j.apenergy.2015.07.036>

8 ANNEXES

In this chapter, the regressions of thermal properties of the air and water using data from ASHRAE, 2017 using the tendency line tool from Microsoft Excel 2013, using quadratic, potential and linear regressions to achieve the highest R^2 value. As can be seen from Figure 8-9, the water's specific heat had the lowest R^2 value, but even though, it is still possible to explain almost 96% of the overall values in that range and bearing in mind that the variability of the specific heat is fairly low.

I. REGRESSIONS OF THERMAL CHARACTERISTICS OF AIR

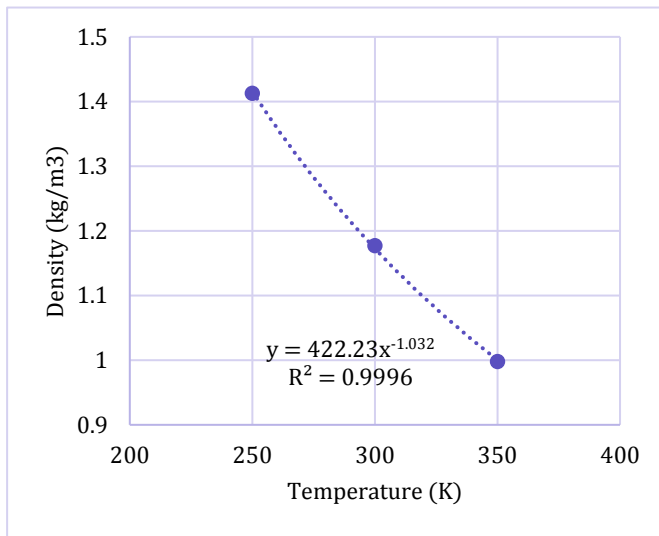


Figure 8-1 Regression of density of air from data

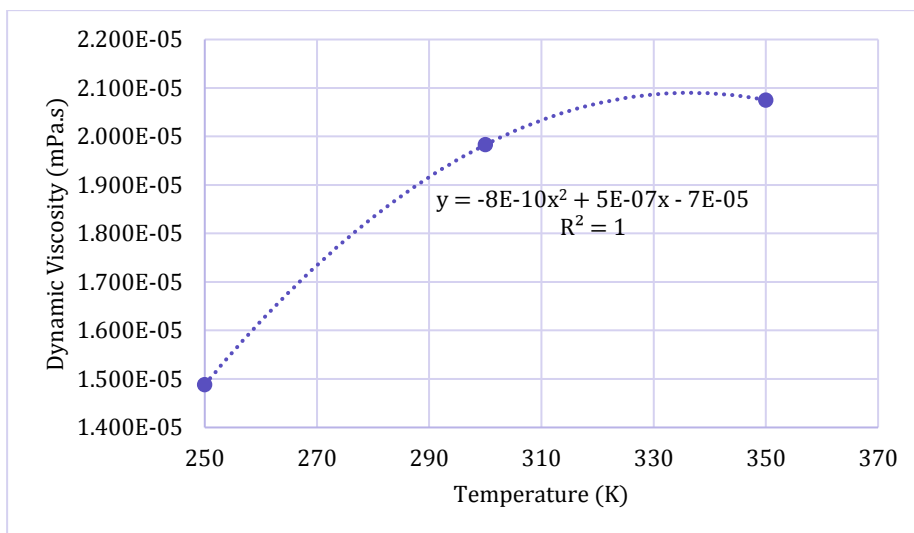


Figure 8-2 Regression of dynamic viscosity of air from data

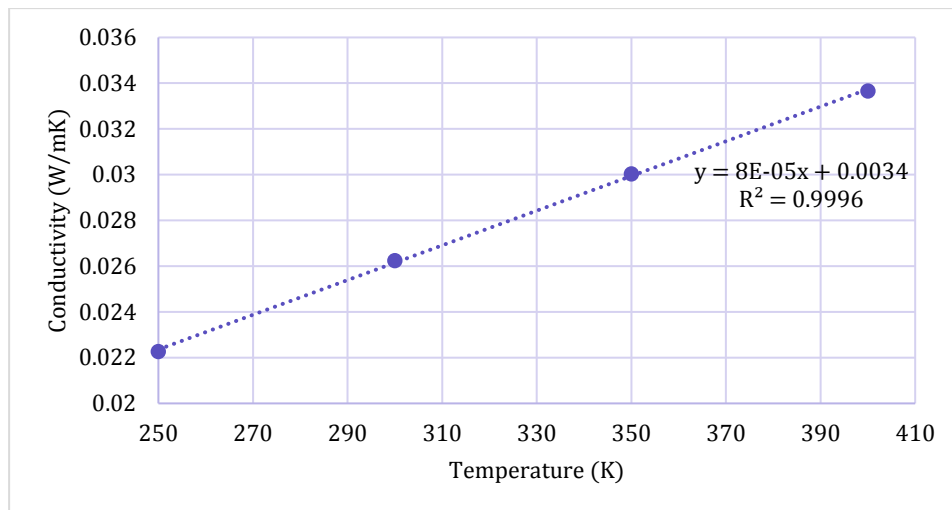


Figure 8-3 Regression of thermal conductivity of air from data

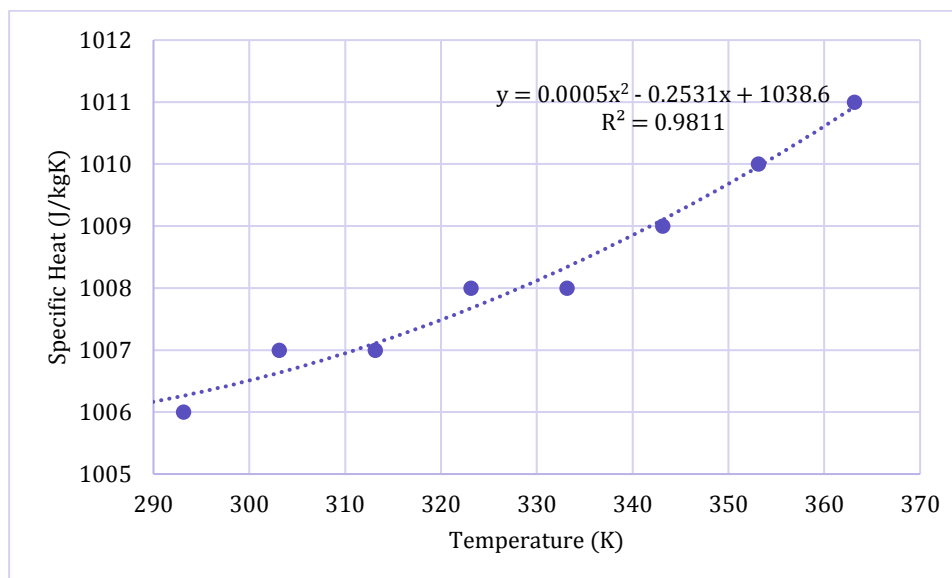


Figure 8-4 Regression of the specific heat of air from data

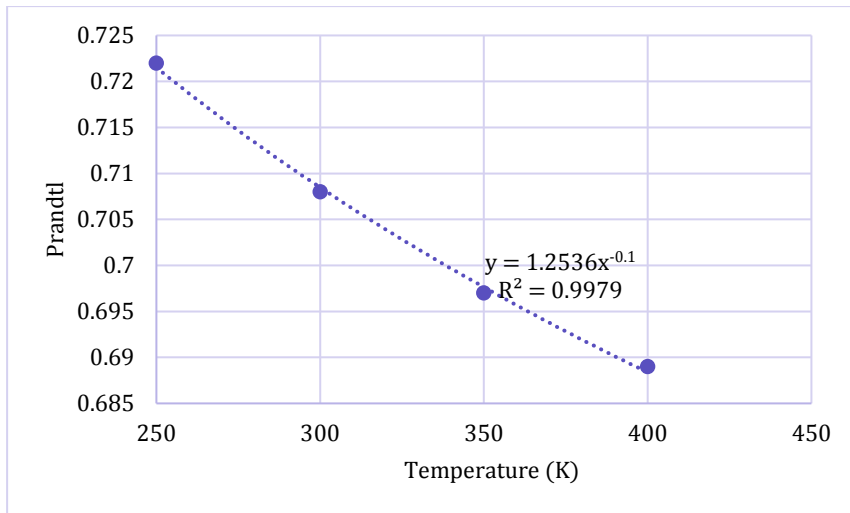


Figure 8-5 Regression of Prandtl number of air from data

II. REGRESSIONS OF THERMAL CHARACTERISTICS OF PURIFIED WATER

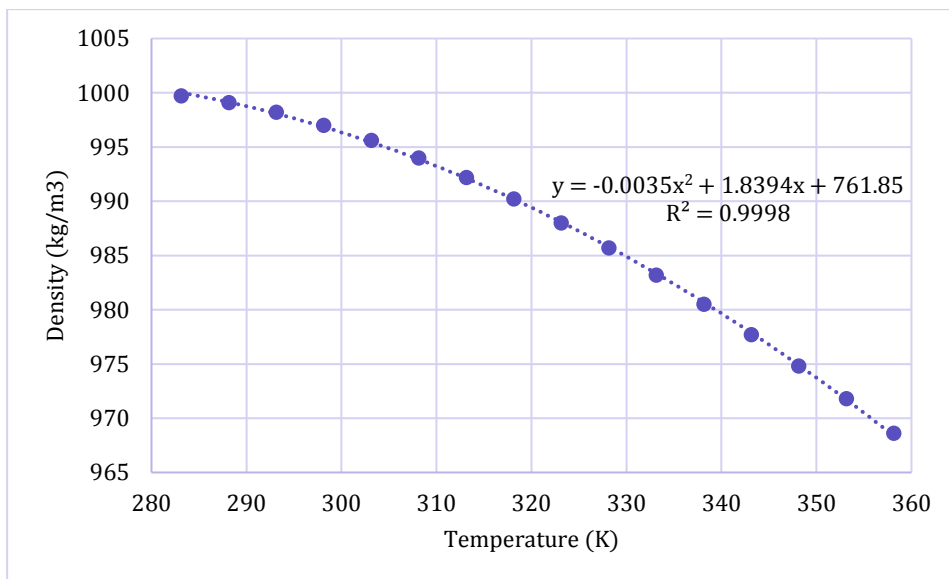


Figure 8-6 Regression of density of water from data

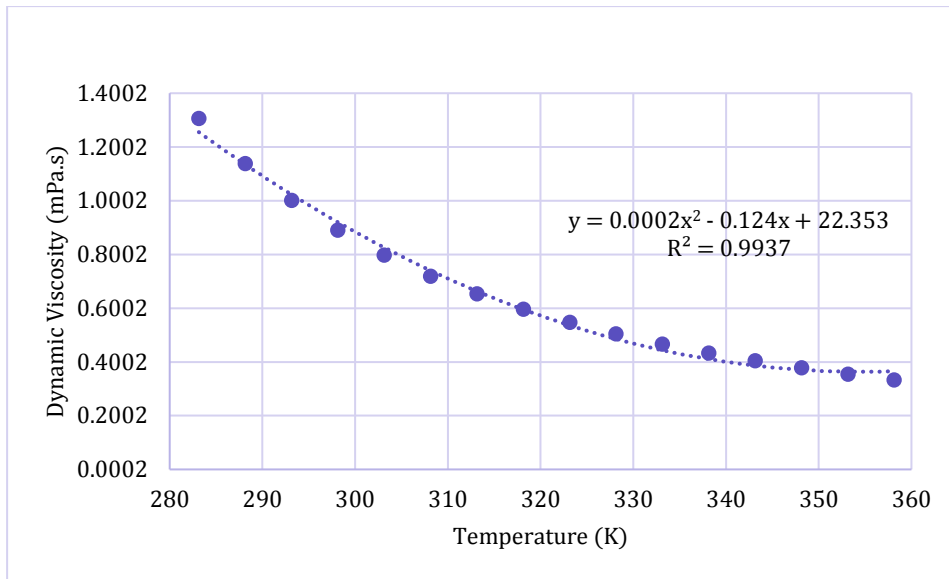


Figure 8-7 Regression of dynamic viscosity (mPa · s) of water from data

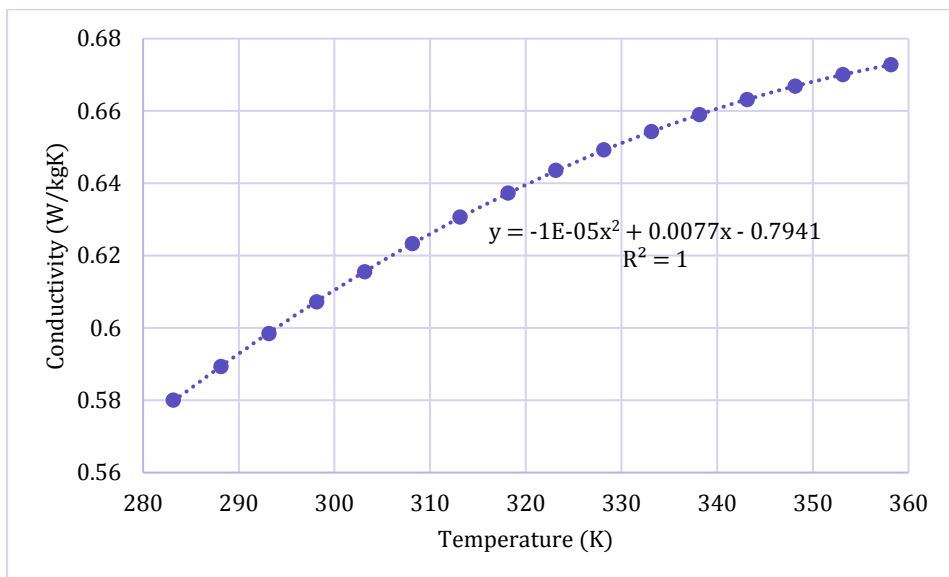


Figure 8-8 Regression of thermal conductivity of water from data

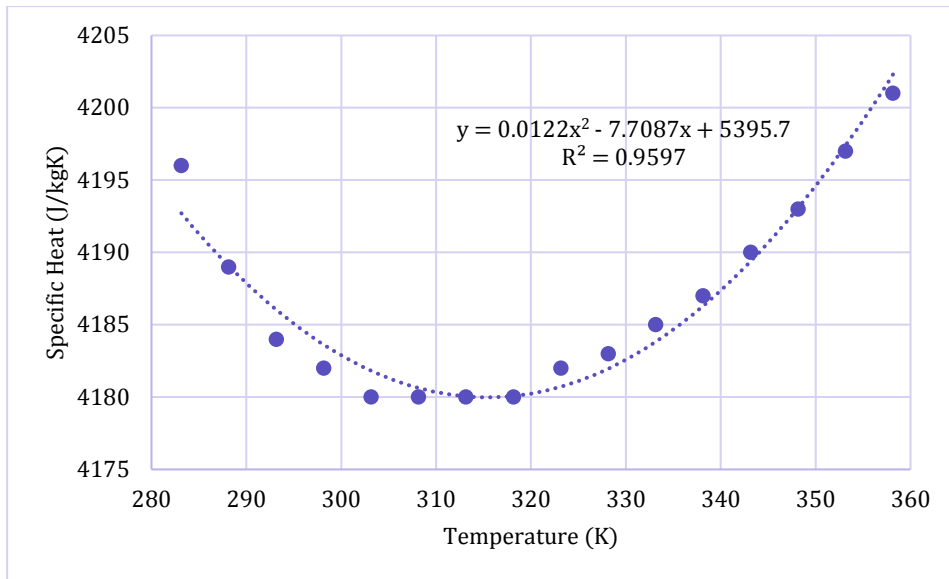


Figure 8-9 Regression of specific heat of water from data